First Principles Study On Novel And Functional Materials

Thesis submitted for the degree of

Doctor of Philosophy (Science)

in

Physics (Theoretical)

by

Shreya Das

Department of Physics
University of Calcutta
2021

To

My parents

Abstract

Designing of materials for improved functionalities are essential for technological advances. Material Physics, connecting physical science and material science, emphasizes on the understanding of materials, and this understanding is used further to optimize the known properties of a material as well as to design new materials. This calls the need for coming up with suggestions for materials with targeted properties before they can be tested in the laboratory. Keeping the above in mind modelling of materials is on high demand. A component of this modelling involves the understanding of the electronic structure of these materials at microscopic level as electrons govern the properties of the materials.

This thesis focuses on the understanding of the physics of specific class of materials namely functional materials. In particular the thesis stressed on exploring different interesting properties like high T_C ferromagnetic insulating nature, multi component high moment magnetism, multiferroicity and symmetry protected quantum spin-liquid behaviour, by employing *ab-intio* calculations within the framework of density functional theory (DFT) and the model Hamiltonian approach. The model Hamiltonians are solved by exact diagonalization technique and quantum Monte Carlo simulations to obtain the physical properties of the systems studied. Application of genetic algorithm further helps to predict actual crystal structure of a compound before tested into laboratories hence making the situation economic. The limited number of states, close to the Fermi energy, governing the electronic and magnetic properties of strongly correlated systems, necessitates the construction of few band Hamiltonian which was obtained through N^{th} order downfolding method in energy selective manner. The study taken up provides the microscopic understanding of the interesting properties of the respective systems with detailed description of their electronic and magnetic properties.

The computational results, presented in this thesis hopefully will make a base which will be useful to explore the novel properties of functional materials in future.

Shreya Das

Acknowledgements

This is the time to look back and convey my gratitude to them who have helped me in many ways in accomplishing this prestigious venture, Ph.D.

First and foremost, I owe my deepest gratitude to my supervisor Prof. Tanusri Saha-Dasgupta for her brilliant ideas, invaluable guidance and constant encouragement throughout the thesis work. Her enthusiasm, deep commitment to science influenced me immensely. I am extremely grateful to her for the suggestions she gave me in completing the thesis work during the Corona pandemic situation. Her constant drive worked as fuel to engage myself into work in the distracting depressing time of lockdown. Apart from academia her non-giving up mentality and determination made a great impact on me. I am thankful to her for giving me opportunity to carry out collaborative works in diverse fields with distinguished scientists: Prof. Indra Dasgupta, Prof. Arun Paramekanti, and Prof. Sugata Ray. I thank all of them and their group-members for the suggestions and discussions which helped me for the better understanding of the subject.

I also want to thank my seniors as well as collaborators Dr. Prabuddha Sanyal and Dr. Badiur Rahaman for their useful insights. A special thanks to my officiating co-supervisor Prof. Anjan Barman for running the administrative issues smoothly.

I am also very much grateful to S. N. Bose National Centre for Basic Sciences (SNBNCBS) for providing me the advanced computational facilities and comfortable stay here. The scenic beauty of the campus always made me feel refreshed. I would also like to thank Mr. Abhijit Ghosh for extending his helping hand in solving any computer related technical problem whenever it was needed. I would like to convey my sense of obligation to the Department of Science and Technology-INSPIRE fellowship for the funding assistance during my Ph.D tenure.

I express my deepest gratitude to my group members: Kartik, Hrishit, Dhani, Poulami, Ransell, Anita, Edwin, Aurab, Tilak, Dipayan and Uttam. Special thanks to Tilak, Kartik and Hrishit for helping me to learn the computational techniques in detail during the initial stage of my Ph.D. I am also thankful to the newly joined group of Samir, Aishwaryo, Shiladitya, Manoj, Koushik and Rajdeep. The brotherly companionship of them made my last phase of Ph.D journey more enjoyable.

During the long stay at SNBNCBS I had come across many good friends. The

joyous companionship of Anuvab, Tuhin, Suraka, Arnab, Sudip, Samrat, Khata, Prantik, Anupam, Jayarshi, Riju, Chandradip, Indranil, Swarnali, Siddhartha, Sutapa di, Sayani di, Krishnendu da made my hostel life at SNBNCBS memorable. I am grateful to my friends and I can not thank them enough for being by my side throughout the journey. I also thank the SNBNCBS badminton group which helped me to build up the sportsmanship as well as relax my mind.

I am also very much thankful to Atanu da, Atasi and Asif for their fruitful discussions in improving my computational skill and learning new techniques.

Finally, I express my heartfelt gratitude to my beloved family for their unconditional love and support. My parents and maternal uncle being so much supportive had never let me feel anything about the family deeds during my Ph.D tenure. I am extremely thankful to my mother for understanding me throughout the journey and providing the mental support constantly. I am grateful to my parents for encouraging me in achieving my goal and believing in myself.

Shreya Das
Kolkata, India 2021.

List of Publications

1. Re-examining the nature of ordering in $CaMnO_2$: The role of Mn-O covalency in the local structure
   Payel Aich, **Shreya Das**, Carlo Meneghini, Irene Schiesaro, Tanusri Saha-Dasgupta, Sugata Ray
   Physica B: Condensed Matter 581 411837 (2020)*.

2. Mixed Anion Physics in Flourinated vacancy ordered Brownmillerite: A possible route to Multiferrocity
   Payel Aich†, **Shreya Das**†, Carlo Meneghini, Desheng Fu, Vasudeva Siruguri, S. D. Kaushik, Mitsuru Itoh, Tanusri Saha-Dasgupta, and Sugata Ray
   † *Authors have equal contribution to this work*
   Manuscript submitted*.

3. Understanding the curious magnetic state of Sr_3OsO_6
   Shreya Das, Anita Halder, Atasi Chakraborty, Indra Dasgupta, and Tanusri Saha-Dasgupta
   Physical Review B 101, 184422 (2020)*.

4. Understanding Magnetism in Double Double Perovskites: A Complex Multiple Magnetic Sublattice System
   Anita Halder†, **Shreya Das**†, Prabuddha Sanyal, and Tanusri Saha-Dasgupta
   † *Authors have equal contribution to this work*
   arXiv:2101.10822. Manuscript communicated*.

5. $NiRh_2O_4$: A spin-orbit entangled diamond-lattice paramagnet
   Shreya Das, Dhani Nafday, Tanusri Saha-Dasgupta, and Arun Paramekanti
   Physical Review B 100, 140408(R) (2019)*.

6. Can we realize Kitaev quantum spin liquids in the $J_{eff} = 1/2$ honeycomb cobaltates?
   Shreya Das†, Sreekar Voleti†, Tanusri Saha-Dasgupta, and Arun Paramekanti
   † *Authors have equal contribution to this work*
   arXiv:2106.11982. Manuscript submitted.

7. Dynamic spin fluctuations in the frustrated spin chain compound $Li_3Cu_2SbO_6$
   A. Bhattacharyya, T. K. Bhowmik, D. T. Adroja, B. Rahaman, S. Kar, **S. Das**, T. Saha-Dasgupta, P. K. Biswas, T. P. Sinha, R. A. Ewings, D. D. Khalyavin, and A. M. Strydom
   Physical Review B 103, 174423 (2021).

8. Short-range and long-range magnetic order in $Fe(Te_{1.5}Se_{0.5})O_5Cl$
   E. S. Kozlyakova, K. N. Denisova, A. A. Eliseev, A. V. Moskin, A. Y. Akhrorov, P. S. Berdonosov, V. A. Dolgikh, B. Rahaman, **S. Das**, T. Saha-Dasgupta, P. Lemmens, A. N. Vasiliev, and O. S. Volkova
   Physical Review B 102, 214405 (2020).

.

This thesis is based on the publications marked with *

Contents

List of Figures

List of Tables

Chapter 1

Introduction

1.1 Introduction to functional materials

Material Physics is an interdisciplinary field of research at the cross-section of physical science and material science. It emphasizes on the understanding of materials, and the understanding thus gained for the use of optimization of known materials and design of new materials. This field has drawn attention in recent times due to its scientific importance together with technological implications.

In the thesis, we will focus on understanding the physics of specific class of materials namely functional materials. As the name suggests, the functional materials have the ability to perform a certain 'function' under an external stimuli. Thus the properties of a functional material is associated with its electric, magnetic, and or optical responses which can be affected by any external perturbation like applied magnetic field, temperature or pressure. The functional materials show a wide range of interesting physical properties [1–4]. This family includes piezoelectrics (e.g. $PbTiO_3$), ferroelectrics (e.g. $BaTiO_3$), semiconductors (e.g. $GdTiO_3$), ionic conductors (e.g. $CaTiO_3$), superconductors (e.g. $YBa_2Cu_3O_7$), magnetic materials (e.g. $LaMnO_3$), multiferroics (e.g. $BiMnO_3$), spintronic materials (e.g. Sr_2FeMoO_6) etc. Technological application of these functional materials are tremendous due to their spontaneous polarization, piezoelectricity, superconductivity and magnetoresistance effect which are dependent on the chemical composition and crystal structure of the materials. The properties of these functional materials making them attractive for technological applications are tunable by small changes in composition, or external conditions. An evergreen class of functional materials are transition metal oxides (TMOs) which can give rise to a variety of physical properties depending on their geometry and composition. In the thesis we have studied few of the TMOs aimed to explore certain functionalities namely,

1. High T_C ferromagnetic insulating properties

2. Symmetry protected quantum spin liquid behaviour
3. Multi component high moment magnetism
4. Multiferroicity

The following Fig. 1.1 describes our studied structural geometries and their properties.

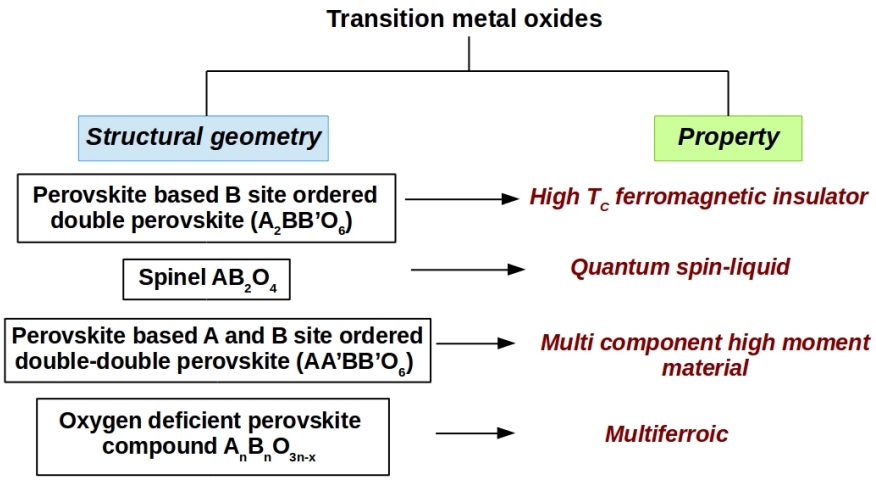

Figure 1.1: Different structural geometry and the corresponding properties of transition metal oxides studied in this thesis.

The electrical, magnetic and optical properties of materials are controlled by their composition and structure. The structure and the strength of materials are determined by the chemical bonding between the atoms, so that in a certain sense the chemistry controls the physical properties. Electron is the glue that binds atoms together. Thus at the microscopic level electrons govern the properties of the materials.

In this thesis we have carried out *density functional theory* (DFT) based *first principles* method to study the electronic stucture of the materials. This parameter free approach of the calculation takes into account all the structural and chemical aspects of a material correctly requiring only the crystal structure with proper atomic information of a material as the input. The outcomes are very reliable, fast and accurate. This framework is capable in accurately describing properties of vast diversity of materials starting from crystalline to amorphous and disordered materials, clusters, organics, inorganics, composites, molecules, biological systems, nano systems etc.

Although this is a highly successful method, the bottleneck is the approximation in choice of exchange-correlation functional. In the local density approxi-

mation (LDA) [5] of DFT calculation, the correlation and the exchange interactions are treated in terms of a local density which remains successful explaining the physical properties of many materials considering that the electronic correlations are weak in these materials. This approach fails to describe properties of strongly correlated systems like TMOs. To overcome this issue Hubbard U correlation has been added through DFT+U [6–8] calculations. As the physical properties of TMOs are controlled by very few states closely lying near Fermi level, we applied N^{th} order downfolding technique [9] to construct low energy few band Hamiltonian in energy selective manner from the Hilbert space to which the missing correlation effect beyond LDA was incorporated. The few band model Hamiltonian was then solved by quantum Monte Carlo method [10–12], exact diagonalization (ED) to obtain the physical properties of the strongly correlated system.

Furthermore we have also applied genetic algorithm [13, 14] to predict the structure of a material theoretically knowing its composition only before testing into laboratory. All these methods will be discussed in Chapter 2 elaborately.

Here in the following, after a general introduction on transition metal oxides, we will discuss the various functionalities and geometries considered in the thesis.

1.2 Transition metal oxides as functional materials

The structural and compositional flexibility of TMOs favour them to accommodate almost every element of the periodic table. Transition metal oxides have variety of interesting structural and physical properties. This class of materials are widely studied as their electronic structure show a wide range of properties starting from insulator to metal, superconductor, even half metal with spin polarized electrical conductivity. The magnetic arrangement can also be antiferromagnetic or ferromagnetic or rather ferrimagnetic or exhibiting complex spin texture like spiral magnetism. Some of them show colossal magnetoresistance too. The following Table-1.1 lists some examples of TMOs with their unique properties.

Insulator	$NaTiO_3$, $SrTiO_3$, $BaTiO_3$
Metal	$LaTiO_3$, $KMnO_3$
Semiconductor	$GdTiO_3$, $PbCrO_3$, $CaCrO_3$
Magnetic	$PbCrO_3$, $CaMnO_3$, $LaMnO_3$
Ferroelectric	$BaTiO_3$
Superconductor	$SrTiO_3$, K_xWO_3, Li_xWO_3
Piezoelectric	$PbTiO_3$
Ionic-conductor	$CaTiO_3$
Colossal magneto-resistance	Sr_2FeMoO_6
Multiferroic	$BiMnO_3$

Table 1.1: Few examples of transition metal oxides with their different physical properties.

The strongly correlated unfilled d electrons of the TM atoms drive the interesting electronic and magnetic properties [15]. The basic structural unit of these materials is the metal-oxygen polyhedra (TMO_n, where TM = transition metal, O = oxygen, n = integer). The coordination of the TM atom with the surrounding oxygens can be of different types e.g. octahedral, square pyramidal, square planar, tetrahedral, pentagonal bipyramidal, trigonal bipyramidal *etc.* The interaction between positively charged TM and negatively charged ligand (O) creates a static electric field in a crystal structure. This puts the d electrons of TM to be in an anisotropic field, known as crystal field. This results into splitting of d orbitals in energy levels, known as crystal field splitting (CFT). Thus an isolated TM atom has spherically symmetric crystal field but in solids this symmetry is lowered and CFT lifts the degeneracy of five-fold d (l = 2; l^z = -2, -1, 0, 1, 2) orbitals. The splitting is affected by the following factors:

- nature and oxidation state of the metal ion; higher oxidation state leads to larger splitting
- geometry of TM's surrounding ligand
- strength of TM-O covalency

Fig. 1.2 shows different TMO polyhedra and their corresponding crystal field splitting. The most common coordination symmetry is octahedral in which the TM ion is surrounded by six ligand oxygens forming TMO_6 polyhedra, as shown in Fig. 1.2 (a). In cubic crystal field of regular octahedron, the d-orbitals split into (i) higher energy level of two-fold (four-fold considering spin) degenerate e_g consisting of $d_{x^2-y^2}$ and d_{3z^2} orbitals, and (ii) lower energy level of three fold (six-fold considering spin) degenerate t_{2g} consisting of d_{xy}, d_{yz}, d_{xz} orbitals. The e_g level gains energy as $d_{x^2-y^2}$ and d_{3z^2} orbitals are pointed directly towards the surrounding oxygen ions and feel strong electrostatic repulsion, whereas d_{xy}, d_{yz}, d_{xz} orbital lobes are directed in between two oxygen atoms so they experience comparatively weaker electrostatic repulsion hence lower in energy.

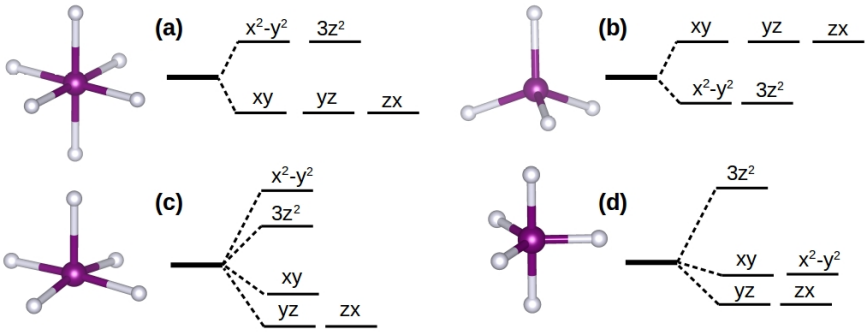

Figure 1.2: Symmetry and corresponding crystal field splitting of d levels for few regular known polyhedra of TMO: (a) Octahedra, (b) Tetrahedra, (c) Square pyramid, (d) Trigonal bipyramid. Purple and light gray balls represent transition metal atom and oxygen respectively.

Further lifting of ground state degeneracy takes place when degenerate e_g levels are partially filled and this is achieved by octahedral distortion, known as Jahn-Teller (JT) distortion, named after Hermann Jahn and Edward Teller [16]. The geometrical distortion, associated with doubly degenerate e_g states, as given by Q_2 and Q_3 modes is shown in Fig. 1.3.

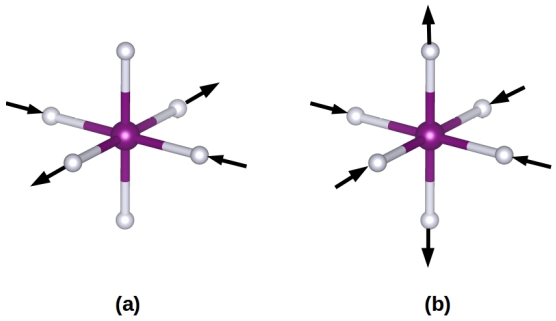

Figure 1.3: Two different JT modes (a) Q_2 and (b) Q_3 in TMO_6 octahedra.

The total volume preserving modes can be written as follows by using normalization:

$$Q_2 = \frac{1}{\sqrt{2}}(x-y),\ Q_3 = \frac{1}{\sqrt{6}}(2z-x-y) \tag{1.1}$$

Tetragonal elongation along z-axis takes place for $Q_3 > 0$ and for $Q_3 < 0$ tetragonal compression occurs. In tetragonal elongation the strong d-p hybridization between the transition metal and oxygen atoms in xy plane puts the energy of d_{x2-y2} level higher than that of d_{z2} by shortening of the TM-O distance. In the same fashion for t_{2g} levels, d_{xy} orbital lies at the top having the highest energy

and d_{xz} and d_{yz} go down with lower energy. The splitting of d orbitals in tetragonal compression is just reverse to that of tetragonal elongation [17]. The splitting of d orbitals in tetragonal distortion (Q_3 distortion) is shown in Fig. 1.4.

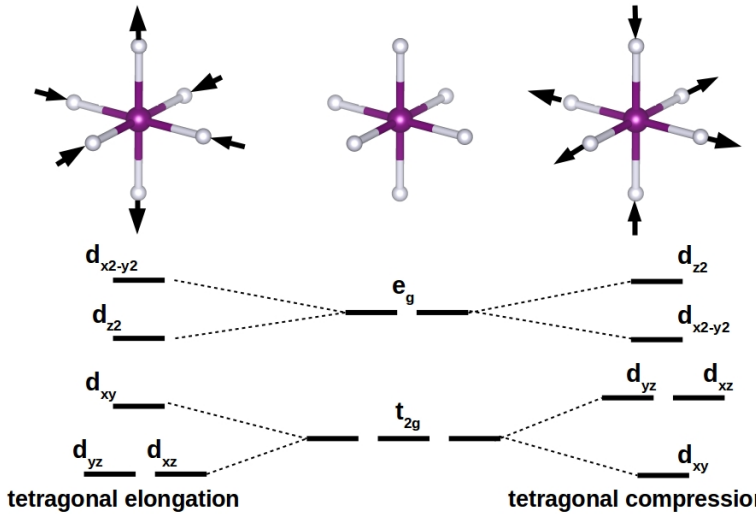

Figure 1.4: Splitting of d orbitals due to tetragonal distortion. Left and right panels show splitting due to tetragonal elongation and tetragonal compression respectively. The middle panel represents the splitting due to crystal field of regular TMO_6 octahedra.

In the orthorhombic distortion (Q_2 mode) shown in Fig. 1.3 (a), with $x \to x+\delta$, $y \to y-\delta$, $z \to z$, both t_{2g} and e_g levels split giving rise to a orthorhombic local symmetry. The splitted e_g levels become the linear superpositions of $|z^2\rangle$ and $|x^2-y^2\rangle$ and can be written as $\frac{1}{\sqrt{2}}(|z^2\rangle \pm |x^2-y^2\rangle)$. The t_{2g} levels also split into three singlets.

Trigonal distortion splits the t_{2g} levels due to the TMO_6 octahedral distortion along one of the [111] axes while the e_g levels remain intact. The t_{2g} levels are split into a singlet a_{1g} and a doublet e_g^{π}. The wavefunctions are as follows:

$$|a_{1g}\rangle = \frac{1}{\sqrt{3}}(|xy\rangle + |xz\rangle + |yz\rangle) \tag{1.2}$$

$$|e^{\pi}_{g\pm}\rangle = \pm\frac{1}{\sqrt{3}}(|xy\rangle + e^{\pm 2\pi i/3}|xz\rangle + e^{\mp 2\pi i/3}|yz\rangle) \tag{1.3}$$

The corresponding splitting for trigonal elongation and trigonal contraction are shown in Fig. 1.5.

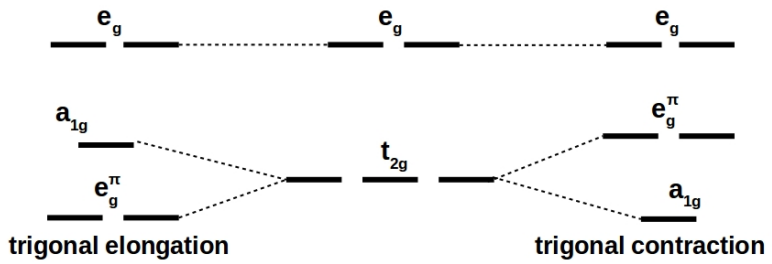

Figure 1.5: Splitting of d orbitals due to trigonal distortion. Left and right panels show splitting due to trigonal elongation and trigonal contraction respectively. The middle panel represents the splitting due to crystal field of regular TMO_6 octahedra.

According to Jahn-Teller theorem, spin (Kramers) degeneracy which is invariant with respect to time reversal is the only allowed degeneracy in the ground state. All other degeneracies will be unstable and will correspond to a maximum (saddle point) instead of a minimum of the total energy. Thus any small distortion will lift the orbital degeneracy. Suppose for the case of four d electrons e.g. in Mn^{3+} (d^4) in cubic crystal field of regular octahedron, three electrons will be on t_{2g} levels making the t_{2g} subshell half filled and the fourth electron will be on one of the doubly degenerate e_g levels. This situation becomes the same for the e_g holes in the case of Cu^{2+} with d^9 configuration. Thus in cubic crystal field, considering the e_g electron or e_g hole, there exists an extra orbital degeneracy besides the double-spin degeneracy (spin of electron or hole can be either $\uparrow$ or $\downarrow$). Thus according to Jahn-Teller theorem, the system will distort itself in such a way that it will lift the degeneracy of e_g levels lowering the total energy of the system. For a small distortion u, e_g levels split as $\pm gu$ (g being the electron-phonon coupling constant) and this will cost an elastic energy of $\frac{1}{2}Bu^2$, where B is the Bulk modulus. Assuming the coupling constant g to be positive, the total energy of the ground state (E) as a function of distortion becomes as follows:

$$E = \pm gu + \frac{1}{2}Bu^2, \tag{1.4}$$

At $u = 0$ the energy levels become degenerate, shown in Fig. 1.6. The minimum energy can be found for a finite distortion u_0 by minimizing the Eq. 1.4 with respect to u,

$$\frac{\partial E}{\partial u} = 0 \Rightarrow u_0 = \pm\frac{g}{B} \tag{1.5}$$

Putting these values of u_0, the doubly degenerate minimum energies are obtained,

$$E_0 = E_{JT} = -\frac{g^2}{2B} \tag{1.6}$$

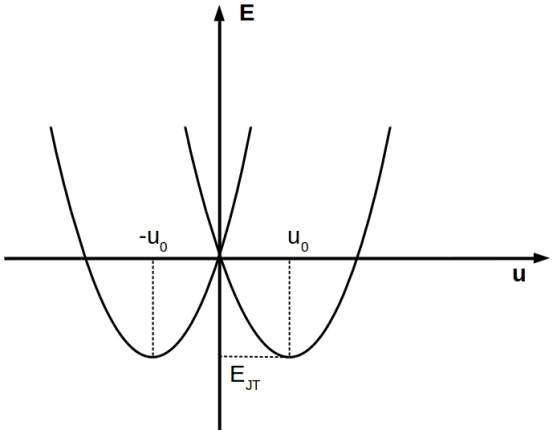

Figure 1.6: Dependence of the energy levels as a function of degeneracy lifting distortion u.

These energy minima are the electronic energy gain which is achieved due to distortion, overcompensates the elastic energy loss. Thus following Jahn-Teller theorem, it is obvious that symmetric situation leads to extra degeneracy to the ground state which is unstable and a small distortion can lift the ground state degeneracy lowering the total energy of the system.

Besides all these, the p-d hybridization or covalency plays an important role on the splitting of the d levels of transition metal atoms thus it determines the crystal field splitting Δ_{CF}. In TMOs the direct d-d overlap of the transition metal atoms is negligibly small due to the surrounding oxygen cage and the overlap of the d orbitals are channelised indirectly through the nonzero overlap between TM d and O p orbitals. The magnitude of this p-d hybridization depends on,

- the orientation of the d orbitals with respect to the surrounding O p orbitals, corresponds to the low energy phenomenon and,
- the relative energy position of TM d (ϵ_d) and O p (ϵ_p) orbitals i.e. the charge transfer energy $\Delta = \epsilon_d - \epsilon_p$.

The head on (directed toward one another) overlap of TM d orbitals and O p orbitals [cf. Fig. 1.7 (a)] gives a strong hybridization, called σ hybridization, denoted as $t_{pd\sigma}$ normally involving d e_g electrons. Other overlap except being directly oriented to each other gives comparatively weak hybridization, called π hybridization involving d t_{2g} electrons [cf. Fig. 1.7 (b)] and the hopping matrix element is denoted as $t_{pd\pi}$. In π hybridization, the p orbitals are perpendicularly oriented to the TM-O bonds.

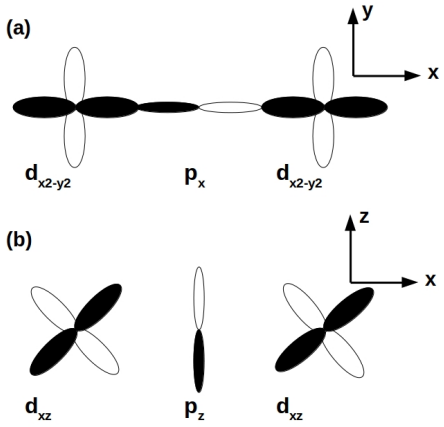

Figure 1.7: Examples of configurations for transition metal d and ligand p orbitals in case of (a) σ and (b) π hybridization.

Normally the energy level of TM d orbitals (ϵ_d) lie higher than that of the O p orbitals (ϵ_p). Due to strong $pd\sigma$ hybridization these p and d levels got mixed and repel giving rise to splitting of the energy levels as,

$$\epsilon_{\pm} = \frac{\epsilon_d + \epsilon_p}{2} \pm \sqrt{\frac{(\epsilon_d - \epsilon_p)^2}{2} + t_{pd\sigma}^2} \tag{1.7}$$

where ϵ_- and ϵ_+ are the energies of bonding (b) and antibonding (a) levels of d orbitals [cf. Fig. 1.8].

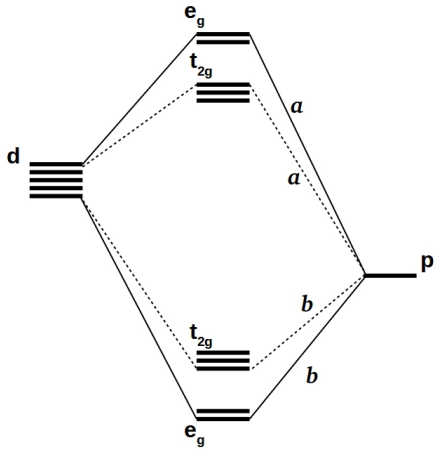

Figure 1.8: Schematic diagram of the origin of crystal field splitting in p-d hybridization. b and a denote the bonding and antibonding levels respectively.

In situation $t_{pd} \ll \epsilon_d - \epsilon_p$, the bonding and antibonding energy levels of the

e_g orbitals of TM atoms become,

$$\epsilon_b = \epsilon_p - \frac{t_{pd\sigma}^2}{\epsilon_d - \epsilon_p}$$
$$\epsilon_a = \epsilon_d + \frac{t_{pd\sigma}^2}{\epsilon_d - \epsilon_p} \tag{1.8}$$

As the π hybridization is weaker than σ hybridization, the bonding-antibonding splitting of t_{2g} orbitals will be smaller than that of e_g orbitals which is schematically shown in Fig. 1.8. The p-d hybridization and the crystal field splitting increases as the radius of the d orbital increases in going from $3d$ to $4d$ to $5d$ TM elements due to enhanced covalency contribution.

The filling of d electrons of transition metal ion in available d levels depend on the crystal field splitting (Δ) and Hund's coupling (J_H). When Δ is not too large, the d electrons will occupy the energy levels in such a way that the total spin will be maximum, following the Hund's rule. Thus d levels will be filled one by one with the electrons, having parallel spin until five d levels are occupied. After this, if the total electron number is greater than 5, the electrons will start to fill the d levels with opposite spins. This type of configuration is known as high-spin (HS) states. For an example we take Mn^{3+} with d^4 configuration. In the crystal field of regular octahedron, the three electrons occupy the lower lying t_{2g} levels with parallel spin. The fourth electron can occupy either one of the e_g levels with parallel spin to that of the t_{2g} electrons or can go to the t_{2g} levels with opposite spin, depending upon the crystal field splitting (Δ) [cf Fig. 1.9].

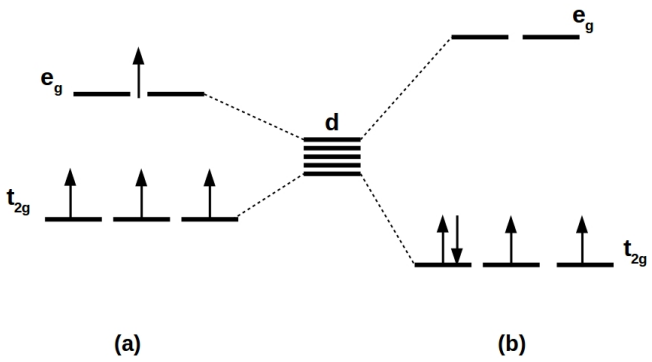

Figure 1.9: Schematic representation of (a) high-spin (HS) and (b) low-spin (LS) state of d^4 configuration in the crystal field of a regular octahedron.

The HS state with this particular example of Mn^{3+} is shown in Fig. 1.9 (a). Energy gain in putting the fourth electron in the e_g level with parallel spin to that of the t_{2g} electrons is $E_{Hund} = -3J_H$, but this electron lies in the upper lying

e_g level and it costs energy Δ. If the fourth electron goes to one of the lower lying t_{2g} levels with opposite spin, crystal field energy (Δ) is gained but Hund's rule energy ($-3J_H$) is lost. Such an electron occupation is known as low-spin (LS) states [cf. Fig. 1.9 (b)]. Thus for small crystal field splitting i.e. $\Delta < 3J_H$, high-spin state is favourable and when the field splitting is large i.e. $\Delta > 3J_H$, low-spin state is being favoured. HS states are commonly found in $3d$ transition metal oxides where the crystal field splitting is not too large. LS and HS both the states can be observed in $3d$ TM oxide $LaCoO_3$ [18] with $S = 0$ and $S = 2$. In this compound both the states have comparable stability thus they are seen in accessible temperatures. Though the LS state has slightly lower energy. The HS state is seen in comparatively elevated temperature as a large spin entropy is associated with $S = 2$ and atoms gain energy from spin-spin interactions as they gain the spins or they even start to order magnetically. $4d$, $5d$ oxides exhibit LS states prominently due to stronger p-d hybridization and larger crystal field splitting than that of $3d$ elements.

d electrons of transition metals are not totally screened from their neighbouring atoms unlike f electrons thus they have an intermediate character of showing itinerant electron properties as well as localized electron properties [15]. Thus transition metal elements experience the interplay of following two opposing tendencies:

- The on-site Coulomb (electron-electron) interaction tries to localize the electrons giving rise to the local magnetic moment
- The overlap between TM d orbitals, bridged through O p hybridization tries to delocalize the electrons in itinerant states giving rise to delocalized band.

The Hamiltonian of the celebrated Hubbard model [19] incorporates these two opposing tendencies and has the form as,

$$\begin{aligned} H &= U \sum_i n_{i\uparrow} n_{i\downarrow} - t \sum_{\langle i,j \rangle, \sigma} c^\dagger_{i\sigma} c_{j\sigma} + c^\dagger_{j\sigma} c_{i\sigma} \\ &= H_{int} + H_{band} \end{aligned} \tag{1.9}$$

where, U is the on-site Coulomb repulsion between two electrons occupying the same site with opposite spin, $c^\dagger_{i\sigma}(c_{i\sigma})$ is the creation(annihilation) operator at site i with spin σ, t is the electron hopping matrix element and $\langle i, j \rangle$ goes over nearest neighbours. The electron occupancy at site i with spin σ can be written as $n_{i,\sigma} = c^\dagger_{i,\sigma} c_{i,\sigma}$. Each lattice site in Hubbard model can be described by these

following four local basis states:

$$|0\rangle_i \qquad \text{i site is empty} \tag{1.10}$$

$$|\uparrow\rangle_i = c^\dagger_{i\uparrow}|0\rangle_i \qquad \text{i site is occupied by } \uparrow \text{ electron} \tag{1.11}$$

$$|\downarrow\rangle_i = c^\dagger_{i\downarrow}|0\rangle_i \qquad \text{i site is occupied by } \downarrow \text{ electron} \tag{1.12}$$

$$|d\rangle_i = c^\dagger_{i\uparrow}c^\dagger_{i\downarrow}|0\rangle_i \qquad \text{i site is doubly occupied} \tag{1.13}$$

Consider the simple case where each site is occupied by single electron. Now hopping of one electron from site i to site j, makes the site i empty and creates a hole at it. Thus pre occupied by a single electron, site j becomes doubly occupied and this process costs energy due to Coulomb repulsion (U) to put two electrons on a single site. On the other hand because of electron hopping, kinetic energy of both the electrons and the hole is gained as they start to move through the crystal which ultimately forms an energy band with bandwidth $W = 2zt$, where z is the number of nearest neighbours. Presence of these two competing factors sets a critical parameter U_{cr}, depending upon which the system will be metallic or insulator. System becomes insulating for $U >> U_{cr} \sim W = 2zt$ and it does not give any conventional band picture as the electrons remain at their site without being itinerant. These type of systems are electron-electron correlation driven insulators, called as Mott-Hubbard insulators [18,20]. The nature of these insulators differs from ordinary band insulators which are caused by the band filling effect of electrons moving in periodic potential of the lattice.

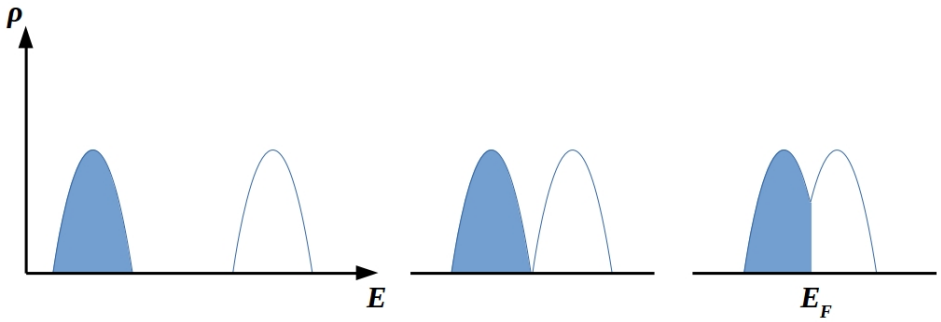

Figure 1.10: Schematic diagram of metal-insulator transition. From left to right: Hubbard subbands overlap on decreasing onsite Coulomb repulsion U gradually giving metallic solution. Middle figure: Hubbard subbands touch each other at U_{cr}. Filled and empty Hubbard subbands are marked in blue and white respectively.

For large $U >> U_{cr} \sim W = 2zt$, Hubbard subbands are well separated with an energy gap E_g, making the solution insulating. For the critical value U_{cr}, Hubbard subbands just touch each other giving rise to metallic solution. Thus if we start from non-interacting ($U = 0$) i.e. from metallic solution and gradually

increase U, for the critical value of (U/t), a metal to insulator transition takes place and we get a finite density of states (ρ_F) at Fermi level (E_F) [cf. Fig. 1.10]. For the case of, one electron per site, in the occupation-number dependent band structure, the lower subband will be filled (marked as blue in Fig. 1.10), called lower Hubbard subband and the upper one will be empty (marked as white in Fig. 1.10), called upper Hubbard subband.

Within the Hubbard picture, considering the 3D form of density of states (DOS) at the subband edges, electron density $\rho(E_F)$ increases continuously from 0 as U decreases below U_{cr} [cf. Fig. 1.11 left panel] and gives rise to a second-order metal-insulator transition at $U = U_{cr}$. However the correlation driven metal-insulator transition was advocated to be first-order metal-insulator transition by Mott. The argument was as follows, one can get a small concentration of electrons δn in upper subband and holes in lower subband for a slight overlap of these two bands. The metal to insulator transition was suggested to be discontinuous transition due to the localization of excitions formed between electrons and holes [cf. Fig. 1.11 right panel]. This complex phenomena, captured by Hubbard scenario is called Mott-Hubbard transition.

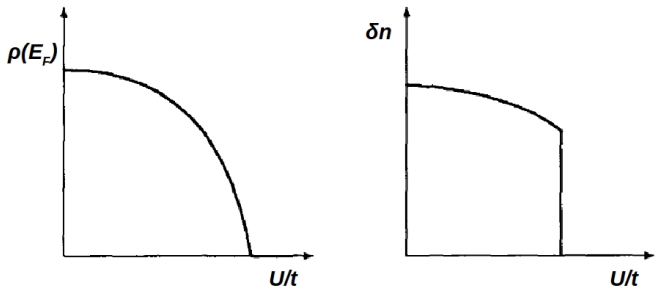

Figure 1.11: Schematic representation of metal-insulator transition without and with the long-range screening effect of Coulomb force. Left panel: $\rho(E_F)$ approaches to 0 gradually as Hubbard subbands separate, gives second-order transition. Right panel: Long-range Coulomb force gives discontinuous first-order Mott-Hubbard transition. Fig. is taken from Ref. [18].

In case of strong correlation effect $U >> t$, and for a system where electron number occupation (n) differs from the case of single electron per site i.e. $n \neq 1$, the interplay of spin and charge degrees of freedom is described effectively by t-J model. This model strictly prohibits double occupancy at the same site. At $n = 1$ and large U limit, t-J model reduces to Heisenberg model with effective Hamiltonian as,

$$H_{eff} = J \sum_{\langle i,j \rangle} S_i . S_j \tag{1.14}$$

where, S_i, S_j are the spin operators at site i and j respectively, and $J = \frac{2t^2}{U}$ is the exchange coupling constant.

For TMOs with $4d/5d$ TM elements the spin-orbit coupling (SOC) plays an important role to determine the electronic properties. It is the coupling between the intrinsic spin of the electron (S) and its orbital angular momentum (L). For TMOs containing $3d$ TM elements, SOC effect is treated as a weak perturbation because its effect on the physical properties of these materials is minimal, but becomes important for heavy elements like $4d/5d$. To handle the multi-orbital situation with SOC, the Hamiltonian takes the form as follows,

$$H = H_{int} + H_{band} + H_{SO} \tag{1.15}$$

where, H_{SO} represents the SOC effect and have the form as

$$H = \lambda \sum_i S_i.L_i$$

λ being the coupling constant and directly proportional to atomic number (Z). The interplay of strong correlation, spin-orbit coupling and band structure effect gives rise to some of the fascinating properties which we will take up in the following.

1.3 Different functionalities studied

1.3.1 High T_C ferromagnetic insulator

The wide spread use of magnetic materials however is limited by the demagnetization effect at ambient conditions. Thus to develop the full moment, materials should be operated sufficiently below the magnetic transition temperature T_C. This necessitates one to look for magnetic materials with T_C much higher than room-temperatures which can be operational at room-temperatures for practical use.

Double perovskites (DPs) with general chemical formula $A_2BB'O_6$ where A is alkaline or rare-earth metal and B and B′ are TM ions, are a family known for high T_C magnetic behaviour. Magnetism of DPs are widely discussed in context of Sr_2FeMoO_6 whose T_C is reported to be $\approx$ 410 K with half-metallicity [21]. The same trend is followed in Sr_2CrMoO_6 (T_C = 420K) [22], Sr_2CrWO_6 (T_C = 458K) [23,24], Sr_2CrReO_6 (T_C = 620K) [25]. Above room-temperature high T_C is also observed in ferrimagnetic Ca_2MnOsO_6 (T_C = 305K) [26]. The high T_C magnetic behaviour of these DPs opens up scopes for their spintronic applications.

The magnetic property of transition metal oxides is mainly governed by the

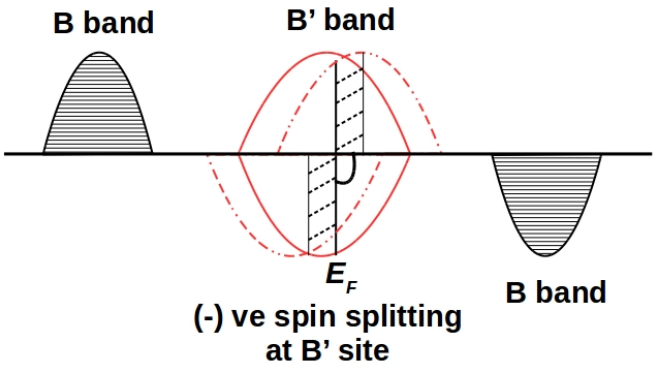

Figure 1.12: Schematic representation of hybridization-driven mechanism. Black hatched and solid red semi-ellipses represent the B bands and B′ bands respectively. Red dashed semi-ellipse represents the negative spin splitting of B′ after switching on the hybridization.

superexchange mechanism of d electrons of the TM ions. As the direct overlap between two TM ion is small, electron hopping is mediated through non-magnetic oxygen atoms. Distortion of BO_6 octahedra also plays an important role in this mechanism. Particular d electron configurations lead to have different physical properties. According to the Goodenough-Kanamori rules the ferromagnetic (FM) interaction is possible only with half-filled and empty orbital combinations [27]. Along with superexchange mechanism, hybridization-driven mechanism which is redolent of two site double exchange, plays a major role in determining the magnetism of double perovskites [28–30]. This mechanism takes place when the energy states of non-magnetic B′ site falls within the energy window of spin split states of the magnetic cation. This mechanism is defined by a large core spin at the magnetic B site and strong coupling on the B site between the core spin and the itinerant electron which is oppositely aligned to the core spin [cf. Fig. 1.12]. The itinerant electron is provided by the conduction electron and the primary magnetic interaction comes from delocalization of the mobile electron in the B-B′ network [31]. Switching on hybridization between B and B′ induces negative spin splitting at the non-magnetic B′ site which favours parallel (ferromagnetic) spin alignment of the B magnetic sites. Thus in these DP compounds the $3d$ magnetic moments are ordered parallel to each other and antiparallel to those of the $4d/5d$ elements. All the above mentioned DPs contain two different TM elements at B/B′ sites.

However there are also DPs where B site is occupied by nonmagnetic elements like Ca or Mg or Y instead of TM elements. Most of these single TM containing DPs like Ba_2CaOsO_6, Sr_2MgOsO_6, Ca_2MgOsO_6, Sr_2YReO_6 are reported to be either antiferromagnetic or exhibit spin-glass-like behaviour. It thus came to a

surprise that Sr_3OsO_6, epitaxially grown on $SrTiO_3$ substrate is reported to be high T_C (1060 K) ferromagnetic, containing single TM element Os at B′ site in double perovskite structural framework.

With the conventional knowledge it is known that ferromagnets are metal and antiferromagnets are insulators. Though few exceptions are also there which show the presence of ferromagnetic insulators. Ferromagnetic insulators like EuO (T_C = 77K), $CdCr_2S_4$ (T_C = 90K), $SeCuO_3$ (T_C = 25K) are reported. It is evident from reports that these all are low-T_C compounds. Exceptions like La_2NiMnO_6 (T_C = 280K), La_2CoMnO_6 (T_C = 240K) are reported with high T_C value FM insulators.

Furthermore the ferromagnetically ordered Sr_3OsO_6 was reported to be insulating. In the present thesis, we investigated the curious high T_C FM insulating state of Sr_3OsO_6.

1.3.2 Symmetry protected quantum spin liquid

Topology in electron system deals with the band structure properties, that remain preserved under continuous deformation. States with different topological ordering can not change into each other without going through a phase transition. One of the manifestations of topology in magnetically ordered electron system is Quantum Anomalous Hall Effect (QAHE) [32].

Topological properties in spin system are classified into two categories, (i) symmetry protected and (ii) symmetry unprotected. Symmetry protected topological (SPT) order is characterized by symmetry protected gapless or degenerate edge states (in 2D) instead of the bulk gap. 1D spin-1 Haldane chains [33–35] were known to be the first to show SPT ordering. Topological insulators protected by time-reversal symmetry with gapless edge states extends the example of SPT ordering in higher dimensions. The main difference between topological order and SPT order is that the gapless boundary excitations in intrinsic topological order is robust against any local perturbation whereas in SPT order the gapless excitations are robust against only any local perturbation that breaks the symmetry. Thus gapless boundary excitations in topological ordered states are topologically protected and in SPT states they are symmetry protected. On the other hand SPT states are short-range entangled whereas topological order states are long-range entangled.

Quantum spin liquid (QSL) systems are understood by spin degrees of freedom. They are characterized by long-range quantum entanglement lacking any particular magnetic order. QSL systems appear in two variants, (i) gapless and (ii) gapped. These two are distinguished by a Berry phase i.e. topological order term in low-energy action. The gapped integer spin system contains topological order manifesting itself as a non-local string order parameter with long-range order. Entanglement spectrum (ES) shows similarity between these gapped spin

systems with topological insulators. ES also shows that any perturbation destroying any long-range leaves the ES degeneracy so long as the inversion symmetry is preserved [36]. The surface of the gapless QSL systems breaks symmetry having an intrinsic topological order. The interacting quantum spins make the the ground state of QSL systems highly degenerate. Antiferromagnetic spin interaction on a triangular lattice is the root cause to lack a particular order.

The fermionic systems are limited to noninteracting models like topological insulators or superconductors. M. Levin *et al.* have established that bosonic model can be applied for the interacting systems. Lack of boson SPTs in high dimension paves the path for suggesting spin-one (S = 1) diamond lattice antiferromagnet with frustrated spin interactions. Prescription for this S = 1 models on diamond lattice system suggests that it can host a time-reversal symmetry protected topological quantum paramagnet, a spin analog of topological insulator. This suggestion puts transition metal oxides, crystallizing in spinel structure with general chemical formula AB_2O_4, into lime-light. B site spinels with magnetic B ions and nonmagnetic A site ions like ACr_2O_4, AV_2O_4 (A = Mg, Zn, Cd) are geometrically frustrated pyrochlore antiferromagnets. On the other hand spinels with nonmagnetic B site ions and magnetic A site ions form diamond lattice where the spins are frustrated. The competing exchange interactions of this diamond lattice can produce ground state degeneracy leading to quantum fluctuations. Beside spin frustration orbital degeneracy also impacts competing exchange interactions through spin-orbit coupling resulting in suppression of the long-range magnetic order. Reported studies on A site diamond lattice $MnSc_2S_4$ (S = 5/2) show the presence of spin-spiral state where the dominant nearest-neighbour (NN) antiferromagnetic (AFM) exchange interaction competes with small next-nearest neighbour (NNN) exchange interactions in presence of spin frustration. $CoAl_2O_4$ with S = 3/2 shows a unique glassy magnetic behaviour. $CoRh_2O_4$ (S = 3/2) and $CuRh_2O_4$ (S = 1/2) show spin-helix characteristics with Néel temperature 25 K and 24 K respectively. In $FeSc_2S_4$, Fe ($3d^6$) ions show orbital degeneracy which enhances the spin fluctuation leading to exhibit spin-orbital liquid characteristics.

Recently to achieve S = 1 A site diamond lattice system $NiRh_2O_4$ has grabbed the attention. The unusual example of $NiRh_2O_4$ with tetrahedrally coordinated Ni ($3d^8$) at A site and nonmagnetic Rh at B site, goes through cubic to tetragonal structural phase transition below $T \approx 440K$. The tetragonal phase with $c/a > 1$ allows SOC to play an important role in magnetism. Experimental studies of $NiRh_2O_4$ show spin gapped excitations in inelastic neutron scattering (INS). Another study claims topological paramagnetic behaviour for it. In contrast, a theoretical study for $NiRh_2O_4$ considering a Heisenberg model with competing AFM NN and NNN exchange interactions, claims for nonmagnetic ground state which arises due to large single-ion spin anisotropy. All the previous studies ignored orbital degrees of freedom but a recent one has put emphasis on orbital

degrees of freedom for the tetragonal phase of $NiRh_2O_4$. The absence of any proper and consistent theory of $NiRh_2O_4$ prompted us to focus on it to reveal its properties.

1.3.3 Multi component high moment magnetism

High moment systems are important for different applications in the field of spintronics, magnetic recording, catalysis, magnetic resonance imaging, and biomedical science to repair tissue, detox biological fluid etc. These systems can be also used to treat malignant tumours [37].

For the technological importance in achieving high moment, atomic clusters of homo or hetero atom species are made. Due to low dimensionality and large surface to volume ratio, magnetic moments of these clusters surpass their respective values in bulk systems [38]. Transition metal (TM) clusters show interesting physical properties, governed by their localized d electrons.

Apart from nano clusters, high moment magnetism in bulk form encourages to play with perovskite based transition metal oxides. The uncommon cation ordering in both A and B sublattices forms doubly ordered (double-double) perovskites (DDPs) extending the flexibility of perovskite structures further. Recently attention has been paid to achieve spontaneous ferroelectric polarization by combining two nonpolar rotational modes of oxygen octahedra in magnetic materials, called Hybrid Improper Ferroelectricity (HIF) which also provokes to design double-double perovskites [39]. With layered ordering at A site and rock-salt ordering at B site, $NaLaMgWO_6$ was the first known example of doubly ordered perovskite reported in 1984 [40]. Few other examples of such DDPs are synthesized under high-temperature and high-pressure conditions to extend the compound possibility beyond the limited ones and these are $NaLaMgTeO_6$ [41], $NaLaCoWO_6$ [42], $NaLaNiWO_6$ [42], $KLaMgWO_6$ [43] etc. In Table-1.2 few of the compounds of $NaLnCoWO_6$ (Ln = Y, Sm, Eu, Ho, Gd, Tb, Dy, Er, Yb) family and their synthesis conditions are listed [39].

$NaYCoWO_6$	1100°C, 5 Gpa
$NaSmCoWO_6$	1000°C, 5 Gpa
$NaEuCoWO_6$	1000°C, 5 Gpa
$NaHoCoWO_6$	1000°C, 5 Gpa

Table 1.2: Few examples and synthesis conditions of the compounds from $NaLnCoWO_6$ family.

High pressure condition stabilizes small magnetic transition metal ions at A sites instead of large nonmagnetic cations like Ca^{2+}, Sr^{2+} and thus it introduces A site magnetism into the system. Magnetism in A and B sublattices drives the interplay of magnetism between multiple sublattices giving rise to highly enriched magnetic properties. Discovery of new double double perovskite for rare-earth (R)

cations is done with $MnRMnSbO_6$ (R = La, Pr, Nd, Sm) under high pressure ≈ 10 GPa and high temperature 1473 K [44]. A sites are further splitted into Mn_A and Mn'_A with tetrahedral and square planer environment respectively. This crystallizes in tetragonal symmetry with space group $P4_2/n$. Analysis of magnetization of this family shows ferrimagnetic arrangement with A site and B site Mn spin alignment in antiparallel direction with T_C value between 50-90 K. The low temperature (2 K) magnetic structure has high Mn^{2+} moments 4.4 μ_B which is close to ideal moment 5 μ_B and Nd^{3+} has small moment 1.1 μ_B. The same structural type is also reported for $CaABReO_6$ materials like $CaMnFeReO_6$, $CaMnMnReO_6$ under high pressure and high temperature condition [45]. Further partial triple double cation ordering of three cations at A sites and two cations at B sites is reported for $CaMn_{0.5}Cu_{0.5}FeReO_6$. $CaMnFeReO_6$, $CaMn_{0.5}Cu_{0.5}FeReO_6$ show ferrimagnetism with antiparallel Fe and Re spins and measured magnetic moment supports the nominal valence of the cations. Although $CaMnMnReO_6$ has different magnetic order where the A site Mn^{2+} cations in square planar and tetrahedral coordination order ferromagnetically parallel to the c axis but the B site cations exhibit antiferromagnetism.

To achieve the cation and charge distribution for late first row transition metal ions, synthesis of magnetically ordered $CaMnMReO_6$ (M = Ni, Co) has been done recently under high pressure and high temperature conditions. Reported study shows ferromagnetic ordering for $CaMnNiReO_6$ and ferrimagnetic ordering for $CaMnCoReO_6$. The experimentally observed net magnetic moment for the compounds is quite high which paves the way for designing large moment magnetic oxides for spintronic applications. In this thesis we focused on $CaMnMReO_6$ (M = Ni, Co) compound to unravel the rich magnetism of high moment magnetic multiple sublattices.

1.3.4 Multiferroicity

Co-existence of the strong coupling of electric and magnetic degrees of freedom makes multiferroics technologically highly important for a range of applications in electronic device and sensors as the magnetism can be controlled with electric field rather than magnetic field. Table-1.3 shows few examples of TMOs exhibiting multiferroicity.

Ferroelectric-ferromagnetic	$BiMnO_3$
Ferroelectric-semiconductor	$SrTiO_3$, $YMnO_3$
Ferroelectric-antiferromagnetic	$HoMnO_3$, $BiCoO_3$
Antiferroelectric-antiferromagnetic	$BiFeO_3$
Ferroelectric- ferroelastic	$KNbO_3$
Ferroelectric-spiral magnetic	$TbMnO_3$

Table 1.3: Few examples of multiferroic transition oxides.

The source of magnetic order in a system is caused by the partially filled d or

f shells of TM ions whereas ferroelectricity is governed by different microscopic sources. Thus coupling two degrees of freedom one can have different types of multiferroicity. Multiferroics are classified into two categories as follows.

(i) Type-I multiferroics: This group of multiferroics contains materials whose ferroelectricity and magnetism are characterised by different sources which are independent to each other. The ferroelectricity takes place at higher temperature than that of the magnetic ordering and the spontaneous polarization has quite large value ($\approx$ 10 - 100 μC/cm^2) [46]. The source of spontaneous ferroelectric polarization is the displacive ferroelectric distortion associated with empty d orbitals. On the other hand the magnetic ordering requires partial d orbital filling. It is thus difficult to have coexistence of these two contrasting order parameter simultaneously as they are mutually exclusive. Thus the route to multiferroicity is to separate these two properties to different ions. In most of the known multiferroics the magnetic ordering is associated with the B site cations like Fe or Mn and the A site cation like Pb or Bi causes the ferroelectric polarization due to lone pair of electrons. For an example, $BiMnO_3$ or $BiFeO_3$ show ferroelectricity with magnetic Mn^{3+} and Fe^{3+} ions, and the Bi ion with lone pair electrons, moves away from the centrosymmetric position in its oxygen neighbourhood giving rise to a polarization. Although $BiFeO_3$ possesses very weak magnetoelectric coupling effect due to its weak magnetism. Ederer and Spaldin reported slight improvement in magnetization of $BiFeO_3$ [47] introducing oxygen vacancies through nonstoichiometric composition. Another route that can lead to ferroelectricity in type-I multiferroic materials is the charge ordering which is observed in TMOs with TM ions of different valency. Nickelates $RNiO_3$ show this kind of multiferroicity caused by charge ordering [48, 49]. In $TbMn_2O_5$ multiferroicity takes place due to dimerization. Another type of ferroelectricity occurs called as geometric ferroelectricity in $YMnO_3$ due to the tilting of MnO_5 block to achieve closer packing which ultimately leads the oxygen ions to move closer to Y ions making it ferroelectric [50].

(ii) Type-II multiferroics: This group of multiferroics includes materials whose magnetism is the source of their ferroelectricity and both are strongly coupled. The polarization in these materials is comparatively smaller ($\approx$ 10^{-2} μC/cm^2) [46] than that of type-I multiferroics. These type-II multiferroics are further grouped into two classes, one is where ferroelectricity is caused by magnetic spiral and the another one where ferroelectricity develops in collinear magnetic structures.
Most of the type-II multiferroics fall into the class of spiral type-II multiferroics where different kind of magnetic ordering is present at different temperatures e.g. $TbMnO_3$. In $TbMnO_3$ magnetic ordering is observed at

≈ 41 K and the magnetic structure changes at ≈ 28 K [51]. In this material the polarization flips depending on the applied magnetic field and forms a cycloid. Magnetic frustration also encourages for spiral magnetic ordering in insulators which makes one to conclude that type-II multiferroics are usually found with frustrated systems.
In the second group of type-II multiferroics where ferroelectricity appears in collinear magnetic structures, polarization takes place due to exchange striction. Collinear unique ↑↑↓↓ E-type antiferromagnetic arrangement breaks the centrosymmetry and induces polarization into the system because the distortion of ferro (↑↑) and antiferro (↑↓) bonds are different which is a consequence of exchange striction. As an example in $RMnO_3$ perovskites with unique E type antiferromagnetic arrangement exchange striction causes the oxygen ions to shift perpendicular to Mn-Mn bonds producing polarization.

Apart from these, mixed anion chemistry i.e. incorporation of a second anion in the system may lead to multiferroicity. The anion based strategy allows to design a new class of materials with multiple anions in a single phase, such as oxyfluorides (O-F), oxynitrides (O-N), oxysulfides (O-S) etc. For example in transition metal oxyfluorides the difference in electronegativity of O^{2-} and F^{-} plays important role. The stronger covalent TM-O interactions result in shorter bonds than that of the more ionic TM-F interactions which drives the displacement of the TM ion towards oxygen anions.

$CaMnO_3$ perovskite based transition metal oxide is an example to incorporate oxygen vacancy as Mn can have different valence states. The oxygen deficient compound possesses unique up-up-down-down magnetic arrangement showing coupling between electron, spin and lattice degrees of freedom. Introduction of F as a foreign anion in the oxygen deficient compound shows interesting properties leading to multiferroicity which we have taken up in this thesis.

1.4 Different structural geometries studied

Different structural geometries of transition metal oxides are studied in this thesis to explore different functional properties. In the following sections the geometries studied in the thesis are discussed.

1.4.1 B site ordered double perovskite

Double perovskite takes the formula $A_2B_2O_6$ where A is the rare-earth or alkaline metal ion and B is transition metal ion. Cation ordering can take place either at A site or B site. Cation ordering at A site is less common in comparison to B site ordered double perovskite. Difference in oxidation state plays an important role for it. B/B′ cation ordering can accommodate large difference (as seven) of

oxidation state but that for A/A′ site cation ordering is limited to two or less [52]. B site ordered double perovskite takes the formula as $A_2BB'O_6$ where B and B′ are the two TM cations. As a general rule it is found that for the difference of oxidation states of B and B′ less than two, disordered arrangement is observed and that of greater than two gives ordered arrangements. When this difference of oxidation states becomes two, we can have disordered, partially ordered or fully ordered arrangements depending on the ionic radii and bonding preference of B and B′ cations [52].

B site ordered double perovskites draw special interest as they can host $3d$, $4d/5d$ transition metals at B sites giving rise to interesting properties.

Cation ordering at B and B′ site can be three types as follows:

(i) Layered ordering: In this uncommon type of B site ordering the B and B′ TM cations have alternating arrangement only in one direction [cf. Fig. 1.13 (a)]. $R_2CuB'O_6$ with B′ = Sn/Zn and R_2CuSnO_6 with R = Nd/Pr/Sm have layered ordering at B sites [53].

(ii) Columnar ordering: In this ordering the B and B′ cations alternate in two directions [cf. Fig. 1.13 (b)]. In this rare ordering the A site is also occupied by two different elements [52].

(iii) Rock-salt ordering: This is the most common ordering of B site ordered double perovskites. Here the B and B′ cations have alternating arrangement in three directions [cf. Fig. 1.13 (c)].

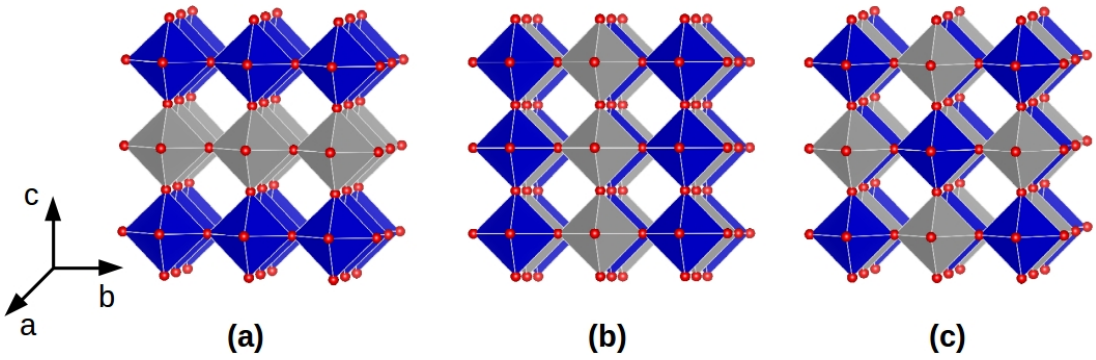

Figure 1.13: Different types of B site cation ordering: (a) layer, (b) columnar and (c) rock-salt. Small red balls represent oxygen atoms. BO_6 and $B'O_6$ polyhedra are coloured in blue and grey respectively. A site cations are omitted for clarity.

In rock-salt ordered structure which is the most common B site ordered double perovskite structure, the alternating arrangement of corner sharing BO_6 and $B'O_6$ octahedra along three axes make voids where the A site cations sit in. Most of

the perovskites are found to have divalent A site cations where A cations are alkaline/rare-earth elements. The larger ionic radii of A^{2+} compared to A^{3+} cations, favour most of the perovskites to host divalent A site cations. Divalent A site cations open up scopes of different combinations of B and B′ cations as, B^{4+}/B'^{4+}, B^{3+}/B'^{5+}, B^{2+}/B'^{6+} or B^{1+}/B'^{7+}. Monovalent A^{1+} cations are rare with only three reported examples: Na_2ZrTeO_6 [54], Na_2TiTeO_6 and Na_2SnTeO_6 [55]. Though the ionic radii of A^{1+} is larger than that of A^{2+}, it restricts the combination of oxidation states of B site cations. B site cation oxidation state combinations get limited to B^{5+}/B'^{5+}, B^{4+}/B'^{6+} and B^{3+}/B'^{7+}. These ultimately leads to have comparatively fewer DPs with monovalent A cations. The ideal crystal structure of rock-salt ordered double perovskite is cubic (space group *Fm-3m*) but it can go through structural distortion depending upon different reasons and lowers the symmetry of structure. The different factors responsible for structural distortion are as follows:

(i) The cationic size mismatch of A, B and B′ cations are one of the reasons to cause distortion. The ionic size mismatch is described by Goldschmidt's tolerance factor t as

$$t = \frac{(r_A + r_O)}{\sqrt{2}(\frac{r_B + r'_B}{2} + r_O)} \tag{1.16}$$

where, r_A, r_B, r'_B, r_O are the ionic radii of A, B, B′ and O ions respectively. Ideal cubic structure is obtained for $t = 1$. For the value of $t \neq 1$ distortion takes place. $t > 1$ implies larger A size cation which does not fit in the interstitial void and non-perovskite hexagonal structures are emerged out. $t < 1$ implies smaller A size cation and perovskite compensates this size mismatch by out-plane tilt and in-plane rotation of BO_6 and $B'O_6$ octahedra ($GdFeO_3$ type distortion).

(ii) Electronic instabilities like Jahn-Teller (JT) effect also cause distortion. JT active ions like Cu^{2+}, Mn^{3+} with orbital degeneracy exhibit octahedral distortion which lifts up the degeneracy and makes the structure stable. Most of the compounds with Mn^{3+} are disordered because of the small charge difference of the B and B′ cation in comparison to high oxidation state of Mn^{3+} which hinders cation ordering. $Sr_2MnB'O_6$ (B′ = Nb/Ta/Sb) show low degree of cation ordering among the disordered structures containing Mn^{3+}. For Cu^{2+} compounds the charge difference of B site cations are larger than that with Mn^{3+} and compounds are more ordered. Rock-salt ordered $Sr_2Cu\,MO_6$ (M = W/Te/Mo) [56] and layered ordered La_2CuSnO_6 show JT distortion [27].

(iii) Another cause to create distortion is ferroelectric displacement of a cation. Presence of Pb^{2+} or Bi^{3+} at A site leads to ferroic distortion due to lone

electron pair of these ions. For an example Pb_2MgTeO_6, Ba_2MMnO_6 (M = Co/Ni) show this kind of ferroic distortion [27].

1.4.2 Spinel

The class of spinel materials with the general chemical formula AB_2X_4 have drawn their attention as they serve as a source of novel physical properties. In the spinel structure the A sites are mainly divalent cations like Mg, Cr, Mn, Fe, Co, Ni, Cu, Zn, Cd, Sn; the B sites are trivalent cations like Al, Ga, Ti, V, Ni, Fe, Cr, and the X anions are typically the chalcogen elements like O, S, Se. Although monovalent (1+), trivalent (3+) A site spinels also exist. A site cation with 4+ valency are high-pressure forms of olivine minerals like $SiCo_2O_4$, $SiFe_2O_4$ [57]. This class of materials are named after $MgAl_2O_4$ which is a Al based spinel compound. Magnetite (Fe_3O_4), known as ledstone was first characterized as spinel mineral by Sir Bragg in 1915 [58]. Spinels are rich in showing their interesting properties. Fe_3O_4 was found to exhibit Verwey transition, a change in physical properties associated with structural transition [59]. $LiTi_2O_4$ exhibits superconductivity [60], LiV_2O_4 shows heavy-fermionic behaviour instead of having f electrons [61]. Besides all these, spinels are interesting due to their geological importance as they are found in earth's crust and mantle.

The crystal structure of a spinel consists of two metal sites with tetrahedral and octahedral coordination. Spinels are classified into two categories: normal spinel and inverse spinel.

- **Normal spinel:** In a normal spinel structure the A site cations are tetrahedrally coordinated whereas the B site cations are octahedrally coordinated [cf. Fig. 1.14]. A normal spinel consists of eight fcc cells in which the anions take the fcc lattice points. A site cations occupy 1/8th of tetrahedral voids and B site cations occupy 1/2 of the octahedral voids. Octahedrally coordinated B site cations form corner sharing pyrochlore B sublattice which is basically the network of corner linked B site tetrahedra.

- **Inverse spinel:** Inverse spinel differs with normal spinel in cationic distribution. In inverse spinel like $NiFe_2O_4$, Fe_3O_4, the A site cation is octahedrally coordinated and the B site cation is tetrahedrally coordinated. The general chemical formula for inverse spinel becomes $B(AB)O_4$ where half of the B cations occupy the tetrahedral coordination and remaining half of the B cations and A cations occupy the octahedral coordination. In case of magnetite Fe_3O_4, the charge distribution becomes as $Fe^{2+}Fe_2{}^{3+}O_4{}^{2-}$ [62]. Thus in magnetite A and B-site cations are same and they have different valences.

Here our discussion will be focusing on normal spinel stated as spinel.

The ideal cubic spinel oxide has space group $Fd\bar{3}m$ with high symmetry atomic

positions of A and B site cations and X anions sit at 32*e* *uuu* position which is the only structural free parameter aside from lattice constant in a spinel structure. Variation in this free parameter changes the relative size of the tetrahedra and octahedra introducing distortion within individual tetrahedron and octahedron keeping the symmetry of the structure intact [63]. The atomic positions of the A, B and X site ions depend on the setting of the origin and in $Fd\bar{3}m$ space group the possible unit cell origin can be one of the two different equipoints with point symmetries $\bar{4}3m$ and $\bar{3}m$. The origin can also be assigned to either a vacant site or an occupied site. Table-1.4 shows the atomic positions with Wyckoff notation of A, B, X ions for different choice of origin setting. The ideal cubic spinel structure

	Origin at $\bar{4}3m$		Origin at $\bar{3}m$	
	Origin at A site	Origin at tetrahedral vacancy	Origin at B site	Origin at octahedral vacancy
A site cation	*8a*	*8b*	*8b*	*8a*
B site cation	*16d*	*16c*	*16c*	*16d*
X anion	*32e*	*32e*	*32e*	*32e*

Table 1.4: Wyckoff notation of A, B and X ions for two different origin settings in $Fd\bar{3}m$ space group symmetry of ideal cubic spinel.

is shown in Fig. 1.14 showing the 3D network of corner linked B sublattice. The A only sublattice forms a diamond lattice which is made of two interlacing fcc lattices. The primitive unit cell consists of two formula units ($Z = 2$) and eight unit cells ($Z = 8$) to form a conventional unit cell containing 24 cations (8 A cations + 16 B cations) and 32 anions.

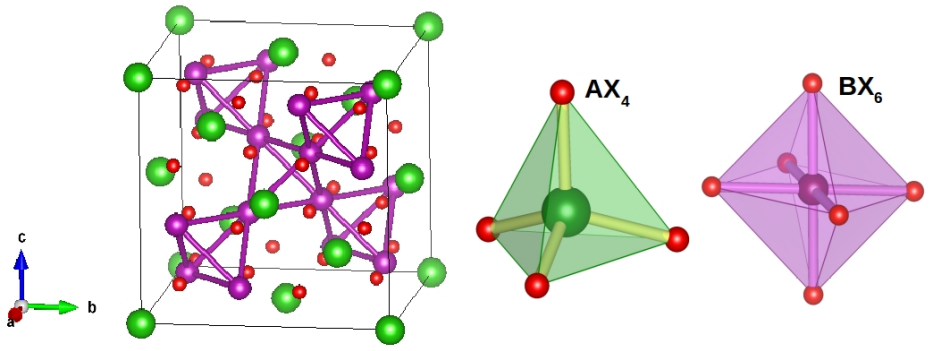

Figure 1.14: Left panel shows the crystal structure of a spinel compound. Green purple and small red balls represent A, B and X site ions respectively. The purple bonded corner sharing 3D network of tetrahedra is the pyrochlore B sublattice. In the right panel the tetrahedral and octahedral coordination of A and B site cations are shown separately.

Table-1.5 lists the atomic positions of the corresponding sites considering the origin at a lattice site occupied by A site ion with $\bar{4}3m$ point symmetry. Another

	Fractional coordinates of lattice sites Origin at A site		
	Wyckoff notation	Site symmetry	Coordinates
A site cation	*8a*	$\bar{4}3m$	(0,0,0); $(\frac{1}{4}, \frac{1}{4}, \frac{1}{4})$
B site cation	*16d*	$\bar{3}m$	$(\frac{5}{8}, \frac{5}{8}, \frac{5}{8})$; $(\frac{5}{8}, \frac{7}{8}, \frac{7}{8})$; $(\frac{7}{8}, \frac{5}{8}, \frac{7}{8})$; $(\frac{7}{8}, \frac{7}{8}, \frac{5}{8})$
X anion	*32e*	*3m*	(u, u, u); $(u,\bar{u},\bar{u})$; $(\bar{u},u,\bar{u})$; $(\bar{u},\bar{u},u)$; $(\frac{1}{4}\text{-}u,\frac{1}{4}\text{-}u,\frac{1}{4}\text{-}u)$; $(\frac{1}{4}+u,\frac{1}{4}+u,\frac{1}{4}\text{-}u)$; $(\frac{1}{4}+u,\frac{1}{4}\text{-}u,\frac{1}{4}+u)$; $(\frac{1}{4}\text{-}u,\frac{1}{4}+u,\frac{1}{4}+u)$

Table 1.5: Atomic coordinates of spinel in $Fd\bar{3}m$ symmetry considering origin at a lattice site occupied by A site cation with $\bar{4}$3m point symmetry

possible space group symmetry of spinels is $F\bar{4}3m$. In this space group the metal cations of the octahedral site i.e. the B site cations are displaced along [111] direction as the u value deviates from its ideal value ($u^{\bar{4}3m}_{ideal} = 3/8$, $u^{\bar{3}m}_{ideal} = 1/4$). The tetrahedral site cations i.e. the A site cations split into two crystallographically independent sites a and c with Wyckoff multiplicity 4. This kind of ionic movement breaks the centrosymmetricity by changing the tetrahedral volume, bond lengths, bond angles and coordination symmetry of the polyhedra [64–67].

Through any one of the B site cations, three different chains of tetrahedra can run in three dimension as shown in Fig. 1.15 (a). The pyrochlore B sublattice

projected on to any one of crystallographic planes gives rise to checker-board patten [cf. Fig. 1.15 (b)] whereas projecting this lattice on a plane perpendicular to any of the three tetrahedron chain directions gives the Kagome lattice [cf. Fig. 1.15 (c)].

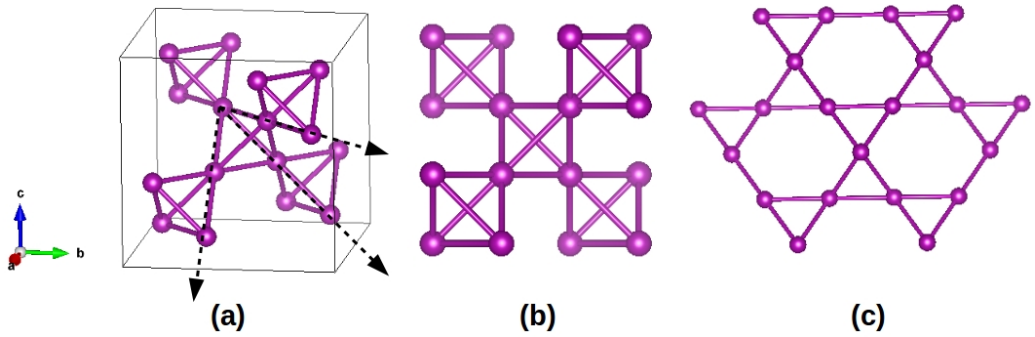

Figure 1.15: Pyrochlore B sublattice. (a) Corner linked B tetrahedra forming pyrochlore lattice. Three arrows represents the directions of three tetrahedra chains. (b) B sublattice projected on any of the crystallographic planes making checker-board pattern. (c) B sublattice projected on a plane normal to any of the chain directions making Kagome lattice.

Spinels go through structural phase transitions on lowering the temperature gradually. Cubic spinels go through cubic to tetragonal to orthorhombic phases on lowering the temperature e.g. $NiCr_2O_4$ exhibits this kind of structural phase transition from cubic to tetragonal symmetry at $\sim$ 310 K [68].

Frustration in spinel structures

Competing interaction i.e. frustration is a characteristic which makes any system unable to satisfy all pairwise interactions and any long range ordering. As a result degenerate ground states like spin liquid, spin glass states are produced [69, 70]. Frustration in spinel structure can be either on A sublattice which is bipartite consisting of two sublattices or on B sublattice which forms pyrochlore lattice and is non-bipartite.

♣ *Frustration at B sublattice: Pyrochlore lattice*

Pyrochlore lattice is formed with the 3D network of corner linked tetrahedra of B sublattice as shown in Fig. 1.15. The 2D form of this pyrochlore lattice is realized as Kagome lattice as shown in Fig. 1.15 (c). The corner linkage of tetrahedral arrangement of B sublattice, gives rise to frustration in the system.

In spinel structure AB_2O_4, containing magnetic ions at B sites, the magnetic ordering is dominated by geometric frustration driven by nearest neighbour

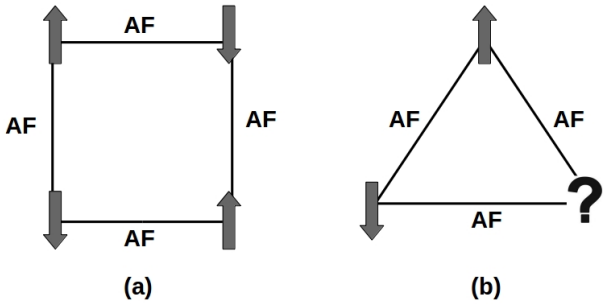

Figure 1.16: (a) Antiferromagnetic (AF) spin interaction on a bipartite lattice : unfrustrated spins. (b) AF spin interaction on a triangular lattice : geometrically frustrated spins.

(NN) antiferromagnetic interactions [71]. Together with the geometrically frustrated NN antiferromagnetic interactions, the next nearest neighbour (NNN) exchange interactions, antisymmetric Dzyaloshinskii-Moriya exchange, dipolar interactions, and magnetoelastic couplings, all become important to develop the spin-spin correlations leading to the unconventional magnetic and thermodynamic behaviours [72]. Lacking any long-range magnetic order, geometrically frustrated pyrochlore lattice systems show nature of spin-liquid, spin-glass, or disordered spin-ice states.

The root ideas of geometrical frustration can be easily caught in context of magnetism. This can be described by the spins on the vertices of a triangular lattice where antiferromagnetic (AF) spin interaction is favoured for nearest neighbour (NN) interaction. Fig. 1.16 (a) shows AF interaction on a bipartite lattice and 1.16, (b) shows the AF interaction on a triangular motif where for all bonds it is impossible to satisfy AF interaction simultaneously [71]. Once the first two spins align in antiparallel direction, the third one becomes frustrated because its two possible orientations, up and down, give the same energy and as a result the ground state becomes highly degenerate. Three interacting spins have six equal energy lowest states instead of having single lowest state and as the number of such triangles for a system grows, the number of equal energy states grow exponentially fast. The AF interacting spins on the vertices of a tetrahedron also experience frustration as the basic interacting unit is triangle here also.

♣ *Frustration at A sublattice: Diamond lattice*

Frustrated A sublattice is a diamond lattice. As mentioned earlier diamond lattice is made up of two interlacing fcc lattices at (0,0,0) and (1/4,1/4,1/4) position and can be viewed as the 3D analog of a honeycomb lattice. Fig. 1.17 shows a diamond lattice in which the A site atoms of two different fcc lattices are coloured differently.

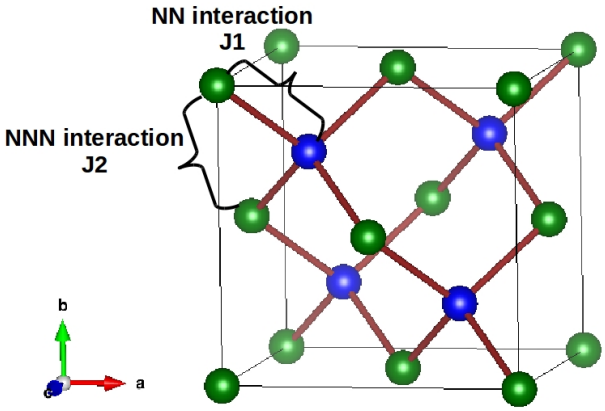

Figure 1.17: Frustrated A sublattice : Diamond lattice. Green and blue A site atoms correspond to two different interlacing fcc lattices. The B site cations and X anions are omitted for clarity. Nearest neighbour (NN) and next nearest neighbour (NNN) interactions are marked separately.

Here the A site is occupied by the magnetic atom which is tetrahedrally coordinated. In a diamond lattice there are 4 nearest neighbour (NN) interactions $J1$, between two adjacent magnetic ions on separate fcc sublattices and 12 next nearest neighbour (NNN) interactions $J2$, between two adjacent magnetic ions of the same fcc sublattice [cf. Fig. 1.17]. The superexchange interaction between two adjacent magnetic ions follow the A-X-B-X-A pathways. The 4 NN interactions are coupled through six A-X-B-X-A exchange paths including nearly rectangular X-B-X bonds of nonmagnetic ions and the 12 NNN interactions are coupled through two equivalent A-X-B-X-A exchange paths including X-B-X bonds [69,70]. Frustration in the system comes due to the competition between NN and NNN exchange interactions. An antiferromagnetic diamond lattice having only NN interaction ($J1$) is not frustrated but inclusion of NNN interaction ($J2$) introduces frustration in the system. As the NNN AFM interaction $J2$ involves two adjacent magnetic ions of a same fcc lattice, the basic coordination of interacting A site cation becomes triangular lattice which certainly sets in frustration into the system.

Thus frustration in diamond lattice is different from geometrically frustrated B sublttice which forms a pyrochlore lattice where the observed frustrations are inherently geometric in nature. Diamond lattice is rather antiferromagnetic NNN exchange interaction driven frustrated system.

Determination of frustration:

Frustration of a magnetic material can be measured by its response to an applied magnetic field. Fig. 1.18 shows temperature dependence of inverse magnetic

susceptibility for three different types of materials.

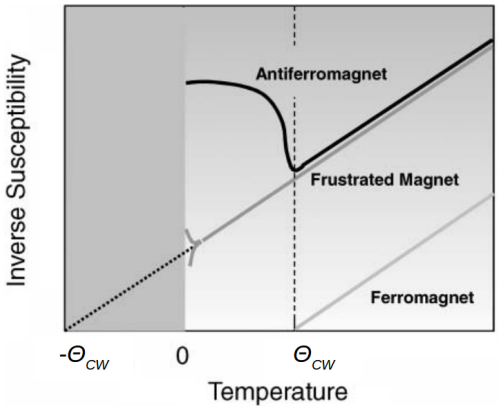

Figure 1.18: Temperature dependence of inverse susceptibility for ferromagnet, frustrated magnet and antiferromagnet. Fig. is taken from Ref. [71].

The high temperature behaviour follows the Curie-Weiss law, $\frac{1}{\chi(T)} = \frac{(T-\Theta_{CW})}{C}$, where C is a constant, proportional to atomic moment and Θ_{CW} is the Curie-Weiss temperature. Energy of two interacting spins is $JS_i.S_j$ where S is the spin magnetic moment vector and J is the interaction energy. Thus for AFM interaction $\chi(T)$ will have negative intercept and for FM interaction it takes positive sign. Geometrically frustrated systems posses AFM interaction but frustration precludes any long-ranged magnetic ordering thus any unique ground state can not be found. The transition temperature value of suppressed long range order, obtained by extrapolation of high temperature mean field behaviour, defines the frustration parameter, as $f = |\Theta_{CW}|/T_C$, where Θ_{CW} is the Curie-Weiss temperature and T_C is ordering or freezing temperature. This parameter is used to measure the frustration in a system qualitatively. A suggested empirical scheme given by terHaar and Lines as follows shows the degree of frustration of a system [73].

(i)	$f = 1$	unfrustrated
(ii)	$1 < f < 10$	moderate frustration
(iii)	$f > 10$	strong frustration

The experimental observations of $ZnCr_2O_4$ gives Θ_{CW} = -390 K and f = 24, showing highly frustrated behaviour [74], for $CoAl_2O_4$ $f \approx$ 10-20 [70] and for $MnSc_2S_4$ $f \approx 12$ [69].

Bergman *et al.* have figured out theoretically that the ground state of a diamond lattice is a Néel phase with antiparallel spins coupled through nearest-neighbour interaction in weakly frustrated limit $0 \leq J2/J1 \leq 1/8$. The ground

state changes depending on the ratio of $J2/J1$ and it becomes spiral-spin liquid for $J2/J1 > 1/8$. Thus for larger $J2$, the Néel phase becomes degenerate set of coplanar spin spirals [75]. For an example, the reported values of $J1$ and $J2$ of $CoAl_2O_4$ are 0.92 meV and 0.101 meV respectively. Thus $J2/J1 = 0.11$ for $CoAl_2O_4$ which suggests to fall it in the critical region between AFM and spiral spin-liquid states [76].

1.4.3 A and B site ordered double double perovskite

The uncommon cation ordering in both A and B sublattices in doubly ordered (double-double) perovskites takes the general chemical formula $AA'BB'O_6$ where A, A′ are the rare-earth/alkaline elements and B, B′ are transition metal elements. In the general structural framework of DDPs the A/A′ site cations have layered ordering and the B and B′ have rock-salt ordering which provide additional degrees of freedom over simple double perovskites [77]. It is also observed that layered ordering at A site cation is only seen in presence of rock-salt ordering of B sites for the case of stoichiometric perovskites. The crystal structure of such DDP is shown in Fig. 1.19.

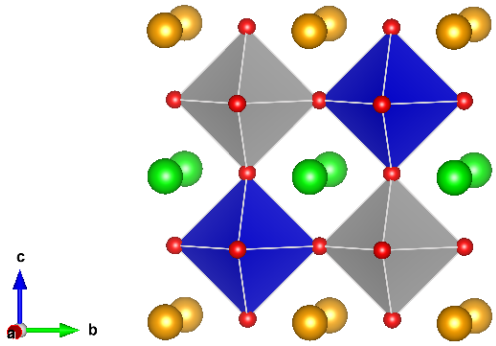

Figure 1.19: Crystal structure of an ideal $AA'BB'O_6$ perovskite with layered ordering at A/A′ and rock-salt ordering at B/B′ sites. Orange and green balls represent cations at A and A′ sites respectively. Blue and grey polyhedra represent BO_6 and $B'O_6$ octahedra respectively.

The unusual layered ordering in A sublattice leads to bond instability which is being stabilized by second-order Jahn-Teller (SOJT) distortion of highly charged B′ (d^0) cation. The presence of SOJT distortion of B′ site and the magnetic ions make the compounds enable to exhibit multiferroicity. Recently under high pressure and temperature condition a new class of DDPs is synthesized with the general chemical formula $AA'_{0.5}A''_{0.5}BB'O_6$. This structure consists of columnar motif at A sites and rock-salt motif at B sites as shown in Fig. 1.20. This crystal structure consists of five independent cation sites, A, A′, A″, B and B′, hosting

rare-earth or alkaline-earth ion at A site, $3d$ transition metals at A′, A″ and B sites, and $5d$ transition metal at B′ site. High temperature and pressure conditions compels small magnetic cations like Mn^{2+} to stabilize at A sites instead of large nonmagnetic cations like Sr^{2+} and Ca^{2+}. Thus A site magnetism gets introduced into the system. The small magnetic A site cations have tetrahedral and square planar coordination instead of usual dodecahedral coordination of A site cations.

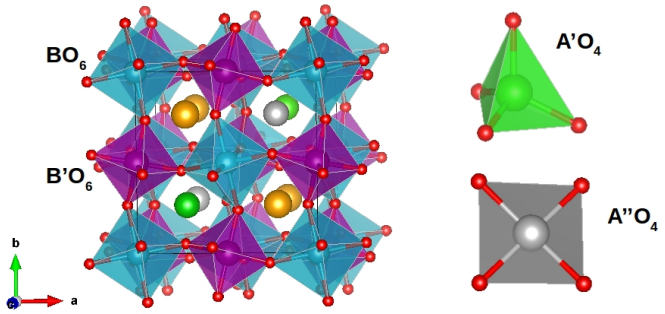

Figure 1.20: Crystal structure of $AA'_{0.5}A''_{0.5}BB'O_6$ perovskite with columnar ordering at A/A′ and rock-salt ordering at B/B′ sites is shown in the left panel. Orange balls represent nonmagnetic A site cations. Blue and purple octahedra show rock-salt arrangement of B sites. Green and grey balls represent cations at A′ and A″ sites respectively. The right panel shows the tetrahedral and square planar coordination of A′ and A″ cations respectively.

This particular ordering at A and B sublattices changes the unit cell to $\sqrt{2}a_p * \sqrt{2}a_p * 2a_p$ where a_p is the unit cell lattice parameter of cubic perovskite with $Pm\bar{3}m$ symmetry. Thus the DDPs take tetragonal symmetry with space group $P4/nmm$. The cation size mismatch and octahedral tilting further reduce the symmetry [78] . Most of the synthesized DDPs under high temperature and pressure conditions are reported to have polar space group. The polar space group symmetry allows these compounds to exhibit ferroelectricity and piezoelectricity. As already mentioned the family of DDPs possesses interesting magnetic properties. Several compounds of $AA'MnWO_6$ family show antiferromagnetic ordering, driven by Mn-O-W-O-Mn superexchange interaction with Néel temperatures ranging from 6-15 K [40]. Compounds of $AA'MgWO_6$ family show paramagnetic nature down to 2 K which remains intact in the presence of magnetic rare-earth ions at A′ site [52, 79].

1.4.4 Oxygen deficient compound of perovskite

The structural and compositional flexibility of perovskite family encourage to design oxygen deficient compound of perovskites as the transition metal cation can accommodate variable valency states. In recent years the oxygen deficient

compounds of perovskites with general chemical formula $A_mB_mO_{3m-x}$ (m is integral number perovskite blocks in unit cell and x is an integer) are in focus of attention due to their various interesting properties. They can be multiferroic, exhibit antiferromagnetism, high-temperature superconductivity, metal-insulator transition, large magnetoresistance effect etc. Playing with oxygen vacancy in perovskites i.e. Oxygen Engineering is an efficient tool to create new superstructures. This term was coined by M. Korppien and H. Yamauchi. The process of oxygen engineering produces new superstructures controlling the precise oxygen content which tailors the properties of functional oxides with optimized performance. The anionic sublattice under reduction atmosphere gives rise to oxygen deficient compounds. These types of reactions are highly topotactic as the reactivity and nature of final reduction products are determined by the crystal structure of the parent compound [80]. The properties of these hypostoichiometric compounds depend on the nature of A and B cations and the particular ordering of the oxygen vacancies [81]. Few examples of oxygen deficient compounds are $Ca_2Mn_2O_5$ [82, 83], $La_2Ni_2O_5$ [84], $Ca_2Co_2O_5$ [85] etc.

♣ *Oxygen vacancy pattern and crystal structure*

Oxygen vacancy is represented by $V_{\ddot{O}}$ in Kröger - Vink notation [86]. Anderson *et al.* [87] have examined six unique vacancy patterns for $A_2B_2O_5$ ($m = 2$, $x = 1$), five for $A_3B_3O_{9-x}$ ($m = 3$, $x = 1$, 2 or 3) and two for $A_4B_4O_{11}$ ($m = 4$, $x = 1$). Generally oxygens are removed from $[100]_c$ or $[110]_c$ rows or $(001)_c$ planes [cf. Fig. 1.21].

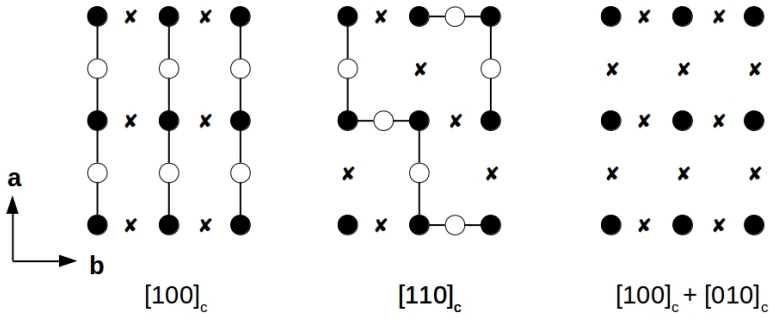

Figure 1.21: Common oxygen defect patterns in oxygen deficient compounds of perovskites. Solid black circles, empty circles and crosses represent B site cations, oxygen atoms and oxygen defects respectively.

Oxygen removal from $[100]_c$ gives rise to BO_5 square pyramids or BO_4 square planes. Oxygen vacancy along $[110]_c$ and $(001)_c$ leads to the formation of BO_4 tetrahedra and BO_5 square pyramids respectively [87]. The most common crystal structure is brownmillerite when the general chemical formula of oxygen deficient

compound becomes $A_2B_2O_5$ ($m = 2$). This kind of crystal structure is found in Ca_2FeAlO_5 [88], $Ca_2Fe_2O_5$ [89], $Ca_2Mn_2O_5$ [90] and may more. The crystal structure of brownmillerites is orthorhombic and its unit cell parameters are related to the unit cell parameter (a_p) of cubic perovskite as, $a = c = \sqrt{2}a_p, b = 4a_p$ [91]. In the following Fig. 1.22 the schematic diagram of brownmillerite formation from perovskite is shown along with different coordination of B cation.

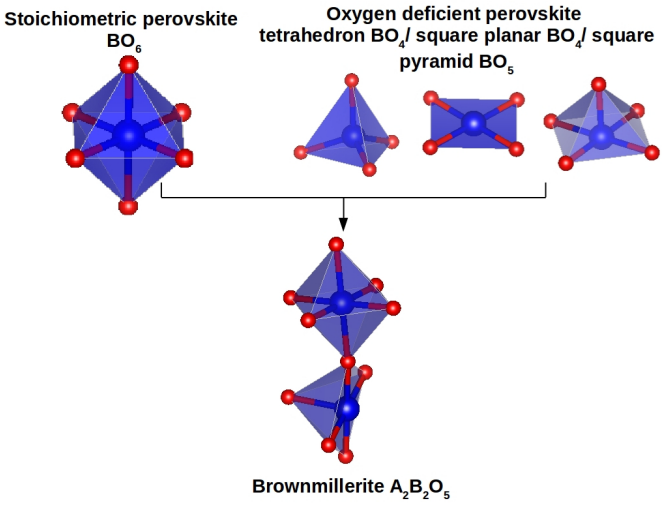

Figure 1.22: Schematic diagram of brownmillerite formation with any one of the different polyhedra coordination of B cation.

The ordered oxygen vacancy results in alternating layers of corner sharing BO_6 octahedra and BO_5 square pyramid (or BO_4 tetrahedron or square plane). Anionic size mismatch is incorporated by Goldschmidt's t factor and for $t < 1$ structural distortions are observed. The crystal structures of $Ca_2Mn_2O_5$ and $La_2Ni_2O_5$ are shown in Fig. 1.23 as examples. $Ca_2Mn_2O_5$ crystallizes in orthorhombic symmetry and the oxygen removal from [001] rows gives rise corner-sharing network of MnO_5 square pyramids [cf. Fig. 1.23 (a)]. Similar structure type is observed for $La_2Cu_2O_5$ [92] and $Ba_2Bi_2O_5$ [93]. For $La_2Ni_2O_5$, the crystal stucture is tetragonal and oxygen atoms are removed from [100] rows resulting in corner-sharing network of NiO_6 octahedra and NiO_4 square planes [cf. Fig. 1.23 (b)] [87].

♣ *Mixed anion chemistry*

Anion ordering plays an important role to tune the properties of perovskite oxides. Along with the oxygen deficient compounds, mixed anion compounds are drawing attention in solid state physics community for their unique properties

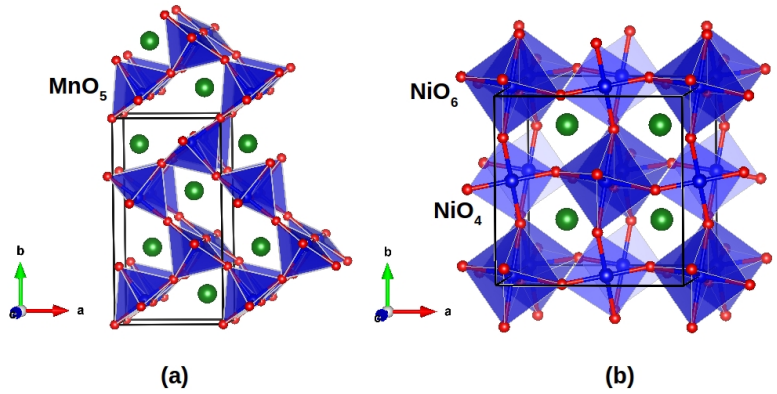

Figure 1.23: (a) Crystal structure of $Ca_2Mn_2O_5$ and (b) $La_2Ni_2O_5$. Green and red balls represent A site cations and oxygen atoms respectively. Blue polyhedra represent different coordination of B site cation.

though they are less explored till date. The anion-centered strategy allows to design new class of materials with multiple anions. Mixed anion compounds combine different anions in a single phase, such as oxyfluorides (O-F), oxynitrides (O-N), oxysulfides (O-S) etc. Mixed anion compounds also incorporate S-Se, S-Te, Se-Te, F-S, F-P anion combinations [94–98]. In comparison to the compounds containing single anions, compounds with multiple anions have a range of structures with unique properties by changing bond angles, bond distances and coordination numbers which add new dimensions to tune the properties [99]. For example fluorination of thin film $SrFeO_{3-x}$ decreases its electrical resistivity hugely [100]. Among all kinds of mixed anion compounds those containing fluoride ions have attracted much attention due to the high electronegativity and large reactivity of fluoride ions which improve the nature of the structural arrangement and charge density carried by polarizable cations to some degree [101]. Fluorine is the most suited foreign element to dope oxides beause of its comparable ionic radius (r_{F^-} = 1.33 Å) to that of oxygen ($r_{O^{2-}}$ = 1.40 Å). In these compounds the metal cation makes bonding with more than one anionic ligand and makes a heteroleptic polyhedron [94]. Incorporation of a different type of anion in a system is easier for oxygen deficient compound of perovskites as they already offer vacancy patterns. Adding a second anion in the system of oxygen deficient compounds of perovskites completes the corner sharing octahedral network of metal cation in 3D. Compounds with multiple anions show multiferroicity, metal-insulator transition, antiferromagnetism, hybrid improper ferroelectric nature etc. which are worthwhile to explore.

1.5 Overview of the present thesis

The above discussion clearly suggests that TMOs with different structural geometries exhibit various novel functionalities. Investigation of these compounds at microscopic level is necessary to understand the underlying chemistry behind the interesting properties. Density functional based first principles calculations give a complete understanding of different magnetic ordering, orbital degrees of freedom, charge states, and electronic properties which can also lead to design new materials with targeted properties. DFT calculations supplemented with model study enable us to have a complete understanding of the underlying physical and chemical processes.

In the present thesis we have studied different transition metal oxides to explore their different unique properties. The overview of different chapters of the thesis is as follows:

Chapter 2: This chapter contains all the theoretical methods we have carried out in the thesis. Discussions are made on density functional theory based calculation and its implementation to solve many-body Hamiltonian. Different basis sets used to study different properties are also discussed here. We also discussed the construction of low energy few band model Hamiltonian and its solution through exact diagonalization technique and Monte Carlo simulation to extract the physical properties. This chapter also contains the description of genetic algorithm used to predict the crystal structure of a material theoretically in more accurate manner.

Chapter 3: This chapter is devoted to study the oxygen deficient counterparts of well known perovskite $CaMnO_3$, using density functional theory based calculations. In this joint theoretical-experimental study we carried out calculations on the oxygen deficient compounds namely $CaMnO_{2.5}$ and $CaMnO_2$ with varying Mn valency.

We probed the local structure analysis of oxygen deficient $CaMnO_2$. Our study shows that a locally phase separated structure with locally ordered regions terminated by antiphase boundaries becomes favoured over disordered rock-salt structure with average occupancy of sites by Ca and Mn atoms. The microscopic origin of stabilization of such locally phase separated structure was found to be caused by an increased Mn-O covalency as well as Mn-Mn magnetic exchange interactions at antiphase boundary.

We have also studied the oxygen deficient compound $CaMnO_{2.5}$ with its square pyramidal environment of Mn instead of octahedral one. Mixed anion chemistry is also studied incorporating F as the foreign element into the system. Our study established the stabilization of unique up-up-down-down magnetic configuration in the un-flourinated compound with strong magneto-structural coupling. Upon

fluorination, we found that F occupies both the interstitial site of the missing oxygen position of metal-oxygen octahedra, driven by the tendency of Mn to be in octahedral environment instead of square pyramidal environment as well as the substitutional oxygen site in the square pyramid. This results in Mn valency in fluorinated compound close to 3+. All these make $Ca_4Mn_4O_9F_3$ compound as the most preferred fluorinated counterpart. The resultant fluorinated structure breaks the inversion symmetry of the crystal, through off-centric movement of F atom in the interstitial, which makes the compound polar with finite polarization. This together with strong magneto-structural coupling holds promise of the compound to be high temperature multiferroic.

Chapter 4: In this chapter we have carried out calculations on B site ordered double perovskite Sr_3OsO_6 to explore its reported high T_C ferromagnetic insulating behaviour in cubic symmetry. Our first principles calculation in conjunction with genetic algorithm establishes monoclinic symmetry as the most preferred symmetry of Sr_3OsO_6 suggesting the role of its epitaxial growth on $SrTiO_3$ substrate as the driving cause of its reported cubic symmetry. We made a comparative Wannier function of orbital overlap constructing low energy few band Os t_{2g} based Hamiltonian for most preferred monoclinic symmetry and reported cubic symmetry of Sr_3OsO_6. Wannier function overlaps for nearest-neighbour interaction show a well defined connected path between two Os atoms across the face of the cube in cubic symmetry which becomes misaligned in the monoclinic symmetry due to structural deviation. Solution of low energy Os t_{2g} based model Hamiltonian through exact diagonalization technique proves the stabilization of FM ordering in cubic phase with high-temperature scale associated with it. Our electronic structure calculation also reveals the origin of insulating behaviour of ferromagnetic Sr_3OsO_6 which is driven by the opening of a Mott gap in the half-filled spin-orbit coupled $j = 3/2$ manifold of d^2 Os.

Chapter 5: This chapter contains the study of doubly ordered perovskites $CaMnMReO_6$ (M = Ni/Co) which show rich magnetism with high moment in multiple magnetic sublattice system. The tetragonal crystal structure of stoichiometric $CaMnMReO_6$ with 5 independent cationic sites holds interesting magnetic and electronic properties. Our electronic structure calculation agrees well with reported ferromagnetic and ferrimagnetic ground state of $CaMnNiReO_6$ and $CaMnCoReO_6$ compound respectively. Our DFT based calculations armed with low energy model Hamiltonian reveals the role of the interplay of hybridization-driven multi sublattice double-exchange and superexchange mechanisms depending on the position and filling of d energy states, on the magnetism of these compounds. We also performed Monte Carlo simulation on the spin Hamiltonian plugging in the DFT derived coupling constants of double exchange (D's) and superexchange (J's) interactions to capture the temperature dependency on mag-

netization. Results of our Monte Carlo study also agree well with the ground state magnetic configurations of the Ni and Co compounds. It shows total magnetic moment of 28 μ_B and 12 μ_B for the Ni and Co compound unit cell respectively supporting the nominal valence of the magnetic cations. Calculated transition temperature T_C from the point of inflection of the temperature vs. magnetization curve also agrees well with the reported T_C values of both the compounds. For the Co compound the dM/dT curve shows a hump suggesting the competition between the ferro and antiferro nature of effective interactions.

We have also carried out calculations on the off-stoichiometric compounds to mimic the experimental situation by making Ni-poor and Co-rich off-stoichiometric compounds. Our study shows that ground state magnetic arrangement remains unaltered and magnetic transition temperature does not change drastically even in presence of off-stoichiometry.

Chapter 6: This chapter contains the study of the spin one ($S = 1$) diamond lattice system $NiRh_2O_4$ which goes through a phase transition from cubic to tetragonal ($c/a > 1$) at temperature $T < 440$ K. Our study on electronic structure calculation of both the cubic and tetragonal symmetry gives half-metallic solution. The tetrahedral environment of Ni breaks its d states into t_2 and e levels whereas the octahedral environment splits Rh d states into t_{2g} and e_g levels. The tetragonal distortion introduces additional splitting of Ni t_2 states and the active degrees of freedom allows spin-orbit coupling (SOC) to play an important role. Making the dominant exchange interaction paths we analysed the magnetism in the low temperature tetragonal symmetry. Our study revels nonzero Wannier overlap on nonmagnetic Rh which makes the Ni-O-Rh-O-Ni superexchange path strong. Calculated exchange interactions using DFT methods establish the presence of strong frustration in the spinel structure. Solving the single site model Hamiltonian in conjunction with DFT derived results show spin-orbit entangled singlet nonmagnetic ground state of the tetragonal symmetry. The gapped nature in the neutron scattering suggests no magnetic condensate formation due to frustration of the diamond lattice.

Chapter 7: This chapter contains the results of different novel functionalities studied at one place and we also discussed about the future scopes of these works.

Bibliography

[1] P. M. Vilarinho, 'Functional Materials: Properties, Processing and Applications', Scanning Probe Microscopy: Characterization, Nanofabrication and Device Application of Functional Materials, Springer Netherlands, 3 (2005).

[2] R. W. Cahn, 'Functional-materials', The Coming of Materials Science, Pergamon, 253 (2001).

[3] A. Planes, L. Mañosa, A. Saxena, Magnetism and Structure in Functional Materials, Springer Series in Materials Science, 79 (2005).

[4] J. A. Rogers, and J. M. DeSimone, PNAS **113**, 11667 (2016).

[5] W. Kohn and L. J. Sham, Phys. Rev. **140**, A1133 (1965).

[6] V. I. Anisimov, J. Zaanen and O. K. Andersen, Phys. Rev. B **44**, 943 (1991).

[7] V. I. Anisimov, I. V. Solovyev, M. A. Korotin, M. T. Czyżyk, and G. A. Sawatzky, Phys. Rev. B **48**, 16929 (1993).

[8] A. I. Liechtenstein, V. I. Anisimov, and J. Zaanen, Phys. Rev. B **52**, R5467 (1995).

[9] O. K. Andersen and T. Saha-Dasgupta, Phys. Rev. B **62**, R16219 (2000).

[10] A. W. Sandvik, Phys. Rev. B **59**, R14157 (1999).

[11] A. Dorneich and M. Troyer, Phys. Rev. E **64**, 066701 (2001).

[12] K. Louis and C. Gros, Phys. Rev. B **70**, 100410(R) (2004).

[13] A. R. Oganov, C. W. Glass, J. Chem. Phys. **124**, 244704 (2006).

[14] A. O. Lyakhov, A. R. Oganov, M. Valle, Modern Methods of Crystal Structure Prediction; A.R. Oganov, Eds.; Wiley-VCH Verlag GmbH & KGaA: Weinheim, Germany (2012).

[15] C. N. R. Rao, Annu. Rev. Phys. Chem. **40**, 291 (1989).

[16] H. A. Jahn, and E. Teller, Stability of Polyatomic Molecules in Degenerate Electronic States, I−Orbital Degeneracy, Proceedings of the Royal Society of London Series A, Mathematical and Physical Sciences **161**, 220 (1937).

[17] D. Khomskii, Transition Metal Compounds, Cambridge University Press, (2014).

[18] P. Fazekas, 'Lecture Notes on Electron Correlation and Magnetism', Series in modern condensed matter physics, World Scientific, (1999).

[19] J. Hubbard, Proceedings of the Royal Society of London Series A, Mathematical and Physical Sciences **276**, 238 (1963).

[20] M. Imada, A. Fujimori and Y. Tokura, Rev. Mod. Phys. **70**, 1039 (1998).

[21] K-I. Kobayashi, T. Kimura, H. Sawada, K. Terakura and Y. Tokura, Nature **395**, 677 (1998).

[22] P. Sanyal, A. Halder, L. Si, M. Wallerberger, K. Held, and T. Saha-Dasgupta, Phys. Rev. B **94**, 035132 (2016).

[23] J. B. Philipp, P. Majewski, L. Alff, A. Erb, R. Gross, T. Graf, M. S. Brandt, J. Simon, T. Walther, W. Mader, D. Topwal, and D. D. Sarma, Phys. Rev. B **68**, 144431 (2003).

[24] H. Das, P. Sanyal, T. Saha-Dasgupta, and D. D. Sarma, Phys. Rev. B **83**, 104418 (2011).

[25] J. M. De Teresa, D. Serrate, C. Ritter, J. Blasco, M. R. Ibarra, L. Morellon, and W. Tokarz, Phys. Rev. B **71**, 092408 (2005).

[26] H. L. Feng, M. P. Ghimire, Z. Hu, S.-C. Liao, S. Agrestini, J. Chen, Y. Yuan, Y. Matsushita, Y. Tsujimoto, Y. Katsuya, M. Tanaka, H.-J. Lin, C.-T. Chen, S.-C. Weng, M. Valvidares, K. Chen, F. Baudelet, A. Tanaka, M. Greenblatt, L. H. Tjeng, and K. Yamaura, Phys. Rev. Mater. **3**, 124404 (2019).

[27] S. Vasala, M. Karppinen, Progress in Solid State Chemistry **43**, 1 (2015).

[28] D. D. Sarma, P. Mahadevan, T. Saha-Dasgupta, S. Ray, and A. Kumar, Phys. Rev. Lett. **85** (2000).

[29] P. Sanyal and P. Majumdar, Phys. Rev. B **80**, 054411 (2009).

[30] L. Brey, M. J. Calderón, S. Das Sarma, and F. Guinea, Phys. Rev. B **74**, 094429, (2006).

[31] T. Saha-Dasgupta, Mater. Res. Express **7**, 014003 (2020).

[32] J. K. Asbóth, L. Oroszlány, A. Pályi, A Short Course on Topological Insulators, Springer Switzerland (2015).

[33] F. D. M. Haldane, Phys. Rev. Lett. **50**, 1153 (1983).

[34] I. Affleck, T. Kennedy, E. H. Lieb, and H. Tasaki, Phys. Rev. Lett. **59**, 799 (1987).

[35] Z.-C. Gu, X.-G. Wen, Phys. Rev. B **80**, 155131 (2009).

[36] G. A. Fieten, V. Chua, M. Kargarian, R. Lundgren, A. Rüegg, J. Wen, V. Zyuzin, Physica E **44**, 845 (2012).

[37] Q. Wang, and Q. Sun, P. Jena, and Y. Kawazoe, Phys. Chem. Chem. Phys. **12**, 1493 (2010).

[38] P. Jena, and Q. Sun, Chem. Rev. **118**, 5755 (2018).

[39] P. Zuo, C. V. Colin, H. Klein, P. Bordet, E. Suard, E. Elkaim, and C. Darieg, Inorg. Chem. **56**, 8478 (2017).

[40] G. King, S. Thimmaiah, A. Dwivedi, and P. M. Woodward, Chem. Mater. **19**, 6451 (2007).

[41] M. L. Lopez, M. L. Veiga, C. Pico, J. Mater. Chem. **4**, 547 (1994).

[42] M. A. Arillo, J. Gomez, M. L. Lopez, C. Pico, M. L. Veiga, J. Mater. Chem. **7**, 801 (1997).

[43] M. A. Arillo, J. Gomez, M. L. Lopez, C. Pico, M. L. Veiga, Solid State Ionics. **95**, 241 (1997).

[44] E. Solana-Madruga, Á. M. Arévalo-López, A. J. Dos santos-García, C. Ritter, C. Cascales, R. Sáez-Puche, and J. Paul Attfield, Phys. Rev. B **97**, 134408 (2018).

[45] G. M. McNally, A. M. Arévalo-López, P. Kearins, F. Orlandi, P. Manuel and J. P. Attfield, Chem. Mater. **29**, 8870 (2017).

[46] D. Khomskii, Am. Phys. Soc., Physics **2**, 20 (2009).

[47] C. Ederer and N. A. Spaldin, Phys. Rev. B **71**, 224103 (2005).

[48] S. W. Cheong and M. V. Mostovoy, Nat. Mater. **6**, 13 (2007).

[49] H. Schmid, J. Phys. Condens. Matter **20**, 434201 (2008).

[50] B. B.van Aken, T. T.M. Palstra, A. Filippetti, and N. A. Spaldin, Nat. Mater. **3**, 164 (2004).

[51] T. Kimura, T. Goto, H. Shintani, K. Ishizaka, T. Arima, and Y. Tokura, Nature **426**, 55 (2003).

[52] G. King, and P. M. Woodward, J. Mater. Chem. **20**, 5785 (2010).

[53] M. Azuma, S. Kaimori, M. Takano, Chem. Mater. **10**, 3124 (1998).

[54] P. J. Saines, B. J. Kennedy, M. M. Elcombe, H. H. Harris, L -Y. Jang, Z. Zhang, J. Solid State Chem. **181**, 2941 (2008).

[55] J-H. Park, J.B. Parise, P.M. Woodward, I. Lubomirsky, O. Stafsudd, J. Mater. Res. **14**, 3192 (1999).

[56] M. W. Lufaso, and P. M. Woodward, Acta Crystallographica Section B **60**, 10 (2004).

[57] P. G. Radaelli, New J. Phys. **7**, 53 (2005).

[58] W. H. Bragg, Nature **95**, 561 (1915).

[59] F. Walz, J. Phys.: Condens. Matter **14**, R285 (2002).

[60] D. J. Singh, M. Gupta, R. Gupta, Phys. Rev. B. **63**, 205102 (2001).

[61] C. Urano, M. Nohara, S. Kondo, F. Sakai, H. Takagi, T. Shiraki, and T. Okubo, Phys. Rev. Lett. **85**, 1052 (2000).

[62] Z. Szotek, W. M. Temmerman, D. Kdderitzsch, A. Svane, L. Petit, and H. Winter, Phys. Rev. B **74**, 174431 (2006).

[63] K. M. Rabe, Annu. Rev. Condens. Matter Phys. **1**, 211 (2010).

[64] L. Hwanq, A. H. Heuer and T. E. Mitchel, On the space group of $MgAl_2O_4$ spinel, The Philosophical Magazine: A Journal of Theoretical Experimental and Applied Physics **28**, 241 (1973).

[65] L. Gastaldi, and L. Scaramuzza, Acta Cryst. B **35**, 2283 (1979).

[66] K. E. Sickafus, and J. M. Wills, J. Am. Ceram. Soc. **82**, 3279 (1999).

[67] N. W. Grimes, P. Thompson, and H. F. Kay, Proc. R. Soc. Lond. A **386**, 333 (1983).

[68] H. Ishibashi, T. Yasumi, J. Magn. Magn. Mater. **310**, e610 (2007).

[69] V. Fritsch, J. Hemberger, N. Bttgen, E.-W. Scheidt, H.-A. Krug von Nidda, A. Loidl, and V. Tsurkan, Phys. Rev. Lett. **92**, 116401 (2004).

[70] N. Tristan, J. Hemberger, A. Krimmel, H-A. Krug von Nidda, V. Tsurkan, and A. Loidl, Phys. Rev. B **72**, 174404, (2005).

[71] A. P. Ramirez, MRS Bulletin **30**, 447 (2005).

[72] V. O. Garlea and B. C. Chakoumakos, Exp. Methods Phys. Sci. **48**, 203 (2015).

[73] A. P. Ramirez, Czechoslovak J. Phys. **46**, 3247 (1996).

[74] D. Fiorani, S. Viticoli, J. L. Dormann, J. L. Tholence, and A. P. Murani, Phys. Rev. B **30**, 2776 (1984).

[75] D. Bergman, J. Alicea, E. Gull, S. Trebst, and L. Balents, Nat. Phys. **3**, 487 (2007).

[76] B. Roy, A. Pandey, Q. Zhang, T. W. Heitmann, D. Vaknin, D. C. Johnston, and Y. Furukawa, Phys. Rev. B **88**, 174415 (2013).

[77] C. De and A. Sundaresan, Phys. Rev. B **97**, 214418 (2018).

[78] M. C. Knapp, P. M. Woodward, J. Solid State Chem. **179**, 1076 (2006).

[79] G. King, L. M. Wayman, P. M. Woodward, J. Solid State Chem. **182**, 1319 (2009).

[80] A. Varela, S. de Dios, M. Parras, M. Hernando, M. T. Fernández-Díaz, A. R. Landa-Cánovas, and J. M. González-Calbet, J. Am. Chem. Soc. **131**, 8660 (2009).

[81] J. Du, T. Zhang, F. Cheng, W. Chu, Z. Wu, and J. Chen, Inorg. Chem. **53**, 9106 (2014).

[82] K. R. Poeppelmeier, M. E. Leonowicz, J. M. Longo, J. Solid State Chem. **44**, 89 (1982).

[83] K. R. Poeppelmeier, M. E. Leonowiez, J. C. Seanlon, J. M. Longo, W. B. Yelon, J. Solid State Chem. **45**, 71 (1982).

[84] C. N. R. Rao, K. Gopalakrishnan, K. Vidyasagar, A. K. Ganguli, A. Ramanan, L. Ganapathi, J. Mater. Res. **1**, 280 (1986).

[85] K. Vidyasagar, J. Gopalakrishnan, C. N. R. Rao, Inorg. Chem. **23**, 1206 (1984).

[86] W.L. Warren, K. Vanheusden, D. Dimos, G. E. Pike, and B. A. Tuttle, J. Am. Ceram. Soc. **79**, 536 (1996).

[87] M. T. Anderson, J. T. Vaughey, and K. R. Poeppelmeier, Chem. Mater. **5**, 151 (1993).

[88] A. A. Colville, and S. Geller, Acta Cryst. B **27**, 2311 (1971).

[89] I. Kagomiya, Y. Hirota, K. Kakimoto, K. Fujii, M. Shiraiwa, M. Yashima, A. Fuwa and S. Nakamura, Phys. Chem. Chem. Phys. **19**, 31194 (2017).

[90] Y. Lu, F. Lu, Z. Yang, J. Wu, H. Yu, X. Xie, J. Xu, F. Cheng, J. Chen, K. Xiong, H. Liu, W.-H. Wang, J. Zhao, and W. Wang, AIP Adv. **6**, 095210 (2016).

[91] A. M. Abakumov, M. G. Rozova, E. V. Antipov, Russ. Chem. Rev. **73**, 847 (2004).

[92] J. F. Bringley, B. A. Scott, S. J. LaPlaca, N. F. Boehme, T. M. Shaw, W. W. McElfresh, S. S. Trail, D. E. Cox, Nature **347**, 263 (1990).

[93] P. Lightfoot, J. A. Hriljac, S. Pei, Y. Zhang, A. W. Mitchell, D. R. Richards, B. Dabrowski, J. D. Jorgensen, D. G. Hinks, J. Solid State Chem. **92**, 473 (1991).

[94] H. Kageyama, K. Hayashi, K. Maeda, J. P. Attfield, Z. Hiroi, J. M. Rondinelli, and K. R. Poeppelmeier, Nat. Commun. **9**, 772 (2018).

[95] Z.-Z. Luo, C.-S. Lin, W.-L. Zhang, H. Zhang, Z.-Z. He, and W.-D. Cheng, Cryst. Eng. Comm. **16**, 2788 (2014).

[96] C. F. Smura, D. R. Parker, M. Zbiri, M. R. Johnson, Z. A. Gál, and S. J. Clarke, J. Am. Chem. Soc. **133**, 2691 (2011).

[97] H. Hiramatsu, H. Yanagi, T. Kamiya, K. Ueda, M. Hirano, and H. Hosono, Chem. Mater. **20**, 326 (2008).

[98] J. A. Armstrong, E. R. Williams, and M. T. Weller, J. Am. Chem. Soc. **133**, 8252 (2011).

[99] S. T. Hartman, S. B. Cho, and R. Mishra, Inorg. Chem. **57**, 10616 (2018).

[100] E. J. Moon, A. K. Choquette, A. Huon, S. Z. Kulesa, D. Barbash, and S. J. May, APL Mater. **3**, 062511 (2015).

[101] A. Demourgues, A. Tressaud, H. Laronze, P. Gravereau, P. Macaudière, J. Fluor. Chem. **107**, 215 (2001).

Chapter 2

Theoretical methods

In this chapter, the theoretical methods, used for electronic structure calculation, crystal structure prediction and thermodynamic properties to reveal different novel functional properties of transition metal oxides are discussed.

Our electronic structure calculations are mainly based on density functional theory (DFT) based first principles calculations. The conventional *ab-initio* method of calculations are used to understand the electronic properties at zero Kelvin ($T = 0$ K). In order to account for electron-electron correlation effect, we adopt two approaches. First, it is dealt within mean field scheme of DFT+U approach. In second approach, we apply supplemented Hubbard U and Hund's coupling J_H to handle the multi-orbital situation within a tight-binding model, derived from *ab-initio* calculation. With the help of N^{th} order muffin-tin orbital method the hopping integrals, onsite energies of the single particle part of the many-body Hamiltonian are extracted from DFT calculations in energy selective manner which is solved using exact diagonalization technique.

To predict the crystal structure of a compound, genetic algorithm is used with DFT total energies as input. For finite temperature calculation of thermodynamic properties, Monte Carlo simulation is carried out on model Hamiltonian.

In the following sections the methods and their background are discussed in detail.

2.1 Many-body Hamiltonian

Understanding of physical and chemical properties of a material at microscopic level is very important. For this understanding, the electronic structure calculation is necessary as electrons govern most properties. Systems like atoms, clusters, solids all are made up of mutually interacting particles, namely electron and nuclei. Matter can be thought as a collection of interacting particles under an influencing external field. Thus any system can be described as the interaction of heavy positively charged particles i.e. nuclei and lighter negatively charged

particles i.e. electrons via coulombic, electrostatic forces. The Hamiltonian of such an interacting system can be written as follows,

$$H = -\sum_{I=1}^{P} \frac{\hbar^2}{2M_I}\nabla_I^2 - \sum_{i=1}^{N} \frac{\hbar^2}{2m}\nabla_i^2 + \frac{e^2}{2}\sum_{I=1}^{P}\sum_{J\neq 1}^{P} \frac{Z_I Z_J}{|\boldsymbol{R_I} - \boldsymbol{R_J}|} + \frac{e^2}{2}\sum_{i=1}^{N}\sum_{j\neq i}^{N} \frac{1}{|\boldsymbol{r_i} - \boldsymbol{r_j}|} - e^2\sum_{I=1}^{P}\sum_{i=1}^{N} \frac{Z_I}{|\boldsymbol{R_I} - \boldsymbol{r_i}|} \tag{2.1}$$

where, $\mathbf{R} = \{\mathbf{R}_1,.....,\mathbf{R}_P\}$, a set of P number of nuclear coordinates and $\mathbf{r} = \{\mathbf{r}_1,.....,\mathbf{r}_N\}$, a set of N electronic coordinates. The nuclear charge and mass are represented by Z_I, M_I respectively whereas these for electron are represented by e and m respectively. The first two terms of the Hamiltonian represent the kinetic energies for the nuclei (T_n) and the electrons (T_e) respectively. The last three terms represent the nucleus–nucleus (V_{nn}), electron–electron (V_{ee}), and electron–nucleus (V_{ne}) coulomb interactions respectively. The potential V_{ne} is also termed as the external potential V_{ext}. Thus Eq. (2.1) can be written as,

$$H = T_n + T_e + V_{nn} + V_{ee} + V_{ne} \tag{2.2}$$

To solve the many-body Hamiltonian the time-independent Schrödinger equation can be written as follows

$$H\Psi(\mathbf{R}, \mathbf{r}) = E\Psi(\mathbf{R}, \mathbf{r}) \tag{2.3}$$

where, E is the energy of the system and $\Psi(\mathbf{R},\mathbf{r})$ is the many body wave-function describing the state of the system which is antisymmetric on exchanging electronic coordinates in $\mathbf{r}$ and symmetric or antisymmetric on exchanging nuclear coordinates in $\mathbf{R}$. Solution of this Hamiltonian is complex as many degrees of freedom are involved. Thus it raises the need of different approximation to make it tractable.

2.1.1 Born-Oppenheimer approximation

The first proposed approximation towards simplification of the many-body Hamiltonian was the *Adiabatic approximation* or the *Born-Oppenheimer approximation* (1927) [1]. In this approximation the electronic and nuclear degrees of freedom are decoupled. Here nuclei is considered to be static due to its heavy mass compared to that of electron. Due to the fixed coordinates of nuclei the kinetic term of them are neglected and the potential energy term due to nucleus-nucleus interaction (V_{nn}) is considered as constant, called the Madelung energy. Thus the Hamiltonian in Eq. (2.2) reduces to,

$$H = h_{el} + V_{nn} \tag{2.4}$$

where, $h_{el} = T_e + V_{ne} + V_{ee}$ is the electronic Hamiltonian. In this approximation the many body Hamiltonian transforms to electron only Hamiltonian though further approximations are needed to overcome the interacting nature of electrons.

2.1.2 Independent electron approximation

In this approximation electrons are considered as independent particles moving in the mean field created by the other electrons and the nuclei. Thus this method maps the interacting electrons into a system of non-interacting electrons which effectively represents the original system. This approximation eliminates the correlated movement of one electron with respect to another electron. This single electron problem can be treated with two approaches, (i) wave-function based approach, (ii) density functional theory (DFT) based approach. Different wave-function based approaches like Hartree [2], Hartree-Fock [3], and configuration-interaction [4] require huge computational resources to capture the detailed wave function as it increases exponentially with the system size. The DFT approach [5–7] is advantageous as it is a parameter free approach and computationally quite simpler. In this thesis we have carried out our calculations based on DFT. The detailed description of this method is given below.

2.2 Density functional theory based approach

Density functional theory is one of the most powerful and successful approaches for electronic structure calculation of different class of materials. This approach deals with the total density of electrons $\rho(\mathbf{r})$ instead of many-body wave-function making the problem simpler. The many-body wave-function $\Psi(\mathbf{R}, \mathbf{r})$ being function of $3N$ (N = number of electrons) variables is thus replaced by electronic charge density $\rho(\mathbf{r})$ which is a function of $3N$ variables and can be written as follows,

$$\rho(\mathbf{r}) = N \int \Psi^*(\mathbf{r}, \mathbf{r}_2, ..., \mathbf{r}_N)\Psi(\mathbf{r}, \mathbf{r}_2, ..., \mathbf{r}_N) d\mathbf{r}_2 d\mathbf{r}_3 ... d\mathbf{r}_N \tag{2.5}$$

Thus if the ground state electron density distributions are known, the ground state properties of many-electron problem can be calculated. The mathematical formulation of this approach is based on two theorems proposed by Hohenberg and Kohn as discussed below.

2.2.1 Theorems of Hohenberg and Kohn

Theorem 1

The 1^{st} theorem of Hohenberg and Kohn (HK) states that there is a one-to-one correspondence between the external potential V_{ext} and the ground state

electron density $\rho(\mathbf{r})$ of the system. Thus the expectation value of any observable $\hat{A}$ will be the unique functional of the ground state electron density as,

$$\langle\Psi|\hat{A}|\Psi\rangle = A[\rho]$$

Proof of 1^{st} HK theorem

Let us assume two different systems, each of them having N number of electrons and characterized by two different external potentials $V_1(\mathbf{r})$ and $V_2(\mathbf{r})$. Consider two corresponding wave-functions of two systems Ψ_1 and Ψ_2 which yield the same electron density $\rho(\mathbf{r})$. Thus Schrödinger equations of these systems become,

$$\begin{aligned} H_1\Psi_1 &= E_1\Psi_1 \\ H_2\Psi_2 &= E_2\Psi_2 \end{aligned} \tag{2.6}$$

Using variational principle we can write

$$\begin{aligned} E_1 = \langle\Psi_1|H_1|\Psi_1\rangle &< \langle\Psi_2|H_1|\Psi_2\rangle \\ = \langle\Psi_2|H_2|\Psi_2\rangle + \langle\Psi_1|(H_1 - H_2)|\Psi_1\rangle \\ < E_2 + \int dr\rho(\mathbf{r})[V_1(\mathbf{r}) - V_2(\mathbf{r})] \end{aligned} \tag{2.7}$$

Thus interchanging the suffices we can also obtain

$$E_2 < E_1 + \int dr\rho(\mathbf{r})[V_2(\mathbf{r}) - V_1(\mathbf{r})] \tag{2.8}$$

These above two inequalities finally lead to the following contradiction,

$$E_1 + E_2 < E_2 + E_1 \tag{2.9}$$

Thus the assumption of getting identical electron density from two different external potential was wrong. It comes up with the conclusion that a given electron density $\rho(\mathbf{r})$ corresponds to only one external potential V_{ext} and fixing of V_{ext}, fixes the Hamiltonian and hence the wave-function by the density.

Theorem 2

This 2^{nd} HK theorem states that the ground state energy can be defined as a functional of the charge density, $E[\rho(\mathbf{r})]$. For any particular external potential, the ground state energy of the system attains the global minimum value of this energy functional, and the corresponding density, minimizing the functional is the exact ground state density.

Proof of 2^{nd} HK theorem

The many-body Hamiltonian can be written as $H = T + V + V_{ext}$ where, T, V, V_{ext} represent the kinetic energy, electron-electron interaction, the external potential with the ground state wave-function Ψ respectively. The total energy which is a functional of density $\rho(\mathbf{r})$ can be written as follows,

$$\begin{aligned} E[\rho] &= \langle \Psi[\rho]|H|\Psi[\rho]\rangle \\ &= \langle \Psi[\rho]|(T+V)|\Psi[\rho]\rangle + \langle \Psi[\rho]|V_{ext}|\Psi[\rho]\rangle \\ &= F[\rho(\mathbf{r})] + \int \rho(\mathbf{r}) V_{ext}(\mathbf{r}) d\mathbf{r} \end{aligned} \tag{2.10}$$

$F[\rho(\mathbf{r})]$ is the universal functional of charge density $\rho(\mathbf{r})$. Applying the Rayleigh-Ritz variational principle we get,

$$F[\rho(\mathbf{r})] + \int \rho(\mathbf{r}) V_{ext}(\mathbf{r}) d\mathbf{r} = E[\rho(\mathbf{r})] \geq E_0[\rho_0(\mathbf{r})] \tag{2.11}$$

where, E_0 is the ground state energy being characterized by ground state density $\rho_0(\mathbf{r})$. Thus this theorem concludes that the ground state properties of an system of N interacting electrons will be determined by the electron density and the ground state density gives the ground state energy.

To know the analytic form of the functional $F[\rho(\mathbf{r})]$ which contains all the many-body effect, it is important to determine $E[\rho(\mathbf{r})]$. Unfortunately functional $F[\rho(\mathbf{r})]$ was not known which encouraged Kohn and Sham to address the issue by giving a proper formalism which finally led to the development of modern DFT.

2.3 Kohn-Sham equations and modern DFT

In 1965 Kohn and Sham [6] gave a formalism of the unknown energy functional $F[\rho(\mathbf{r})]$ by mapping the electron density ($\rho(\mathbf{r})$) of interacting N electrons into that of a system of non-interacting electrons.

For this non-interacting system the universal functional can be written as follows,

$$F[\rho(\mathbf{r})] = T_0[\rho(\mathbf{r})] + \frac{e^2}{2} \int \frac{\rho(\mathbf{r}_1)\rho(\mathbf{r}_2)}{|\mathbf{r}_1 - \mathbf{r}_2|} d\mathbf{r}_1 d\mathbf{r}_2 + E_{xc}[\rho(\mathbf{r})] \tag{2.12}$$

where, $T_0[\rho(\mathbf{r})]$ is the kinetic energy functional for the non-interacting electrons, the 2^{nd} term is the Hartree term depicting the classical electrostatic contribution and the last term includes all the effect of many body interactions, known as exchange (xc) correlation. This xc correlation part has the expression as follows,

$$E_{xc}[\rho] = \{V_{ee}[\rho] - V_{Hartree}[\rho]\} + \{T[\rho] - T_0[\rho]\} \tag{2.13}$$

where, $T[\rho]$ is the exact kinetic energy of the interacting system. Thus the xc part captures the difference between the non-interacting electron system and the interacting electron system. Finally the energy functional can be written putting the expression of the universal functional as follows,

$$E_{KS}[\rho] = \int \rho(\mathbf{r}) V_{ext}(\mathbf{r}) d\mathbf{r} + T_0[\rho(\mathbf{r})] + \frac{e^2}{2} \int \frac{\rho(\mathbf{r})\rho(\mathbf{r}')}{|\mathbf{r} - \mathbf{r}'|} d\mathbf{r} d\mathbf{r}' + E_{xc}[\rho(\mathbf{r})] \quad (2.14)$$

Thus the corresponding Hamiltonian is,

$$H_{KS} = (-\frac{\hbar^2}{2m}) \bigtriangledown^2 + V_{eff} \quad (2.15)$$

where,

$$\begin{aligned} V_{eff}(\mathbf{r}) &= V_{ext}(\mathbf{r}) + \int \frac{\rho(\mathbf{r}')}{|\mathbf{r} - \mathbf{r}'|} d\mathbf{r}' + \frac{\delta E_{xc}[\rho]}{\delta \rho(\mathbf{r})} \\ &= V_{ext} + V_{Hartree} + V_{xc} \end{aligned} \quad (2.16)$$

The one-electron Schrödinger equation can be written as follows

$$[-\frac{\hbar^2}{2m} \bigtriangledown^2 + V_{eff}(\mathbf{r}, \rho)]\phi_i(\mathbf{r}) = \varepsilon_i \phi_i(\mathbf{r}) \quad (2.17)$$

and solving this one can find the one-electron orbital ϕ_i which minimizes the energy. The set of N-nonlinear integro-differential equations [Eq. (2.17)] are known as Kohn-Sham (KS) equations. These equations can be solved if the effective potential V_{eff} is known. To know V_{eff}, it is necessary to know $\rho(\mathbf{r})$ thus the set of orbitals ϕ_i which are the solutions of the KS equations. Thus KS equations can be solved in self-consistent iterative process as follows: a charge density value ρ_0 should be guessed to initiate the process. Then with this density initial KS Hamiltonian H_{KS1} is constructed. Solving the equation a set of ϕ_i is obtained from which a new density ρ_1 can be derived. Now if the new density ρ_1 and old one ρ_0 differ from each other by an amount more than the given critical value, the density for the next step will be then evaluated mixing the two known densities depending on the choice of mixing scheme and this procedure will go on iteratively until the density converges to its final value ρ_f which generates H_{KSf} which again gives a solution for ρ_f in self-consistent manner. The flowchart, shown in Fig. 2.1 depicts the whole procedure discussed above.

2.4 Exchange-correlation functional

Celebrated Kohn-Sham theory is exact in principle but the main problem arises to find out the exact expression of the exchange-correlation (xc) energy term and now at this point approximations are needed. Out of different successful approximations made over years, local density approximation (LDA) and generalized gradient approximation (GGA) are mostly popular and also been used in this thesis. A brief description of these two approximations are given below.

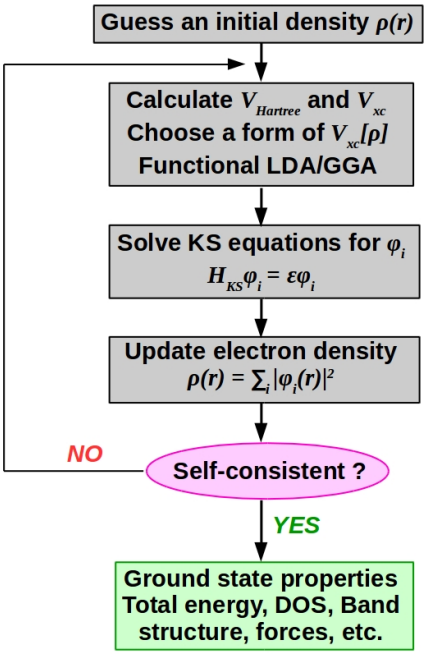

Figure 2.1: Flowchart of the self-consistent DFT procedure.

Local density approximation (LDA)

This approximation is the most commonly used approximation to get the exchange correlation energy. This particular method was introduced by Kohn and Sham [6] but the central idea was present in Thomas-Fermi-Dirac theory [8–10]. The main idea of this approximation is based on the consideration of a general inhomogeneous electronic system as locally homogeneous one. Thus it assumes that the exchange-correlation energy has only local dependency on charge density $\rho(\mathbf{r})$ [11]. The energy functional takes the form as,

$$E_{xc}^{LDA} = \int \varepsilon_{xc}^{LDA}[\rho(\mathbf{r})]\rho(\mathbf{r})d\mathbf{r} \tag{2.18}$$

where, $\varepsilon_{xc}^{LDA}[\rho(\mathbf{r})]$ represents the exchange-correlation energy density of a homogeneous electron gas with charge density $\rho(\mathbf{r})$. This exchange-correlation energy density can be splitted up into individual exchange and correlation terms as follows,

$$\varepsilon_{xc}^{LDA}[\rho(\mathbf{r})] = \varepsilon_{x}^{LDA}[\rho(\mathbf{r})] + \varepsilon_{c}^{LDA}[\rho(\mathbf{r})] \tag{2.19}$$

With Dirac's expression, the exchange energy for homogeneous electron gas becomes,

$$\varepsilon_{x}^{LDA} = -\frac{0.058}{r_s} \tag{2.20}$$

where, $r_s = (3/4\pi\rho)^{1/3}$ is the mean interatomic distance in atomic unit.

The most accurate expression for the correlation energy density obtained through quantum Monte Carlo simulation was given by Ceperley and Alder in 1980 [12]. This correlation functional is exact in numerical accuracy and further parametrization was done by Perdew and Zunger in 1981 [13], Perdew and Wang [14] for the spin polarized and spin unpolarized homogeneous electron gas.

LDA approximation was formulated for homogeneous electron gas but it remained quite successful for real materials which are far from homogeneous electron gas [15]. The reason behind this performance beyond expectation can be attributed as follows, LDA underestimates the exchange energy while overestimates the correlation energy leading to a cancellation of errors. In LDA the exact density depletion around an electron at $\mathbf{r}$ is replaced by that of the homogeneous electron gas of density $\rho(\mathbf{r})$. The region around each electron where the electronic charge density is depleted is known as exchange-correlated hole. LDA takes the exchange-correlation hole as a sphere instead of taking its actual shape but it captures the size of the xc hole correctly and as the xc energy depends on the xc hole extent, LDA remains successful in obtaining the xc energy functional. LDA yields reasonable results for many systems but it fails to explain strongly correlated systems where the electrons are well localized. It also fails to predict accurately the activation energy barriers due to overestimation of the binding energies.

Generalized gradient approximation (GGA)

In this approximation the improvement of the LDA xc energy has taken into account considering the inhomogeneity of the electron density. Unlike LDA, in GGA the functional is dependent on the spatial variation (gradient) of density instead of its local value. The xc energy in GGA can be written as,

$$E_{xc}^{GGA}[\rho(\mathbf{r})] = \int \varepsilon_{xc}[\rho(\mathbf{r}), |\bigtriangledown \rho(\mathbf{r})|]\rho(\mathbf{r})d\mathbf{r} = \int \varepsilon_{xc}[\rho(\mathbf{r})]F_{xc}[\rho(\mathbf{r}), \bigtriangledown\rho(\mathbf{r})]\rho(\mathbf{r})d\mathbf{r} \tag{2.21}$$

where, F_{xc} is the enhancement factor to modify the LDA expression according to the variation of density in the vicinity of the considered point.

Depending upon the choice of enhancement factor, different GGA's are available to use. Among all these, the functional form of F_{xc} given by Perdew-Wang (PW91) in 1990 is the most widely used one [16]. In 1996 Perdew, Burke, and Ernzerhof (PBE) proposed an exchange-correlation where the enhancement factor F_{xc} incorporates dependence on local density, magnetization density and dimensionless density gradient [17].

In comparison with LDA, GGA works better improving the binding energies, atomic energies, bond lengths and bond angles. However GGA fails to describe

long-range Van Der waals interaction and can not describe accurately strongly correlated electron systems as it fails to capture the local electron-electron correlation interaction which plays a significant role in determining the physical properties. All the drawbacks arise because in GGA, the self-interaction i.e. the interaction of electron with the field generated by itself term is not exactly cancelled out by the exchange and correlation functional and the residual effect strongly impacts the system containing localized d and f electrons. Thus for a strongly correlated system a more accurate treatment with strong correlation effect is needed.

2.5 LDA+U (Beyond DFT exchange-correlation)

Transition metal oxides and rare-earth metal compounds with well localized d electrons lead to strong onsite correlations and placing a second electron on a preoccupied site costs an energy U known as Hubbard U. The approach of combining Hubbard U with DFT calculations supplemented in LDA and GGA was given by Anisimov *et al.* in 1991 [18]. The main philosophy of this LDA+U approach lies on the replacement of the average electron-electron correlation energy by a Hubbard interaction which introduces orbital polarization in the potential.

For a system of fluctuating numbers of d electrons, the total number of electrons $N = \sum_i n_i$ is constant. The average Coulomb energy for the interacting d electrons become,

$$E = \frac{UN(N-1)}{2} \tag{2.22}$$

The total energy of the system becomes as follows by subtracting the Coulomb energy from the LDA total energy and adding the Hubbard term,

$$E_{LDA+U} = E_{LDA} - \frac{UN(N-1)}{2} + \frac{1}{2}U\sum_{i\neq i} n_i n_j \tag{2.23}$$

where, n_i is the orbital occupancy. The orbital energy can be written as,

$$\varepsilon_i = \frac{\delta E_{LDA+U}}{\delta n_i} = \varepsilon_{LDA} + U(\frac{1}{2} - n_i) \tag{2.24}$$

Thus it produces an energy shift depending on the occupancy of the orbital and opens up a gap of value U between lower and upper Hubbard subbands [cf. Fig. 2.2].

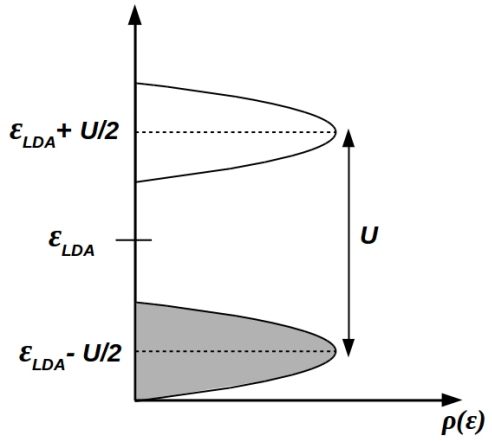

Figure 2.2: Schematic representation of the shift of occupied and unoccupied LDA orbitals in presence of U.

This method thus becomes successful in capturing the band gap opening of strongly correlated electron systems. Two popular approaches to handle multi-band Hubbard model in conjunction with LDA+U method are described in the following.

Liechtenstein method

In this method proposed by Liechtenstein *et al.* in 1995 [19], the multi-orbital phenomena in LDA+U can be defined as,

$$E_{LDA+U}[\rho^{\sigma}(\mathbf{r}), n^{\sigma}] = E_{LDA/GGA}[\rho(\mathbf{r})] + E_U[n^{\sigma}_m] - E_{dc}[n^{\sigma}] \tag{2.25}$$

where, $\rho^{\sigma}(\mathbf{r})$ is the charge density of electrons of spin σ. n^{σ}_m represents the orbital occupancy for atom in presence of onsite Hubbard interaction where m is the magnetic quantum number and $n^{\sigma} = \sum_m n^{\sigma}_m$. The rotationally invariant Hartree-Fock like term $E_U[n^{\sigma}_m]$ has the form as,

$$\begin{aligned} E_U[n^{\sigma}_m] = \frac{1}{2}\sum_{\{m\}\sigma} \langle m, m''|V_{ee}|m', m'''\rangle n^{\sigma}_{m,m'}, n^{-\sigma}_{m'',m'''} \\ -(\langle m, m''|V_{ee}|m', m'''\rangle - \langle m, m''|V_{ee}|m''', m'\rangle) n^{\sigma}_{m,m'}, n^{\sigma}_{m'',m'''} \end{aligned} \tag{2.26}$$

where, V_{ee} is the screened Coulomb interaction of electrons in nl quantum states (n is the principal and l is the orbital quantum number). The last term in Eq. (2.25) accounts for the double counting and can be expressed as,

$$E_{dc}[n^{\sigma}] = \frac{UN(N-1)}{2} - \frac{1}{2}J[N^{\uparrow}(N^{\uparrow}-1) + N^{\downarrow}(N^{\downarrow}-1)] \tag{2.27}$$

where, $n^{\sigma} = Tr(n^{\sigma}_{m,m'})$ and $N = N^{\uparrow} + N^{\downarrow}$. U and J represent the screened Coulomb and exchange parameters respectively [20, 21].

Dudarev method

This simplified method to handle rotationally invariant approach of LDA+U was given by Dudarev *et al.* in 1998 [22]. This method considers the orbital degeneracy of $3d$ electrons and neglects exchange interaction along with the non-sphericity of the electronic interaction. The energy functional can be written as,

$$E_U[n_m^\sigma] = \sum_{i,\sigma} \frac{U_i}{2} Tr[n_i^\sigma(1 - n_i^\sigma)] \tag{2.28}$$

where, i is the site index. Thus this expression depends on the trace of occupation matrices. This approach does not use U and J parameters separately rather it considers effective U-J in meaningful way [23].

2.6 Basis sets to expand wavefunctions

Aiming to solve the Kohn-Sham equations and obtain the energy eigenvalues and eigenfunctions, one need to choose an appropriate basis set in which the one electron Kohn-Sham orbitals can be expanded.

Choice of basis sets depends on two factor: (i) the crystal symmetry and (ii) the nature of the elements involved of the periodic table. Depending on the choice of basis sets one electronic structure calculation method differs from the another. Basis set methods are broadly classified into two categories depending on the choice of basis functions as discussed below.

Fixed basis set method

This method uses energy independent basis sets or fixed basis sets as in tight-binding method using linear combination of atomic orbitals (LCAO) [24], orthogonalized plane wave (OPW) method [25] etc. Here to obtain eigenvalue ϵ with expansion coefficient C one has to solve the following

$$(H - \epsilon O)C = 0 \tag{2.29}$$

where O is the overlap matrix.

This method is computationally very simple and faster but its disadvantage is that the basis set may be large to be reasonably complete.

Partial wave basis set method

In this case the wavefunction is expanded into energy and potential dependent all electron partial waves as in cellular method [26], augmented plane-wave

method [27] and Korringa-Kohn-Rostoker (KKR) method [28]. The set of equations with non-linear energy dependence to be solved takes the form as,

$$M(\varepsilon)C = 0 \tag{2.30}$$

This method is advantageous as (i) its basis set is minimal, (ii) it can be applied to any atom of periodic table, (iii) it deals with all electrons and (iv) yields solutions with arbitrary accuracy for closed-pack systems.

The main drawback of these methods is, they are computationally heavy. To get rid of this problem, in 1975 Anderson came up with the proposal to involve linear energy dependency as implemented in Linear Muffin-Tin Orbital (LMTO) and Linear Augmented Plane Wave (LAPW) method [29].

2.7 Basis set methods used in the thesis

In this present thesis, different basis set methods have been used for band structure calculations as listed below,

(i) Plane-wave basis set in projector augmented wave (PAW) potential [27, 28] as implemented in Vienna ab-initio simulation package (VASP) [29–31].

(ii) All electron full potential approach of augmented plane-wave method (APW) with local orbital (LO) [32] as implemented in WIEN2k code [33].

(iii) Tight-binding linear muffin-tin orbital method within atomic sphere approximation (TB-LMTO-ASA) [31] and N^{th} order muffin-tin orbital method (NMTO) as implemented in Stuttgart code [34].

All these methods are described briefly in the following.

2.7.1 Plane-wave basis set method

The plane-wave based DFT calculations are popular due to the following advantages,

- The basis set is independent of atomic positions.
- The Hellman-Feynman forces acting on atoms and the stress of the unit cell can be calculated easily without any basis set correction.
- Change from real-space (diagonal representation of potential V) to momentum-space (diagonal representation of kinetic energy) representation of basis sets is easier through Fast Fourier Transformation (FFT).

The electronic states of a material may be classified into two categories, (a) core states which are localized with deep energy, and (b) valence states which spread out spatially with higher energy. The main problem of using plane-wave basis set is that a large number of plane waves is needed to describe the wavefunctions of the core region accurately because the core electrons are tightly bound to the nucleus and the wavefunctions have high oscillations due to the orthogonality constraints with the electrons in the valence states. This can be overcome by replacing the strong Coulomb potential of the nucleus by an effective ionic potential acting on the valence electrons, called as the pseudopotential. The concept of pseudopotential originates from the basic idea of orthogonalized plane-waves (OPW) proposed by C. Herring [35, 36] where the core states are described by Bloch sums built from localized orbitals and valence states by plane-waves, orthogonalized to the core electron wavefunctions. According to the concept of OPW, orthogonalized plane-wave can be written as,

$$\phi_{\mathbf{k}} = e^{i\mathbf{k}.r} + \sum_{c} b_c \Psi^c_{\mathbf{k}}(r) \tag{2.31}$$

where $\mathbf{k}$ is the Bloch wave vector and subscripts c represents the core states. The constant b_c is determined from the orthogonality condition as follows,

$$\int d\mathbf{r} \Psi^{c*}_{\mathbf{k}}(\mathbf{r}) \phi_{\mathbf{k}}(\mathbf{r}) = 0 \tag{2.32}$$

Taking the linear combination of the OPWs, the wavefunction becomes,

$$\Psi_{\mathbf{k}} = \sum_{\mathbf{k}} c_{\mathbf{k}} \phi_{\mathbf{k}+\mathbf{K}} \tag{2.33}$$

The basic idea of constructing a pseudopotential is: the core regions have very deep and attractive potential where the valence electrons gain kinetic energy due to rapid oscillations and act like a repulsive potential. Smooth nodeless pseudowavefunctions within the core region can mimic the valence wavefunctions being identical to the actual wavefunction outside of the core region [cf. Fig. 2.3]. Developing the pseudopotential idea with the concept of OPW we take $\phi^v_{\mathbf{k}}$ as the plane-wave part of the wavefunction so that,

$$\phi^v_{\mathbf{k}}(\mathbf{r}) = \sum_{\mathbf{k}} C_{\mathbf{k}} e^{i(\mathbf{k}+\mathbf{K}).\mathbf{r}} \tag{2.34}$$

subscript v denotes valence states. Thus,

$$\Psi^v_{\mathbf{k}}(\mathbf{r}) = \phi^v_{\mathbf{k}}(\mathbf{r}) + \sum_{c} \Big(\int d\mathbf{r}' \Psi^{c*}_{\mathbf{k}}(\mathbf{r}') \phi^v_k(r') \Big) \Psi^c_{\mathbf{k}}(\mathbf{r}) \tag{2.35}$$

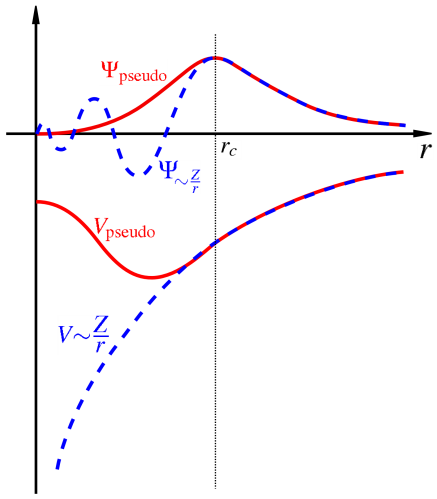

Figure 2.3: Schematic representation of the pseudopotential basic idea. All electron and pseudo potential as well as wavefunctions are represented in blue dashed and red solid lines respectively. r_c is the cut off radius. Picture is adapted from wikipedia.

$\Psi^v_{\mathbf{k}}$ is the exact valence wavefunction satisfies the Schrödinger equation,

$$H\Psi^v_{\mathbf{k}} = \varepsilon^v_{\mathbf{k}}\Psi^v_{\mathbf{k}} \tag{2.36}$$

and similarly for the exact core wavefunction,

$$H\Psi^c_{\mathbf{k}} = \varepsilon^c_{\mathbf{k}}\Psi^c_{\mathbf{k}} \tag{2.37}$$

We can also write the repulsive potential as,

$$V^{\mathbf{R}}\Psi = \sum_c (\varepsilon^v_{\mathbf{k}} - \varepsilon^c_{\mathbf{k}})(\int d\mathbf{r}'\Psi^{c*}_{\mathbf{k}}\Psi)\Psi^c_{\mathbf{k}} \tag{2.38}$$

Thus the Schrödinger equation becomes,

$$(H + V^{\mathbf{R}})\phi^v_{\mathbf{k}} = \varepsilon^v_{\mathbf{k}}\phi^v_{\mathbf{k}} \tag{2.39}$$

The pseudopotential is defined as

$$H + V^{\mathbf{R}} = -\frac{\hbar^2}{2m}V^2 + V_{pseudo} \tag{2.40}$$

Three different kinds of pseudopotentials with plane-wave basis sets, used widely in electronic structure calculations are described below.

(i) Norm conserving pseudopotential: This pseudopotential keeps the basic principle intact imposing only one constraint that the norm of the pseudowavefunctions must be identical to that of the all electron wavefunctions within the cut-off radius (r_c) [37]. For elements with strongly localized electrons, this particular type of pseudopotential requires large number of plane-wave basis sets and makes the computation expensive.

(ii) Ultra soft pseudopotential: The constraint causes the hardness of the norm conserving pseudopotentials which is further removed by implementing a soft pseudopotential introduced by Vanderbilt [38]. This ultra soft pseudopotential reduces the number of plane-waves at the cost of a much more complex formulation of the algorithm. The charge difference between the all electron and pseudo wavefunctions are termed as augmentation charge. The moments and the charge distribution of the all electron wavefunctions are restored accurately within a small cut-off radius for the augmentation charge.

(iii) Projector augmented wave (PAW) method: This method introduced by Blöch [39] is widely used for electronic structure calculation due to its high accuracy, computational lightness compared to other methods. The present thesis extensively uses the PAW based pseudopotential which is described in Section 2.7.4.

2.7.2 Linear augmented plane-wave (LAPW) method

Pseudopotential method has remained very useful for electronic structure calculation but this can not serve for the detailed investigation of the region very close to the nucleus e.g. hyperfine splitting or core level excitations. In these cases augmented plane-wave (APW) method is very useful. In this method the whole space is divided into two regions, (i) region close to the nucleus where the electrons are well localized and can be described efficiently by the atomic like wavefunctions, and (ii) region far from the nucleus where the electrons are delocalized and can be described by plane-waves. Thus around every atom a sphere of radius R_α can be formed, called as the muffin-tin (MT) sphere (S_α) and rest of the region is called the interstitial space (IS). The potential is considered to be spherically symmetric within the MT spheres and constant in the IS, known as muffin-tin approximation. The graphical representation of this potential is given in Fig. 2.4. Thus the APW wavefunction can be described as follows,

$$\phi_G^k(\mathbf{r},\epsilon) = \begin{cases} \dfrac{1}{\sqrt{\Omega}} e^{i(\mathbf{k}+\mathbf{G}).\mathbf{r}} & \text{for } \mathbf{r} \in IS \qquad (2.41a) \\ \displaystyle\sum_{l,m} A_{lm}^{\alpha,\mathbf{k}+\mathbf{G}} \varphi_l^\alpha(\mathbf{r},\epsilon) Y_m^l(\theta',\phi') & \text{for } \mathbf{r} \in S_\alpha \qquad (2.41b) \end{cases}$$

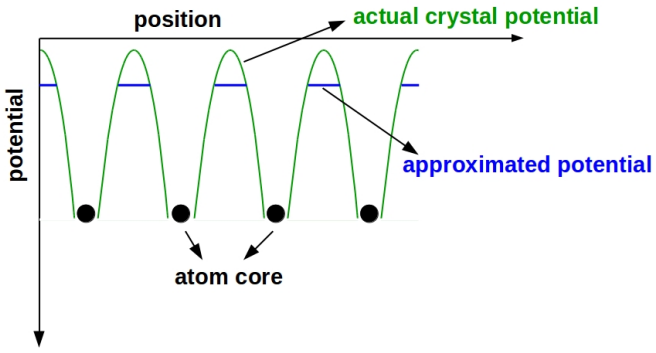

Figure 2.4: Schematic representation of the muffin-tin potential. Potential varies rapidly in the region very close to the atom cores. In the interstitial region the actual potential is approximated to be a constant potential.

φ_l^a represents the solution of the radial Schrödinger equation for an isolated atom a. Coefficient $A_{lm}^{\alpha+\mathbf{k}+\mathbf{G}}$ can be determined by satisfying the criteria that the wavefunctions should be continuous at the boundary of the MT spheres i.e. one needs to match the plane-waves outside the MT spheres to the functions inside the sphere to get the value of the coefficient. As a plane-wave expansion contains infinite term, there will be an infinite number of $A_{lm}^{\alpha+\mathbf{k}+\mathbf{G}}$. So for practical use truncation at some l_{max} value is done. Thus for the crucial parameter, l_{max} a reasonable condition is required for band calculation in LAPW basis as the following,

$$R_i K_{max} = l_{max} \tag{2.42}$$

where, R_i is the radius of i^{th} MT sphere and K_{max} is the cut-off for the plane-waves. The accuracy of the basis is being controlled by the term $R_i^{min} K_{max}$ where, R_i^{min} is the radius of the smallest MT sphere in the unit cell. Solving the secular equation to obtain the energy eigenvalues makes the problem non-linear thus computationally expensive. To cut down the expense linearization of APW method i.e. LAPW was proposed by Anderson [29], Koelling and Arbman [40]. Acoording to Anderson's linearization each basis function is defined as the linear combination of atomic like functions inside the MT sphere, connected smoothly to the plane-wave in the interstitial region. This can be expressed mathematically

as follows,

$$\phi_G^k(\mathbf{r},\epsilon) = \begin{cases} \dfrac{1}{\sqrt{\Omega}} e^{i(\mathbf{k}+\mathbf{G}).\mathbf{r}} & \text{for } \mathbf{r} \in IS \\ \displaystyle\sum_{l,m} [A_{lm}^{\alpha,\mathbf{k}+\mathbf{G}} \varphi_l^{\alpha}(\mathbf{r}',\epsilon_\nu) + B_{lm}^{\alpha,\mathbf{k}+\mathbf{G}} \dot{\varphi}_l^{\alpha}(\mathbf{r}',\epsilon_\nu)] Y_m^l(\theta',\phi') & \text{for } \mathbf{r} \in S_\alpha \end{cases} \tag{2.43a}$$

(2.43b)

Coefficients A_{lm} and B_{lm} are determined by matching the two functions at the sphere boundary in terms of value and slope.

In this method the core states which do not involve in chemical bonding, are treated as in free atoms subject to the potential due to the valence states. The main problem arises to describe the semi-core states lying between the core and valence states. To overcome this problem another basis function called local orbital (LO) is added [41]. This LO basis function consists of a linear combination of two radial functions at two different energies and one energy derivative at one of these energies as follows,

$$\phi_{lm}^{LO} = [A_{lm,R}\varphi_{LR}(r_R,\epsilon_{\nu 1}) + B_{lm,R}\dot{\varphi}_{LR}(r_R,\epsilon_{\nu 1}) + C_{lm,R}\varphi_{LR}(r_R,\epsilon_{\nu 2})] Y_l^m(\mathbf{r}) \tag{2.44}$$

The coefficients can be determined by the requirement that ϕ_{lm}^{LO} should be normalized and have zero value and slope at the MT sphere boundary i.e. it does not leak out of the MT sphere. Though adding LO orbital makes the basis set heavy, they are being used for better accuracy.

2.7.3 Augmented plane wave + local orbital (APW+lo) method

Sjöstedt, Nordström and Singh [42] have shown that LAPW method is not the most effective way to linearize Slaters APW method. Rather linearization of Slaters APW method can be made much efficient by using the standard APW basis, but with $\varphi_l(\mathbf{r},\epsilon)$ at a fixed energy ϵ to keep the eigenvalue problem linear. Addition of local orbital (lo) gives variational flexibility in the radial basis functions

$$\phi_{lm}^{lo} = [A_{lm,R}\varphi_{LR}(r_R,\epsilon_{\nu 1}) + B_{lm,R}\dot{\varphi}_{LR}(r_R,\epsilon_{\nu 1})] Y_m^l(\mathbf{r}) \tag{2.45}$$

The upper case *lo* distinguishes it from *LO* in Eq. (2.44) and the coefficients A_{lm} and B_{lm} do not depend on $\mathbf{k}$ and can be determined by the condition that *lo* is zero at MT sphere boundary and normalized [33]. This new scheme converges to the identical result as LAPW produces but it reduces the RK_{max} which significantly

reduces the basis set size thus becomes computationally light.

In this thesis we have used APW+lo based computer code as implemented in WIEN2k [33].

2.7.4 Projector augmented wave (PAW) method

In 1994 projector augmented wave (PAW) method was introduced by Blöchl [39] aiming to achieve the computational efficiency of the pseudopotential method and the accuracy of the full-potential LAPW method simultaneously.

Within this formalism a linear transformation τ is applied to map the smooth pseudopotential (PS) wavefunction Ψ_n^{PS} to all electron (AE) true wavefunction Ψ_n^{AE} following the relation,

$$\Psi_n^{AE} = \tau \Psi_n^{PS} \tag{2.46}$$

A transformation v has the contribution from atom-centred part (τ_R) apart from identity and it takes the form as,

$$\tau = 1 + \sum_R \tau_R \tag{2.47}$$

Now an augmentation region Ω_R is defined surrounding each atom in which the local contribution τ_R can act. This augmentation region is equivalent to muffin-tin sphere as defined in the linear methods and core region in pseudopotential method.

Thus out side of this Ω_R region, the AE and PS wavefunctions are the same. The AE wave function being transformed from the PS wavefunction can be written as follows,

$$|\Psi_n^{AE}\rangle = |\Psi_n^{PS}\rangle + \sum_i (|\phi_i^{AE}\rangle - |\phi_i^{PS}\rangle)\langle p_i^{PS}|\Psi_n^{PS}\rangle \tag{2.48}$$

where, ϕ_i^{AE} and ϕ_i^{PS} represent the all-electron and pseudopotential partial waves respectively. p_i^{PS} is the projector function satisfying $\langle p_i^{PS}|\phi_j^{PS}\rangle = \delta_{ij}$ relation within Ω_R region for each PS partial waves.

Using the transformation for any operator A in the AE space, one can evaluate it for the PS space as,

$$A_{PS} = \tau^* A_{AE} \tau \tag{2.49}$$

Likewise the Kohn-Sham equation can be transformed and written as follows,

$$(H_{PS} - \varepsilon S)|\Psi_i^{PS}\rangle = 0 \tag{2.50}$$

where, $H_{PS} = \tau^* H \tau$ and $S = \tau^* \tau$ is the pseudopotential overlap operator.

We have used the PAW method and a plane-wave basis set as implemented in VASP [43, 44] code in this thesis.

2.7.5 Linearized muffin-tin orbital (LMTO) method

Linearized muffin-tin orbital (LMTO) [31] method of calculation uses the energy independent basis set strategy. This approach is very efficient at the same time computationally light for electronic structure calculation. This is strikingly good choice for obtaining chemical insight of complex electronic structure.

Here the actual crystal potential is replaced by the muffin-tin potentials as shown in Fig. 2.4 schematically. This approximation assumes the potential to be spherically symmetric ($v(\mathbf{r}_R)$) close to the nuclei i.e. within the muffin-tin sphere of radius S_R and constant in the interstitial region.

The radial part of Schrödinger equation inside and outside (interstitial region) of the MT sphere takes the form as follows respectively.

$$[\frac{d^2}{dr_R^2} + \frac{l(l+1)}{r_R^2} - v(r_R) - \varepsilon]r_R\varphi(r_R) = 0 \tag{2.51}$$

$$[\frac{d^2}{dr_R^2} + \frac{l(l+1)}{r_R^2} - \kappa^2]r_R\varphi(r_R) = 0 \tag{2.52}$$

where, $\kappa^2 = \varepsilon - v_0$. The solution of Eq. (2.51) is partial wave which is the product of the radial part and spherical harmonics and can be written as,

$$\phi(r_R) = \varphi(r_R, \varepsilon)Y_L(r_R) \tag{2.53}$$

where, L represents the angular momentum (l, m) and Y_L is the spherical harmonics.

Outside the MT sphere the solution of Eq. (2.52) is the plane-wave solution and can be expanded in Neumann $\eta_l(\kappa r_R)$ and Bessel $j_l(\kappa r_R)$ functions. The solutions inside and outside the MT sphere must match continuously and smoothly at the MT sphere boundary to satisfy the well behaved wavefunction characteristics which lead to energy dependent KKR equation. This approach is accurate but the energy dependency makes it computationally heavy. Later to avoid the energy dependence the MT spheres are replaced by space filling atomic spheres, called Wigner-Seitz (WS) spheres as proposed by Anderson in his linearization of atomic sphere approximation [29]. Following Anderson's proposal the LMTO basis function can be written as,

$$\chi^{\alpha}_{RL} = \phi_{RL}(r_R) + \sum_{R'L'} \dot{\phi}^{\alpha}_{R'L'}(r_{R'})h^{\alpha}_{R'L',RL} \tag{2.54}$$

where ϕ's are the partial waves residing within the WS sphere centered at R. $\dot{}$ represents derivative with respect to energy and the function $\dot{\phi}^{\alpha}_{R'L'}(r_{R'})$ can be written as a linear combination of ϕ and $\dot{\phi}$,

$$\dot{\phi}^{\alpha}_{R'L'} = \dot{\phi}_{R'L'} + \phi_{R'L'}O^{\alpha} \tag{2.55}$$

where O^{α} is non-diagonal overlap matrix. The h^{α} matrix is given by,

$$h = C^{\alpha} - \epsilon_{\nu} + (\Delta^{\alpha})^{1/2} S^{\alpha} (\Delta^{\alpha})^{1/2} \tag{2.56}$$

where, C^{α} and Δ^{α} denote the diagonal potential matrices known as band centre and band width respectively. These matrices depend on the potential inside the MT sphere, screening parameter α and on the sphere radii. S is the structure matrix which depends on the representation and the geometrical arrangement of the atomic sites.

2.7.6 Improved LMTO: N^{th} order muffin-tin orbital (NMTO) downfolding method

To obtain single particle part of a many body model Hamiltonian namely, the hopping integrals, onsite energy terms out of full DFT Hamiltonian, one needs to construct a low-energy few band Hamiltonian in energy selective manner which is achieved by downfolding method. This technique divides the whole space into two parts: lower $|l\rangle$ and upper $|h\rangle$. The reduction of the full Hamiltonian H into lower subset Hamiltonian $\tilde{H_{ll}}$ is done in such a way that lower l eigenvalues of the original Hamiltonian H and eigenvalues of $\tilde{H_{ll}}$ are the same. $\tilde{H_{ll}}$ Hamiltonian can be expressed as follows,

$$\tilde{H_{ll}} = H_{ll} - H_{lh}(H_{hh} - \epsilon)^{-1} H_{hl} \tag{2.57}$$

introducing additional energy dependence which further gets removed through linearization of LMTO method taking care of ghost band problem but fails to provide an accurate way for a massive downfolding where the downfolded bands span in a very narrow energy window. The disadvantages faced with LMTO are as follows,

- the basis set is complete to 1^{st} order $(\epsilon - \epsilon_{\nu})$ inside the sphere and complete to only 0^{th} order $(\epsilon - \epsilon_{\nu})^0 = 1$ in the interstitial which leads to inconsistency. This problem was further overcome by introducing atomic sphere approximation (ASA) and removing the interstitial region. In this approximation the MT spheres are replaced by space filling atomic spheres, called Wigner-Seitz (WS) spheres. Although this approach makes the formalism heavy.

- the Hamiltonian H is expanded in the orthogonal representation as a power series in two centred tight-binding (TB) Hamiltonian h obtained within atomic sphere approximation (ASA) excluding downfolding as,

$$\langle \phi | H - \epsilon_{\nu} | \phi \rangle = h - hoh + ... \tag{2.58}$$

All these drawbacks are taken care through a recent formalism of a more sophisticated method, based on N^{th} order NMTO [34] basis which provides the downfolded band structure within a chosen energy window accurately. Here the energy dependent partial wave $\phi_{RL}(\epsilon, r_R)$ is retained as a solution within atomic sphere where the potential is approximated to be spherical, but in the interstitial region, a screened spherical wave (SSW) is used instead of the Neumann function. The screened technique introduces a hard sphere of radius a and a phase shifted

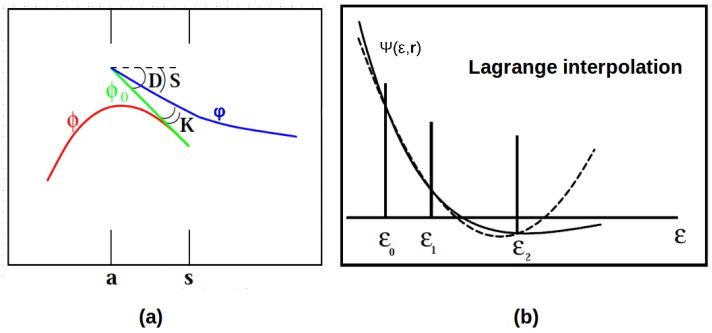

Figure 2.5: (a) Kink partial wave construction with ϕ, ϕ_0 and φ. (b) Quadratic N^{th} order approximation to energy dependence of a partial wave for discrete energy mesh (Lagrange). Figures are taken from Ref. [45].

partial wave solution ϕ_0 matches the value and slope of ϕ at S_R but their curvatures differ. ϕ_0 is joined continuously with a kink to the SSW φ at the hard sphere as shown in Fig. 2.5 (a). This form of combined contribution is known as the Kink Partial Wave (KPW). The NMTO basis sets are constructed by Lagrange interpolation of the partial waves ψ^{α}_{RL} at $(N+1)$ energy points $\varepsilon_0, \varepsilon_1, ..., \varepsilon_N$ [cf. Fig. 2.5 (b)].

This basis set is constructed with the aim of energy selection within a very narrow energy window integrating out all the irrelevant orbital from full DFT Hamiltonian thus it is well localized in nature and serves as Wannier orbitals. The real-space representation of the downfolded Hamiltonian keeping only the relevant orbitals, gives the hopping parameters, onsite energies of these orbitals, as used in the present thesis.

2.8 Genetic algorithm: A theoretical crystal structure predictor

The structural information is the essential information needed to understand the physical properties of a material. The conventional way to search for the stable crystal structure knowing the chemical composition of a material is experimental synthesis which is time consuming as well as expensive. Thus theoretical

prediction of the crystal structure knowing only chemical composition is always a better alternative to avoid the expense. This method is very much successful in designing new materials with targeted properties.

The theoretical search of crystal structure of a material is challenging as it is entangled with the search of multidimensional energy landscape and the ranking of the relative energies correctly [46]. The computational task to search for the stable crystal structure requires a global optimization operator which will pick the lowest energy structure at given external conditions like pressure and temperature. There are various genetic algorithms available to predict the crystal structure e.g. constant pressure molecular dynamics implemented Parrinello-Rahman algorithm [47], simulated annealing [48–51], minima hopping [52], metadynamics [53–55], Swarm algorithms [56–58], Monte Carlo basin hopping [59], random sampling [60] etc. All these methods, offering limited success, necessitate the development of a very different evolutionary algorithm [46]. This evolutionary algorithm has been a very successful tool in predicting and designing the crystal structure of minerals and materials even before lab synthesis.

In this thesis we have applied Universal Structure Predictor: Evolutionary Xtallography (USPEX) [61, 62], the evolutionary algorithm for crystal structure prediction of a material.

In the following a brief description of this evolutionary algorithm and how it works is given.

2.8.1 Universal Structure Predictor: Evolutionary Xtallography (USPEX): The evolutionary algorithm for crystal structure prediction

Evolutionary algorithm is an attractive scheme as it finds out the global minima in fully nonlocal way without involving any assumptions on the order parameter and any initial structure as a prior.

USPEX evolutionary algorithm uses the energy obtained from *ab-inito* or other classical calculations of local optimization of structure, as the fitness parameter to find out the global minima i.e. the stable structure in an evolutionary way. Though the computation is expensive, USPEX provides accurate results predicting not only the most stable structure but also a set of low-energy metastable phases. This algorithm is able to compare the energies of competing phases in a wide energy landscape without trapping into any local minima. The most challenging part of any evolutionary algorithm is to find new samples for each generation. The relative position of the nearby atoms holds the main information about any structure. The spatially selected fraction of such a structure holds lots of information of the entire structure and rearranging these fragments can be served as 'parent' for new 'off-spring' generation and thus helps to search for stable crystal structure in promising way. Thus USPEX uses the basic prescrip-

tion of evolutionary approach, to initiate from a population (set of structures) and evolve them using three variational operators namely heredity, mutation and permutation which will be discussed later on.

The basic flowchart of evolutionary algorithm is shown in Fig. 2.6. The first

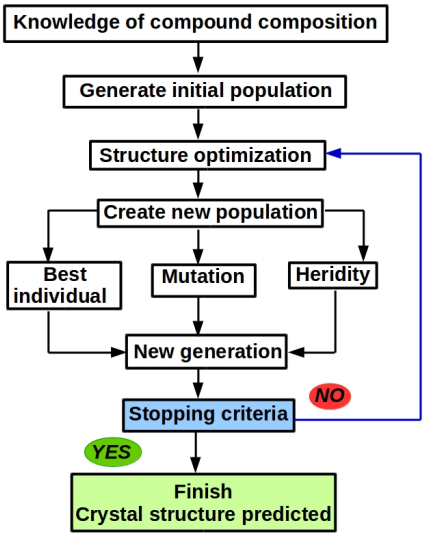

Figure 2.6: Flowchart of evolutionary algorithm for crystal structure prediction.

generation generates structures randomly for a chemical composition of interest. Then they go through hard constraints where inter-atomic distances, restriction of the cell angles (α, β, γ) between 60° and 120°, minimal lattice vector length (not larger than largest atom diameter) are checked for all the structures to remove the redundancies in the search space. The hard constraints fulfil two purposes, (i) the minimal inter-atomic distances must be sufficient to ensure that there is no overlap of the pseudopotential core regions and (ii) they zoom in the search reducing the search space and allow to have system specific knowledge. Any individual disobeying any one of the hard constraints are discarded from the search. All the generated individuals are then optimized by some external code interfaced with this algorithm. In this thesis we used plane-wave method as implemented in Vienna Ab-initio Simulation Package [44] code to calculate the energy which is the fitness parameter and the structures are ranked according to their fitness parameter. The weak structures are discarded and rest of the structures are selected as parent for the next generation of structures. In this succeeding generations new structures are generated employing the variational operators as discussed below.

- **Heredity:** This operator produces a new off-spring structure taking and combining a fraction which are spatially coherent slabs of each of the two

individual parent structures. These fractions must bear the informations of the parents as much as possible.
In detail, a lattice vector is picked randomly along which the atoms will be shifted and a random number (x) between 0 and 1 is generated for the two individual parents. For the first individual of the parents, the fraction value should be between 0 and x and that for the second individual will be between x and 1. Now these two fractions are mixed together to form a new individual i.e. the off-spring. The total atom number of the new individual is counted and compared with the desired value and atoms are added or removed in a certain way to keep the desired number of atoms intact. Here the off-spring has weighted averaged lattice parameters of the two parent individuals.

- **Mutation:** Here a single parent individual produces a off-spring by applying a strain matrix which transforms parent lattice vector $\vec{a}$ to off-spring lattice vector $\vec{a'}$ in the following way,

$$\vec{a'} = [I + \epsilon_{ij}]\vec{a} \tag{2.59}$$

  where, I represents the unit matrix and ϵ_{ij} is the symmetric strain matrix. The distortion caused by strain matrix facilitates to set up step size of the lattice parameter.

- **Permutation:** Here one parent individual generates a off-spring by exchanging two atoms of different kind, a variable number of times. This method can be operational only when the parent consists of more than one type of atoms. Permutation helps to find out correct atomic ordering.

After the actions of the operators, the off-spring structures together with few best structures of the previous generation, create the population for the next generation and this procedure goes on until any lower energy stucture gets produced for a sufficient number of generations. To cut down the computational expense seeding procedure is applied where initial structures are provided for the first generation if good structures are available. Although seeding incorporates bias which can misdirect the search but careful handling can converge the search for the stable crystal structure in short time.

2.9 Exact diagonalization of model Hamiltonian

Exact diagonalization (ED) technique is used to calculate electronic properties numerically by constructing a finite sized cluster instead of the full lattice. An ED technique differs from any first principle technique in the sense that nothing is approximated in solution of the problem but needs to be carried out on

a Hamiltonian that retains only few degrees of freedom. To obtain the energy eigenvalues and eigenvectors though ED one needs to construct a model Hamiltonian of finite lattice size. Next step to write the Hamiltonian, is to choose basis set which is preferably the localized Wannier functions.

In this thesis we have employed exact diagonalization technique on a model Hamiltonian which contains crystal field part (H_Δ) depending on the lattice symmetry, interaction term (H_t), known as the Kanamori Hamiltonian, spin-orbit coupling term (H_{SOC}) and hopping term (H_t) as follows,

$$H = H_\Delta + H_t + H_{SOC} + H_t \tag{2.60}$$

The explicit expression of each of the terms are given below,

$$\begin{aligned}
H_\Delta &= \sum_i \sum_{l,m} \Delta^i_{l,m} d^\dagger_{i,l\sigma} d_{i,m\sigma} \\
H_{int} &= U \sum_i \sum_l n_{i,l\uparrow} n_{i,l\downarrow} + \frac{(U' - J_H)}{2} \sum_i \sum_{\substack{l,m \\ l\neq m}} n_{i,l\sigma} n_{i,m\sigma} + \frac{U'}{2} \sum_i \sum_{\substack{l,m \\ l\neq m \\ \sigma\neq\sigma'}} n_{i,l\sigma} n_{i,m\sigma'} \\
&\quad - \frac{J_H}{2} \sum_i \sum_{\substack{l,m \\ l\neq m}} (d^\dagger_{i,m\uparrow} d_{i,m\downarrow} d^\dagger_{i,l\downarrow} d_{i,l\uparrow} + d^\dagger_{i,m\uparrow} d^\dagger_{i,m\downarrow} d_{i,l\uparrow} d_{i,l\downarrow} + H.c.) \\
H_{SOC} &= \frac{i\lambda}{2} \sum_i \sum_{\substack{l,m,n \\ \sigma,\sigma'}} \epsilon_{lmn} d^\dagger_{i,l\sigma} d_{i,m\sigma'} \sigma^n_{\sigma,\sigma'} \\
H_t &= \sum_{\substack{l,m,\sigma \\ \langle i,j\rangle}} t^{ij}_{lm} (d^\dagger_{i,l\sigma} d_{j,m\sigma} + H.c.)
\end{aligned} \tag{2.61}$$

$d^\dagger_{i,l\sigma}$, $d_{i,l\sigma}$ are the creation and annihilation operator of the l^{th} orbital at site i with spin σ. H_Δ represents the onsite crystal field splitting with onsite matrix element $\Delta_{l,m}$ between l and m orbital at the same site i. H_{int} contains intra-orbital Coulomb correlation (U), Hund's coupling (J_H) and inter-orbital Coulomb correlation (U'). Coulomb interaction satisfies $U' = U - 2J_H$. In H_{SOC}, λ is the spin-orbit coupling strength and ϵ_{lmn} is the three dimensional leve-civita symbol. H_t contains t^{ij}_{lm} hopping parameter between l^{th} and m^{th} orbital of i and j sites respectively. Low-energy few band Hamiltonian and the system specific hopping parameters are obtained by employing N^{th} order downfolding technique. This model Hamiltonian containing multiple orbital and spin-orbit coupling is solved by exact diagonalization for accurate understanding of the parameter space.

The solution by exact diagonalization technique is shown considering 1-band

Hubbard model as an example, involving the physics of electrons, spins and phonons [63]. The Hamiltonian takes form as follows,

$$H = -t \sum_{\langle ij \rangle, \sigma} (c^{\dagger}_{i\sigma} c_{j\sigma} + H.c.) + U \sum_{i} n_{i\uparrow} n_{i\downarrow} \tag{2.62}$$

where $c^{\dagger}_{i\sigma}$ and $c_{i\sigma}$ are the creation and annihilation operators of an electron with spin σ at site i respectively and 'H.c.' denotes its hermitian conjugate counterpart, t is hopping term and U represents the repulsive onsite Coulomb interaction. To diagonalize the Hamiltonian matrix it is important to know the dimension of the matrix. For a Hubbard model each site can have four spin states. Thus for the Hubbard model with a system of N number of lattice sites, the basis set size is 4^N [64]. Due to the exponential growth of basis set size ED prefers small clusters to be computationally light. The advantages of common symmetries are applied to cut down the computer expense. These symmetries incorporate the conservation of total charge, total spin along z direction. The basis set size thus reduces to ${}^{N}C_{N\uparrow} \times {}^{N}C_{N\downarrow}$ where, $N\uparrow$ and $N\downarrow$ represents the total number of atoms with spin up and down respectively. Translational and rotational symmetries can reduce the basis set size thus the dimension of the Hamiltonian matrix further. Most of the time the matrix is sparse though it consumes computer memory which can be solved by block diagonalization of the matrix by producing smaller matrices along the diagonal.

In the thesis we have applied Lanczos algorithm for exact diagonalization. This is one of the simplest algorithms to extract ground state properties from a sparse matrix through ED. In this method from a random initial state $|\phi_0\rangle$, a set of states $H^n|\phi_0\rangle$ is constructed by applying the Hamiltonian matrix H. These states forming the Krylov space will be orthogonalized against each other to obtain the basis set of the space. Applying the orthonormality we can write

$$\langle \phi_0 | \phi_0 \rangle = 1 \tag{2.63}$$

A new state $|\phi_1\rangle$ is defined as,

$$H|\phi_0\rangle = a_0|\phi_0\rangle + b_1|\phi_1\rangle \tag{2.64}$$

Again from the conditions we can write,

$$\langle \phi_0 | \phi_1 \rangle = 0 \quad \text{and} \quad \langle \phi_1 | \phi_1 \rangle = 1 \tag{2.65}$$

Thus the coefficients a_0, b_1 and state $|\phi_1\rangle$ of Eq. (2.64) should be determined. The following steps should be applied.

$$a_0 = \langle \phi_0 | H | \phi_0 \rangle \tag{2.66}$$

So from Eq. (2.64) we can write

$$b_1|\phi_1\rangle = (H - a_0)|\phi_0\rangle \tag{2.67}$$

Now applying the orthonormality and multiplying Eq. (2.67) with $\langle\phi_1|$ we get,

$$b_1^2 = [(H - a_0)|\phi_0]^\dagger[(H - a_0)|\phi_0] \tag{2.68}$$

Because of the definite positive inner product, $b_1^2 \geq 0$. For $b_1^2 > 0$, $|\phi_1\rangle$ becomes,

$$|\phi_1\rangle = (H - a_0)|\phi_0\rangle/b_1 \tag{2.69}$$

Next a set of orthonormal states $\{|\phi_0\rangle, |\phi_1\rangle, ..., |\phi_n\rangle\}$ with $\{a_0, a_1, ..., a_{n-1}\}$ and $\{b_1, b_2, ..., b_n\}$ real parameters, is constructed using Lanczos step keeping the constraint that no b will be 0. Using recursion relation the following equations can be written to determine the parameters.

$$H|\phi_n\rangle = a_n|\phi_n\rangle + b_{n+1}|\phi_{n+1} + b_n|\phi_{n-1}\rangle \tag{2.70}$$

$$a_n = \langle\phi_n|H|\phi_n\rangle \quad \text{and} \quad b_n = \langle\phi_n|H|\phi_{n-1}\rangle \tag{2.71}$$

For new state $|\phi_{n+1}\rangle$,

$$b_{n+1}|\phi_{n+1}\rangle = (H - a_n)|\phi_n\rangle - b_n|\phi_{n-1}\rangle \tag{2.72}$$

and again in similar way for $b_{n+1} > 0$ we can write,

$$|\phi_{n+1}\rangle = [(H - a_n)|\phi_n\rangle - b_n|\phi_{n-1}\rangle]/b_{n+1} \tag{2.73}$$

All these states constructed are normalized to 1 and orthogonal to each other. Thus starting with any random normalized state $|\phi_0\rangle$ and imposing constraints as initial conditions, $b_0 = 0$ and $|\phi_{-1}\rangle = 0$, the tridiagonal Hamiltonian takes the form as follows [63, 65],

$$H = \begin{bmatrix} a_0 & b_1 & 0 & 0 & \cdots \\ b_1 & a_1 & b_2 & 0 & \cdots \\ 0 & b_2 & a_2 & b_3 & \cdots \\ 0 & 0 & b_3 & a_3 & a_{n-1} \\ \vdots & \vdots & \vdots & \vdots & b_{n-1} \end{bmatrix} \tag{2.74}$$

Now the eigenvalues of this Hamiltonian matrix can be obtained through standard library functions [66]. With the obtained eigenvalues the search for the eigenvectors can be done easily.

This method of calculation for obtaining the eigenvalues and eigenvectors is advantageous as the extreme eigenvalues of the matrix H converge rapidly to the extreme values of H for a finite N.

2.10 Monte Carlo technique: A finite temperature calculation

In this thesis we have employed Monte Carlo method on the model Hamiltonian describing the system besides DFT calculations.

The method of Monte Carlo is based on repeated random sampling to obtain numerical results. This algorithm uses random walk in the phase space for the transition from one state (m) to another state (n). The energy difference of phase transition is defined as $\Delta_{nm} = E_n - E_m$, where E_n and E_m are the energies of phase n and m respectively. The transition probability from m to n becomes 1 if the move is downhill in energy i.e. $\Delta_{nm} < 0$. If the move is uphill in energy i.e. $\Delta_{nm} > 0$ then the move is accepted with the ratio of probabilities of initial and final states. Thus it follows the acceptance and rejection decision generating the random numbers through random walk.

For an Ising spin system with two spin states S_1 and S_2 and obeying Boltzmann distribution we can write the acceptance probability as follows,

$$A(S_1 \rightarrow S_2)) = \begin{cases} e^{-\Delta E/T} & \text{for } \Delta E = E_{S_1} \text{ - } E_{S_2} > 0, \text{ uphill} \quad (2.75a) \\ 1 & \text{for } \Delta E \leq 0, \text{ downhill} \quad (2.75b) \end{cases}$$

Spin flip is accepted for downhill condition, though if the energy is increased (uphill) spin flip is accepted with a certain probability [67]. In this case a random number r is generated between [0,1] and move is accepted for $r < e^{-\Delta E/T}$.

Thus for practical use and to determine different physical properties at finite temperature of a spin system, a finite cubic lattice size $L \times L \times L$ should be defined with all the periodic boundary conditions. Next a spin configuration with all either up or down spin is considered to start the process and following iterative steps take place as follows until self consistency is achieved [68].

- At first any site i is selected with spin S_i for spin flipping $S_i \rightarrow -S_i$.
- The change in energy ΔE for spin flipping is calculated.
- Transition probability i.e. the acceptance probability for spin flip is calculated estimating the energy change associated with spin flip
- Decision of spin flipping is made by generating a random number between 0 and 1. For the allowed transition the corresponding spin configuration serves as the new configuration.
- The ground state configuration is stored to extract its different properties. For an example to calculate total magnetization M_{total}, M_{total} should be updated with $M_{total} + 2S_i$.

Bibliography

[1] M. Born and J. R. Oppenheimer, Annu. Physik **84**, 457 (1927).

[2] D. R. Hartree, Proc. Cambridge Phil. Soc. **24**, 111 (1928).

[3] C. C. J. Roothaan, Rev. Mod. Phys. **23**, 69 (1951).

[4] C. D. Sherrill, An Introduction to Configuration Interaction Theory, Georgia Institute of Technology (1995).

[5] P. Hohenberg and W. Kohn, Phys. Rev. B **136**, 864 (1964).

[6] W. Kohn and L. J. Sham, Phys. Rev. A **140**, 1133 (1965).

[7] W. Kohn, Nobel Lecture, Rev. Mod. Phys. **71**, 1253 (1999).

[8] L. H. Thomas, Proc. Cambridge Phil. Soc. **23**, 542548 (1927).

[9] E. Fermi, 'Un Metodo Statistico per la Determinazione di alcune Priopriet dell'Atomo', Rend. Accad. Naz. Lincei **6**, 602607 (1927).

[10] P. A. M. Dirac, 'The Quantum Theory of the Electron', Proceedings of the Royal Society A : Mathematical, Physical and Engineering Sciences **117**(778), 610 (1928).

[11] J. Kohanoff, Electronic Structure Calculations For Solids And Molecules: Theory and Computational Methods, Cambridge University Press, (2006).

[12] D. M. Ceperley and B.J. Alder, Phys. Rev. Lett. **45**, 566 (1980).

[13] J. P. Perdew and A. Zunger, Phys. Rev. B **23**, 5048 (1981).

[14] J. P. Perdew and Y. Wang, Phys. Rev. B **45**, 13244 (1992).

[15] R. O. Jones and O. Gunnarson, Rev. Mod. Phys. **61**, 689 (1989).

[16] J. P. Perdew, in Electronic Structure of Solids 91, edited by P. Ziesche and H. Eschrig (Akademie Verlag, Berlin), 11 (1991).

[17] J. P. Perdew, K. Burke and M. Ernzerhof, Phys. Rev. Lett. **77**, 3865 (1996).

[18] V. I. Anisimov, J. Zaanen, and O. K. Andersen, Phys. Rev. B **44**, 943 (1991).

[19] A. I. Liechtenstein, V. I. Anisimov, and J. Zaanen, Phys. Rev. B **52**, R5467 (1995).

[20] O. Gunnarsson, O. K. Andersen, O. Jepsen and J. Zaanen, Phys. Rev. B **39**, 1708 (1989).

[21] V. I. Anisimov, and O. Gunnarsson, Phys. Rev. B **43**, 7570 (1991).

[22] S. L. Dudarev, G. A. Botton, S. Y. Savrasov, C. J. Humphreys and A. P. Sutton, Phys. Rev. B **57**, 1505 (1998).

[23] M. Cococcioni and S. de Gironcoli, Phys. Rev. B **71**, 035105 (2005).

[24] J. C. Slater and G. F. Koster, Phys. Rev. **94**, 1498 (1954).

[25] J. C. Phillips and L. Kleinman, Phys. Rev. 116, 287 (1959).

[26] E. P. Wigner and F. Seitz, Phys. Rev. **46**, 509 (1934).

[27] T. L. Loucks, Augmented Plane wave Methods, Benjamin, New York, (1967).

[28] J. Korring, Physica **13**, 392 (1947); J. Korringa, Phys. Rev. **238**, 341 (1994).

[29] O. K. Andersen, Phys. Rev. B **12**, 3060 (1975).

[30] W. Kohn and N. Rostoker, Phys. Rev. **94**, 1111 (1954).

[31] O. K. Andersen and O. Jepsen, Phys. Rev. Lett. **53**, 2571 (1984).

[32] O. Jepsen, J. Madsen, and O. K. Andersen, Phys. Rev. B **18**, 605 (1978).

[33] P. Blaha, K. Schwarz, G. K. H. Masden, D. Kvasnicka, and J. Luitz, in Wien2k, An Augmented PlaneWave+Local Orbitals Program for Calculating Crystal Properties, edited by K. Schwarz, Technische Universitiat Wien, Vienna, (2001).

[34] O. K. Andersen and T. Saha-Dasgupta, Phys. Rev. B **62**, R16219 (2000).

[35] C. Herring, Phys. Rev. **57**, 1169 (1940).

[36] C. Herring and A. G. Hill, Phys. Rev. **58**, 132 (1940).

[37] D. R. Hamann, M. Schlter, and C. Chiang, Phys. Rev. Lett. **43**, 1494 (1979).

[38] D. Vanderbilt, Phys. Rev. B **41**, 7892 (1985).

[39] P. E. Blöchl, Phys. Rev. B **50**, 17953 (1994).

[40] D. D. Koelling and G. O. Arbman, J. Phys. F. Met. Phys. **5**, 2041 (1975).

[41] D. Singh, Phys. Rev. B **43**, 6388 (1991).

[42] E. Sjöstedt, L. Nordström, and D. J. Singh, Solid State Commun. **10**, 137 (2000).

[43] G. Kresse and J. Hafner, Phys. Rev. B **47**, 558 (1993).

[44] G. Kresse and J. Furthmuller, Phys. Rev. B **54**, 11169 (1996).

[45] T. Saha-Dasgupta, http://www.jncasr.ac.in/cams06/talks/18th_tanusri_mot.pdf.

[46] A. R. Oganov, A. O. Lyakhov, and M. Valle, Acc. Chem. Res. **44**, 227 (2011).

[47] M. Parrinello and A. Rahman, Phys. Rev. Lett. **45**, 1196 (1980); J. Appl. Phys. **52**, 7182 (1981).

[48] M. W. Deem and J. M. Newsam, Nature **342**, 260 (1989).

[49] J. Pannetier, J. Bassas-Alsina, J. Rodriguez-Carvajal and V. Caignaert, Nature **346**, 343 (1990).

[50] M. B. Boisen, G. V. Gibbs, and M. S. T. Bukowinski, Phys. Chem. Miner. **21**, 269 (1994).

[51] J. C. Schön and M. Jansen, Angew. Chem. Int. Edn **35**, 1287 (1996).

[52] S. Gödecker, J. Chem. Phys. **120**, 9911 (2004).

[53] R. Martonak, A. Laio and M. Parrinello, Phys. Rev. Lett. **90**, 075503 (2003).

[54] R. Martonak, A. Laio, M. Bernasconi, C. Ceriani, P. Raiteri, F. Zipoli, M. Parrinello, Z. Kristallogr. **220**, 489 (2005).

[55] R. Martoňák, D. Donadio, A. R. Oganov and M. Parrinello, Nat. Mater. **5**, 623 (2006).

[56] R. C. Eberhart and Y. Shi, IEEE Trans. Evolut. Comput. **8**, 201 (2004).

[57] R. Poli, D. Bratton, T. Blackwell and J. Kennedy, IEEE Trans. Evolut. Comput. 1955 (2007).

[58] Y. Wang, J. Lv, L. Zhu and Y. Ma, Phys. Rev. B: Condens. Matter **82**, 1 (2010).

[59] D. Wales and J. P. K. Doye, J. Phys. Chem. A **101**, 5111 (1997).

[60] C. J. Pickard and R. J. Needs, Nat. Mater. **7**, 775 (2008).

[61] A. R. Oganov, C. W. J. Glass, Chem. Phys. **124**, 244704 (2006).

[62] A. O. Lyakhov, A. R. Oganov, M. Valle, In Modern Methods of Crystal Structure Prediction; Oganov, A.R., Eds.; Wiley-VCH Verlag GmbH and KGaA: Weinheim, Germany (2012).

[63] A. Weiße and H. Fehske, Lect. Notes Phys. **739**, 529 (2008).

[64] H. Q. Lin and J. E. Gubernatis, Computers In Physics **7**, 400 (1993).

[65] A. Nandgaonkar, Static and Dynamical Properties of Correlated Systems. Ph.D thesis, Department of Physics, University of Pune (2004).

[66] Linear Algebra PACKage. URL http://www.netlib.org.

[67] K. H. Hoffmann, M. Schreiber (Eds.), Computational Physics, Springer-Verlag Berlin Heidelberg (1996).

[68] K. Binder, and D. W. Heermann, Monte Carlo Simulation in Statistical Physics (1988).

Chapter 3

Examining the microscopic chemical structure and mixed anion chemistry through fluorination for oxygen deficient compounds of $CaMnO_{3-x}$ $(x = 1, 0.5)$*

Motivation

Perovskites with general chemical formula ABO_3 are the class of materials, extensively studied for showing enormous variety in physical properties. In recent years oxygen deficient compounds of perovskites with formula $A_nB_nO_{3n-x}$ (n = integer number of perovskite blocks in unit cell, x = integer) are evolved through oxygen engineering [1] resulting into the transition metal (TM) of the perovskite structure with varying oxidation states. The BO_6 octahedra of the perovskite structure changes to BO_5 or BO_4 polyhedra depending upon the oxygen vacancy pattern. The anionic sublattice under reduction atmosphere generates new metastable phases dealing with the tunable oxidation states of transition

*Based on publications: Payel Aich, **Shreya Das**, Carlo Meneghini, Irene Schiesaro, Tanusri Saha-Dasgupta, Sugata Ray; **Physica B: Condens. Matter 581, 411837 (2020)**; Payel Aich†, **Shreya Das**†, Carlo Meneghini, Desheng Fu, Vasudeva Siruguri, S. D. Kaushik, Mitsuru Itoh, Tanusri Saha-Dasgupta, and Sugata Ray; †authors have equal contribution to this work; **manuscript submitted**.

metals. These types of reactions are highly topotactic because the reactivity and nature of final reduction products are determined by the crystal structure of the parent compound [1]. These new superstructures incorporating oxygen vacancies at different degrees, show interesting novel properties.

Besides oxygen vacancy, incorporation of a foreign anion in the system through mixed anion chemistry makes the situation more interesting by changing the structural and physical properties. Incorporation of a second anion and manipulating the anionic sublattice becomes easier for oxygen deficient compounds of perovskites as they already consist of various vacancy patterns.

Mn based perovskite oxides e.g $LaMnO_3$, $LiMn_2O_4$, $CaMnO_3$ [2,3] have been studied in the field of electrochemical energy storage. The interest in search of electrocatalysts with better performance, interesting magnetic properties, non-centrosymmetricity, paves the path to play with the anionic sublattice of Mn based perovskites.

$CaMnO_3$ is a promising perovskite oxide to incorporate varying degree of oxygen vacancy as the Mn valency can be varied from Mn^{4+} to Mn^{2+}. Topotactic oxygen removal from $CaMnO_3$ produces oxygen deficient counterparts namely, $CaMnO_{2.5}$ (Mn^{3+}) and $CaMnO_2$ (Mn^{2+}).

Oxygen vacancies in orderly fashion along [001] rows of parent $CaMnO_3$ leads to $Ca_2Mn_2O_5$ which was reported by Poeppelmeier *et al.* [4] to have brownmillerite structure with corner linked BO_5 square pyramids instead of BO_6 octahedra. The final product in topotactic reduction of $CaMnO_3$ produces rock-salt phased $CaMnO_2$ where the Mn^{2+} atoms are octahedrally coordinated, explored by A. Varela *et al.* recently [1]. The structural phase difference from perovskite type $CaMnO_3$ to rock-salt type $CaMnO_2$ suggests strong diffusion of oxygen atoms.

Here in conjunction with experimental inputs, we carried out our calculations on the two oxygen deficient compounds of well known perovskite $CaMnO_3$ namely $CaMnO_2$ and $CaMnO_{2.5}$.

For $CaMnO_2$ we made in depth analysis of its local structure. Our study together with experimental results showed that a locally phase separated structure with locally ordered regions terminated by antiphase boundaries is favoured over disordered rock-salt structure with average occupancy of sites by Ca and Mn atoms. The microscopic origin of stabilization of such locally phase separated structure was found to be due to an increased Mn-O covalency as well as Mn-Mn magnetic exchange interactions at antiphase boundary.

In the case of oxygen deficient $CaMnO_{2.5}$, we carried out first-principles density functional theory based calculations to study its physical properties as this is a poorly studied compound lacking any detailed description of its electronic and magnetic properties. Moreover in order to improve their physical properties through anion chemistry we investigated the role of 'mixed anion chemistry' through fluorination. Our calculations established the stabilization of a unique up-up-down-down magnetic configuration in the un-fluorinated compound

with strong magneto-structural coupling, akin to that found in compounds like $HoMnO_3$ [5]. This establishes promise of these compounds as possible materials showing coupling between electron, spin and lattice degrees of freedom. We investigated the effect of fluorination, namely the site occupancy of F in the system. We found that F occupies both the interstitial site of the missing oxygen position of metal-oxygen octahedra, driven by the interplay of the tendency of Mn to be in octahedral environment instead of square pyramidal environment and the Mn valency in fluorinated compound to be close to 3+. The resultant structure of the fluorinated compound was found to break the inversion symmetry of the crystal locally through off-centric movement of F atom in the interstitial making the compound polar with finite polarization. This together with magnetism of Mn sublattice holds the promise to be high temperature multiferroic.

The detailed description of our study on the two oxygen deficient compounds $CaMnO_2$ and $CaMnO_{2.5}$ are discussed in the following.

3.1 Re-examining the nature of ordering in $CaMnO_2$: The role of Mn-O covalency in the local structure

As stated earlier $CaMnO_2$ is a oxygen deficient compound of $CaMnO_3$, obtained through topotactic reduction procedure. In this compound Mn adopts Mn^{2+} oxidation state i.e. d^5 configuration.

Previous study on this compound shows rock-salt type structure with random distribution of Ca^{2+} and Mn^{2+}. This structure on refinement gives a rock-salt type $CaMnO_2$ where the relative cationic distribution remains unaltered but the anionic assemblage undergoes a rearrangement to give rise to the rock-salt structure for $CaMnO_2$. From the study of A. Varela *et al.* [1], the schematic representation of the topotactic reduction procedure from perovskite $CaMnO_3$ to cubic rock-salt $CaMnO_2$ is shown in Fig. 3.1. This rock-salt structure can be derived from the cubic perovskite $CaMnO_3$ by viewing it from (111) direction. The cubic perovskite $CaMnO_3$ [cf. Fig. 3.1 (a)] has Ca/Mn 1:1 alternating arrangement. Next a hypothetical ordered rhombohedral structure [cf. Fig. 3.1 (b)] is constructed with the distribution of Ca and Mn in alternate planes along the stacking direction of the cubic rock-salt structure. Now upon reduction, the cationic sublattice remains unaltered but removal of two out of three oxygens around each Mn atom compels the third oxygen atom to rearrange and form a rhombus like Fig. 3.1 (c). This rhombus upon rotation can be recognized as an ordered rock-salt structure of oxygen deficient $CaMnO_2$ [cf. Fig. 3.1 (d)].

In this ordered structure each Mn atom is coordinated by 6 Mn/6 Ca atoms with distance 3.27 Å. The topotactic reduction procedure followed here raises the

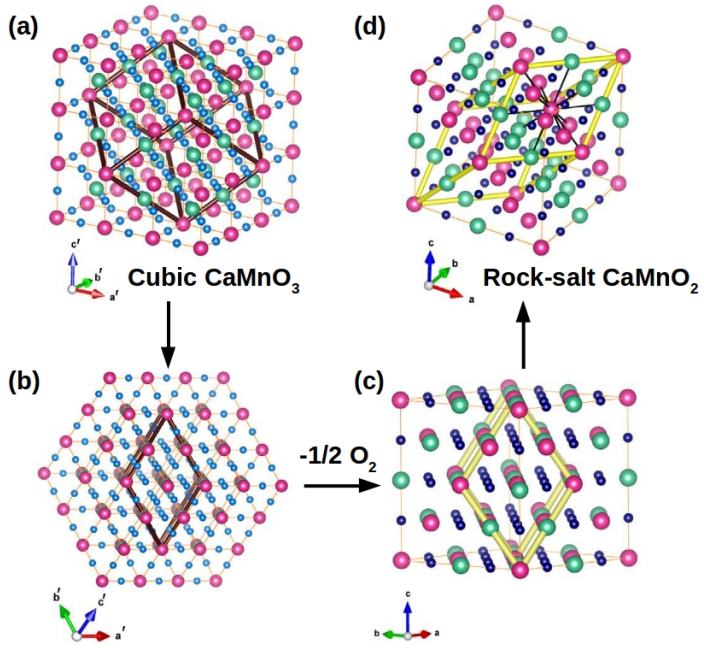

Figure 3.1: Schematic representation of topotactic reduction from $CaMnO_3$ to $CaMnO_2$. (a) Parent cubic perovskite $CaMnO_3$, (b) hypothetical rhombus with rock-salt ordering of Ca and Mn, (c) rhombus after removal of two out of three oxygen atoms around each Mn atom and (d) final product $CaMnO_2$ with rock-salt arrangement. Green and pink balls represent Ca and Mn atoms respectively. Small sky balls in (a) and (b) represent the oxygen atoms. Dark blue small balls in (c) and (d) represent reoriented oxygen atoms after oxygen removal.

expectation to have observable specific site preferences of Ca and Mn. However no Ca/Mn long-range ordering was observed in experimental observation through selected area electron diffraction (SAED), though it does not preclude the presence of local ordering [1].

Thus all these necessitate to investigate the local stucture at microscopic level so that a proper chemical structure of this oxygen deficient compound $CaMnO_2$ can be constructed.

Our experimental collaborators probed the local structure using x-ray absorption fine structure spectroscopy (XAFS) in its near edge (XANES) and extended (EXAFS) spectral regions for their chemical selectivity and short range order sensitivity [6–10]. The experimental collaborative results show that no 6 Mn/6 Ca arrangement around each Mn is retained rather it shows a very different cationic arrangement at the local level.

3.1.1 Crystal structure of $CaMnO_2$ from collaborative experimental findings

The x-ray diffraction (XRD) pattern of $CaMnO_2$ shows cubic crystal structure belonging to $Fm\bar{3}m$ space group symmetry with random distribution of Ca and Mn atoms in rock-salt type structure [cf. Fig. 3.2 (a) top panel]. The corresponding lattice parameter is 4.6328 Å. The structure is then refined on the basis of ordered arrangement of Ca and Mn atoms [cf. Fig. 3.2 (a) bottom panel] obtained through topotactic reduction. The fitting of XRD data establishes the inherent tendency of chemical disorder of the structure and 6 Mn/6 Ca nearest neighbour coordination around each Mn.

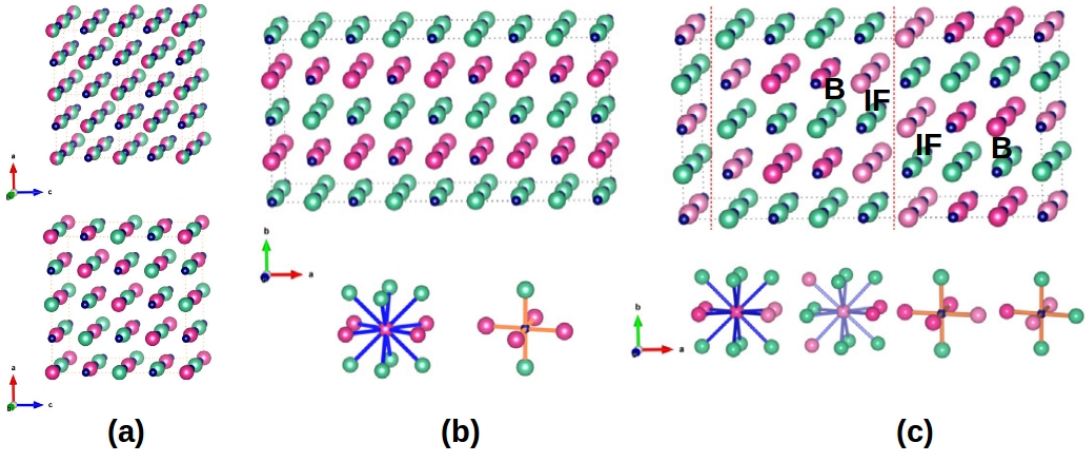

Figure 3.2: (a) Top panel: Disordered structure, Ca, Mn are randomly oriented. Bottom panel: Refined rock-salt arrangement of $CaMnO_2$. (b) Top panel: Structure-I with alternate layers of Ca and Mn atoms. Bottom panel: Coordination of Mn and O in structure-I. (c) Top panel: Structure-II with antiphase boundary separating between bulk (B) and interface (IF) atoms. Bottom panel: Coordination of bulk (B) and interface (IF) Mn and O in structure-II. Green, pink, light pink and dark blue balls represent Ca, bulk Mn, interface Mn and O atoms respectively.

Local structure analysis with extended x-ray absorption fine structure spectroscopy and structure modelling

Local structure analysis has been done with the k^3 weighted extended x-ray absorption fine structure spectroscopy (EXAFS). The structural parameters obtained from this experiment are tabulated in the following Table-3.1. The results show that the shell distances are close to that of the crystallographic model only with slight expansion of Mn-Ca distance with respect to Mn-Mn distance. The nearest neighbour analysis shows the presence of octahedrally coordinated

Mn atoms with nearest neighbour distance 2.23 Å. The next-nearest neighbour analysis shows that each Mn atom has 8.4 (≈ 8) Ca and 3.6 (≈ 4) Mn neighbours. This suggests chemical modification for which Ca becomes preferable over Mn, around each Mn atom.

Shell	N	R (Å)	R_{th} (Å)
Mn-O_I	6.0**	2.233(5)	2.31
Mn-Mn_{II}	3.6(2)	3.19(1)	3.27
Mn-Ca_{II}	8.4*	3.30(1)	
Mn-O-Mn_{III}(SS+MS)	4.2(4)	4.50(2)	4.63
Mn-O-Ca_{III}(SS+MS)	1.8*	4.67(2)	
Mn-Mn_{IV}	8**	5.72(4)	5.67
Mn-Ca_{IV}	16**	5.68(4)	
Mn-Mn-Mn_V	4**	6.49(5)	6.55
Mn-Ca-Mn_V	8**	6.39(5)	

Table 3.1: Structural results obtained through Mn K-edge x-ray absorption fine structure spectrum refinement for $CaMnO_2$. The constrained and fixed parameters are labelled by * and ** respectively. N represents the coordination number. Standard uncertainty of the free parameter on the last digit are also reported in parenthesis. The expected interatomic distances are reported for comparison and denoted as R_{th}. SS and MS represent single and multiple scattering respectively.

However this 8 Ca/4 Mn cationic ordering is fully local and the system retains its global disordered nature to match with its bulk diffraction pattern. Going into the third shell it is found that Mn-O-Mn is preferred over Mn-O-Ca.

Based on these experimental findings and coordination numbers, a model structure namely structure-I [cf. Fig. 3.2 (b) top panel] is constructed with alternate layers of Mn and Ca where each Mn is coordinated with 8 Ca and 4 Mn atoms [cf. Fig. 3.2 (b) bottom panel].

Next for checking the validity of this modelled structure, the EXAFS experiment is extended about 6.5 Å and the results establish the preference of dissimilar cationic arrangement around Mn atom which suggests a locally ordered Ca/Mn arrangement differing from the rock-salt arrangement. Thus to keep the global inherent disorderness another alternative structure namely structure-II is modelled with a antiphase boundary which interrupts a Mn layer by a Ca layer separating the bulk (B) and interface (IF) atoms [cf. Fig. 3.2 (c) top panel]. In this structure the 8 Ca/4 Mn coordination number is kept intact with a difference in the arrangement of the Ca and Mn atoms for the bulk and interface Mn atoms as shown in the bottom panel of Fig. 3.2 (c). The coordination of oxygen atoms as shown in Fig. 3.2 (c) bottom panel, reveals that the bulk and the interface oxygen atoms are octahedrally coordinated with a difference in the position of Ca and Mn atoms around it.

With these two modelled structures, structure-I and structure-II based on experimental observations, we carried out density functional theory (DFT) based calculations being interested to find out the most preferred structure for the com-

pound $CaMnO_2$.

3.1.2 Theoretical methods

We carried out the theoretical calculations employing the first-principles density functional theory (DFT) [11] which considers the complete structural as well as chemical information. Our DFT calculations were carried out in the plane-wave basis as implemented in the Vienna Ab-initio Simulation Package (VASP) [12] with projector-augmented wave (PAW) potential [13]. Generalized gradient approximation (GGA) for the exchange correlation functional was used with Perdew-Burke-Ernzerhof prescription [14]. The strong electron-electron correlation at Mn site beyond GGA, was taken into calculation through supplemented Hubbard U correction in terms of GGA+U [15] calculation with the choice of $U = 4$ eV and Hund's coupling parameter, J_H of 0.8 eV to handle the multiorbital situation. The results were checked and found to be robust by varying 1-2 eV of the U parameter. We expanded the 1×1×1 cubic unit cell of $CaMnO_2$ in $Fm\bar{3}m$ symmetry to 4×2×2 supercell in order to accommodate the local structural pattern observed experimentally. We set the energy cutoff of 560 eV and Monkhorst-Pack k-points mesh of 8×8×8 for the unit cell and 2×4×4 to provide good convergence of the total energy in self-consistent field calculations.

3.1.3 Theoretical results

To investigate the stability between these two structures, we carried out spin-polarized DFT calculations in GGA+U framework. The spin-polarized DFT calculations within GGA+U gave insulating solution for both the structures. The calculated total magnetic moment was found to be 5 μ_B/f.u where the magnetic moment of Mn site is $\approx$ 4.5 μ_B and the remaining moment is distributed over oxygen sites suggesting the presence of finite Mn-O covalency.

The calculated density of states (DOS) of structure-I and structure-II in Fig. 3.3 (a) revealed a remarkable trend. The overall DOS features are similar of these two structures but DOS of structure-I shows a sharp feature right at Fermi level, followed by the flat Mn e_g and O p hybridized bands. This sharp feature near Fermi is absent for structure-II. This difference in DOS structure near Fermi is marked by the rectangle and the inset shows its zoomed view. The DOS structure suggests structure-I to have higher energy than structure-II which got supported with our total energy calculations. Structure-II was found to have lower energy than structure-I by an energy difference of 45 meV/f.u. Next we took the experimentally observed antiferromagnetic arrangement of Mn atoms where the ferromagnetically ordered Mn^{2+} cations are antiferromagnetically coupled to the neighbouring sheets along (111) direction [1]. Comparing the computed total energy this particular magnetic arrangement is found to have $\approx$ 100 meV/f.u. lower

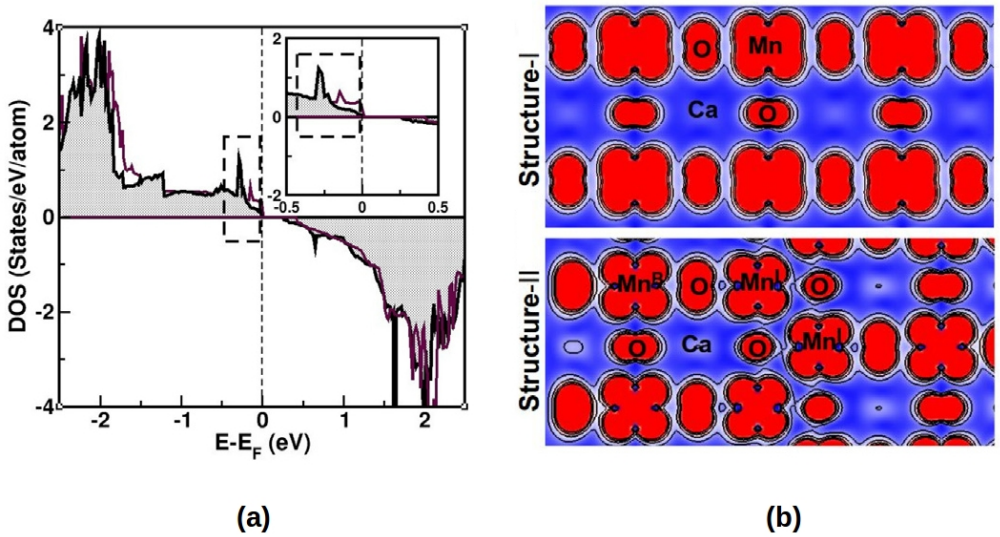

Figure 3.3: (a) Density of states projected on the Mn-*d* orbitals of structure-I and structure-II are denoted in purple solid and black shaded respectively. The difference of density of states of the two structures near Fermi energy (E_F) is highlighted with a box and the zoomed view is shown in the inset. (b) Charge density plots for structure-I (top) and structure-II (bottom), with the choice of maximum and minimum isosurface values of 0.02 $e^-/Å^3$.

energy than its ferromagnetic spin arrangement. This energy difference further increased to 60 meV/f.u. suggesting the significant contribution of magnetism in the stabilization of structure-II over structure-I.

The stability of structure-II can also be anticipated on the basis of anionic stability through its arrangement in the MnO-CaO binary system [16]. Accommodation of a larger cation in a close packed face centred cubic (FCC) lattice modifies the cation-anion distance in such a way that it will make a room for the larger cation to sit in. This cation-anion distance modification is easier when the anion has dissimilar cationic environment. Here the accommodation of larger cation Ca^{2+} with radius 1.08 Å [17] in close packed FCC lattice is favoured in dissimilar cationic environment, Mn-O-Ca of structure-II over similar cationic environment, Mn-O-Mn and Ca-O-Ca of structure-I, as the anion O^{2-} adjacent to Ca^{2+} cation can shift towards smaller cation Mn^{2+} of radius 0.83 Å [17]. This anionic shift towards Mn^{2+} helped the cation-anion i.e. Mn-O bond to adopt more covalent character by decreasing the Mn-O bond length. The covalency was also facilitated due to the presence of half filled *d* orbitals of transition metal Mn atom, favouring the easy exchanges of electrons in the orbitals [16]. Thus cationic arrangement around O^{2-} plays an important role and presence of dis-

similar cation arrangement in structure-II due to antiphase boundary facilitates the stabilization of structure-II over structure-I.

Next we calculated the crystal orbital Hamiltonian population (COHP) [18–22] integrated until Fermi level for both the structures. COHP basically makes partition of the band structure energy in terms of orbital-pair contribution. For the interaction of two orbitals namely μ and ν, the Hamiltonian matrix becomes $H_{\mu\nu} = \langle\phi_\mu|\hat{H}|\phi_\nu\rangle$ and the multiplication of this with the corresponding density of states matrix gives the quantitative measure of bonding strength by either lowering (bonding) or raising (antibonding) the band structure energy [19].

Our calculated COHP value reflects the enhanced Mn-O covalency in structure-II. The calculated COHP value for structure-II was found to be 0.2 eV higher than that of structure-I. The comparison of calculated covalency of structure-I and structure-II is shown in Fig. 3.3 (b). The bottom panel of Fig. 3.3 (b) shows the enhanced Mn-O covalency at the antiphase boundary in structure-II which is absent in structure-I as shown in the top panel of the figure.

Next we analysed the dominant exchange interaction paths in order to investigate the role of magnetism. In structure-I, all the Mn sites are equivalent [cf. Fig.

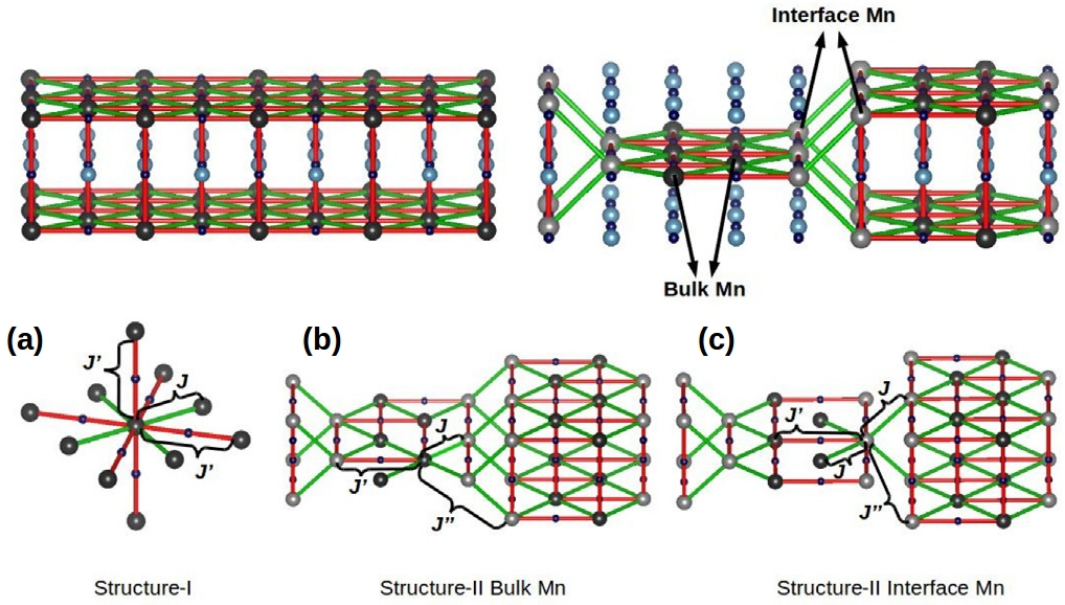

Figure 3.4: Top panel: Geometry of $CaMnO_2$ for structure-I (left) and structure-II (right). Sky, gray, dark blue balls represent Ca, Mn and O respectively. The bonds depict the nearest (green) and next-nearest (red) neighbour interactions. Bottom panel: (a) Mn-Mn exchange couplings J, J' in structure-I. (b) Mn-Mn exchange couplings J, J', J'' for bulk Mn atoms in structure-II. (c) Mn-Mn exchange couplings J, J', J'' for interface Mn atoms in structure-II.

3.4 top left panel] but in structure-II, the Mn sites belong to inequivalent interface and bulk atoms due to antiphase boundary as shown in the top right panel of Fig. 3.4. Structure-I has two types of magnetic exchanges, nearest neighbour (NN) J mediated through 90° Mn-O-Mn path and next-nearest neighbour (NNN) J' interactions through 180° Mn-O-Mn path as shown in Fig. 3.4 (a) bottom panel.

Table-3.2 lists the number of in-plane and out-of-plane NN and NNN interactions for structure-I.

Mn-Mn distance Å	**∠ Mn-O-Mn °**	**Exchange interaction**	**No. of interactions**
3.28	90	J	4 in-plane
4.64	180	J'	4 in-plane 2 out-plane

Table 3.2: Details of the exchange interactions of structure-I.

In structure-II, the magnetic exchange interactions of bulk Mn atoms remain the same as that in structure-I but the exchange interactions for the interface Mn atoms differ. Due to the antiphase boundary one NNN J' interaction becomes missing whereas a third NN interactions J'' appear as shown in Figs. 3.4 (b) and 3.4 (c) for bulk and interface Mn atoms respectively. The detailed description of the exchange interactions for both bulk and interface Mn atoms of structure-II is given in Table-3.3 and Table-3.4 respectively.

Mn-Mn distance Å	**∠ Mn-O-Mn °**	**Exchange interaction**	**No. of interactions**
3.28	90	J	4 in-plane
4.64	180	J'	3 in-plane, one missing in-plane 2 out-plane
5.67		J''	12 out-plane

Table 3.3: Details of the exchange interactions of bulk Mn atoms of structure-II.

Mn-Mn distance Å	**∠ Mn-O-Mn °**	**Exchange interaction**	**No. of interactions**
3.28	90	J	2 in-plane, 2 out-plane
4.64	180	J'	3 in-plane, one missing in-plane 2 out-plane
5.67		J''	12 out-plane

Table 3.4: Details of the exchange interactions of interface Mn atoms of structure-II.

Thus the number of third NN interactions is 12 for the interface Mn as well as for the bulk Mn atoms. The strength of J'' is expected to be much smaller than J' as the connecting Mn-Mn distance increases and our DFT total energy calculation for different spin alignment of Mn atoms estimates the strength of $J'' \approx \frac{1}{5} J'$. Although the total combined effect of the newly appeared interaction J'' surpasses the effect of the total missing interactions J' resulting into overall magnetic energy gain in structure-II over structure-I. This further facilitates the overall covalency energy gain in stabilization of structure-II.

3.1.4 Summary

Our collaborative experimental study employing local probes together with our first-principles electronic structure calculations reveal a very different chemical structure of $CaMnO_2$ at microscopic level in contrast to the random Ca/Mn distribution as concluded from the diffraction like bulk probe.

The most stable structure for $CaMnO_2$, derived out of local probe consists of alternate arrangements of Mn and Ca layers with a shift due to antiphase boundary. These chemically ordered regions with a short coherence length are limited by antiphase defects. The local distribution of cations around oxygen plays an important role in Mn-O covalency which is also supported by our *ab-initio* calculations. Analysis of dominant magnetic exchange interactions also supports the overall magnetic energy gain of the structure with local ordering supporting the stabilization of this structure.

3.2 Mixed Anion Physics in Flourinated vacancy ordered Brownmillerite: A possible route to Multiferrocity

The simultaneous presence of strong coupling of electric and magnetic degrees of freedom makes multiferroics technologically very important for their numerous application in spintronics. Multiferroics can be classified into two categories: (i) type-I multiferroics, where the origins of ferroelectricity and magnetism are different and independent to each other, and (ii) type-II multiferroics, where the magnetism drives the ferroelectricity and both are strongly coupled.

Type-I multiferroics are further grouped into 3 classes on the basis of their lone pair, charge order and geometric distortion [23, 24]. Previous studies in search of multiferroics, focused on oxide compounds.

There were very few exceptions of compounds with anion other than oxygen, to be multiferroic [25–30].

Recently mixed-anion compounds are in lime light as the cation is bonded to more than one type of anion which may show interesting properties. The variation in charge, ionic radii, electronegativity, and polarizability due to the presence of different anions plays an important role in showing unusual properties which are inaccessible in single anion counterparts [31–38].

These compounds have significant importance in the field of catalysis, energy conversion, electronic devices, magnetism and ferroelectricity, driven by the introduction of local noncentrosymmetricity [39–41].

Incorporation of second anion in the oxygen deficient compounds of perovskites brings back the octahedral coordination of the TM atom. Inherent polar nature or acentricity can be developed by these pseudo-octahedra e.g. MnO_5X^{m-},

$MnO_4X_2^{n-}$, $MnO_3X_3^{p-}$ where X is the second anion. These may give rise to finite polarization lowering the symmetry of the system [40, 42].

In this joint theoretical and experimental work, we have studied brownmillerite structured $CaMnO_{2.5}$, obtained through the oxygen removal in orderly fashion along (001) rows of cubic perovskite $CaMnO_3$. Ordered oxygen vacancies create corner linked MO_5 square pyramids instead of the MO_6 octahedra, forming regular void patterns and three inequivalent oxygen atoms with the alternate network of Mn-Mn short and long bonds, as shown in Fig. 3.5.

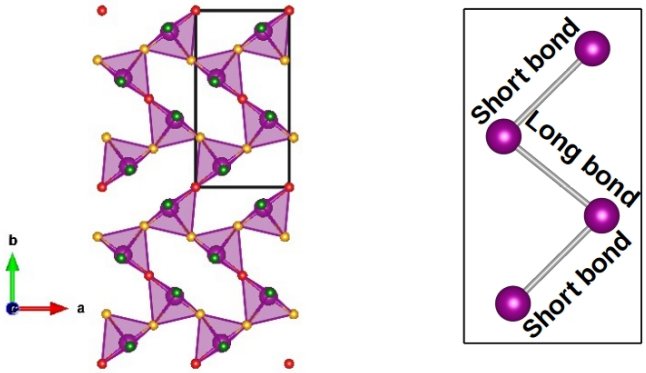

Figure 3.5: Left panel: Crystal structure of $CaMnO_{2.5}$. Formation of regular voids by the corner shared network of MnO_5 square pyramids. Ca atoms are removed for clarity. Mn atoms are represented by purple balls. Three inequivalent oxygen atoms, O1, O2, O3 are represented by green, yellow and red balls respectively. Right panel: Alternating arrangement of Mn-Mn short and long bonds in the *ab*-plane.

We chose fluorine (F) as the best suited anion to be incorporated in the system to investigate the effect of mixed anion chemistry as the radius of F ion (r_F^- = 1.33 Å) is comparable to that of oxygen anion (r_O^{2-} = 1.40 Å).

3.2.1 Collaborative experimental results

Results from Rietveld refinement of x-ray diffraction (XRD) data collected at 300 K suggests that $CaMnO_{2.5}$ crystallizes in orthorhombic *Pbam* space group consisting of distorted MnO_5 square pyramids [cf. Fig. 3.5 left panel]. The refined lattice parameters are in good agreement with the parameters obtained from neutron powder diffraction (NPD) refinement confirming the presence of single crystalline phase. The corresponding lattice parameters are a = 5.437 Å, b = 10.238 Å, c = 3.749 Å.

Analysis of magnetic Bragg peak indicates room temperature antiferromagnetic order with up-up-down-down spin arrangement along the c axis. The ob-

served magnetic moment of each Mn site is 2.235 μ_B. The high-temperature antiferromagnetic order, confirmed through high-temperature susceptibility measurement, shows the Néel temperature (T_N) at 335 K.

Due to the inability of x-ray diffraction pattern and neutron scattering to distinguish between O^{2-} and F^- anions with the same electronic configuration, x-ray photoelectron spectroscopy (XPS) and x-ray absorption near edge spectroscopy (XANES) are extensively used to determine the actual position of fluorine in the parent compound $CaMnO_{2.5}$ upon fluorination.

The XPS spectrum of F 1s in $Ca_2Mn_2O_{5-x}F_y$ shows double peak characteristic indicating the presence of two different chemical environments of F^- i.e the fluorine may be in the interstitial position as well as substituting oxygen in the parent compound $Ca_2Mn_2O_5$. Analysis of Mn K-edge positions in XANES experiment gives the valence of Mn as 3.26+ and 3.43+ in $Ca_2Mn_2O_5$ and $Ca_2Mn_2O_{5-x}F_y$ respectively suggesting the increment of Mn valency upon fluorination. However substitution of O^{2-} by F^- should decrease the Mn valence to maintain the charge neutrality but here the enhanced valency of Mn suggests incorporation of F^- in the interstitial voids as well.

Investigation of the proper atomic position of F^- in the system upon fluorination has been done with x-ray absorption fine structure spectroscopy (XAFS). The results are listed in Table-3.5. Negligible changes are observed in Mn-O, Mn-Ca and Mn-Mn and Mn-O-Mn-O between the parent compound $Ca_2Mn_2O_5$ and its fluorinated counterpart $Ca_2Mn_2O_{5-x}F_y$. The significant change is observed due to the presence of an extra bond of Mn atom with F which fulfils the octahedral coordination of Mn atom suggesting the interstitial occupation of F. Results also show the shortening of Mn-F-Mn distance in comparison to that of Mn-O-Mn as a consequence of shorter Mn-F bond length to that of Mn-O. Although EXAFS remained unable to produce result on oxygen substitution by fluorine. Taking

	$Ca_2Mn_2O_5$		upon fluorination	
Shell	***N***	***R* (Å)**	***N***	***R* (Å)**
Mn-O	4*	1.883(6)	4*	1.924(7)
Mn-O	1*	1.93(1)	1*	2.01(1)
Mn-Ca	8*	3.1627	8*	3.17(2)
Mn-Mn	5*	3.6312	5*	3.7019
Mn-O-Mn (MS)	10*	3.7812	10*	3.7915
Mn-O-Mn-O (MS)	5*	3.9312	5*	3.8812
Mn-F			1*	1.796(7)
Mn-Mn			1*	3.53(1)
Mn-F-Mn			2*	3.53*
Mn-F-Mn-F			1*	3.53*

Table 3.5: Structural results obtained through Mn K-edge x-ray absorption fine structure spectrum refinement for $Ca_2Mn_2O_5$ and upon its fluorination. The constrained values are labelled by *. N represents the coordination number. Standard uncertainty of the free parameter on the last digit are also reported in parenthesis. MS represents multiple scattering.

the results of EXAFS as input, neutron powder diffraction (NPD), carried out at different temperatures, revealed the major phase presence of *Pbam* space group with lattice constants $a = 5.055$ Å, $b = 9.729$ Å, $c = 4.629$ Å for the fluorinated counterpart. The results show the presence of F at interstitial with occupancy 0.463 completing the MnO_5F octahedra of Mn which is in good agreement with the EXAFS analysis.

The Bond Valence Sum (BVS) [43] calculation hints that oxygen substitution is most favourable at the O3 site.

The high temperature susceptibility data of the fluorinated counterpart shows antiferromagnetic transition at 340 K with 3.04 μ_B magnetic moment at each Mn site. The antiferromagnetic arrangement upon fluorination remains the same as that in the unfluorinated system, only the spins take a 90° turn and align along the b axis and at higher temperature becomes canted in the ab-plane.

The presence of mixed valent Mn^{3+} and Mn^{4+} due to fluorination, induces ferrimagnetic interaction. The butterfly loop of strain vs. electric field establishes ferroelectric switching nature of the fluorinated system indicating the role of noncentrosymmetricity due to fluorination.

In order to verify these results and investigate the site occupancy of F in the system in detail, we have carried out first-principles density functional theory based calculations. Our study also provides microscopic insight on the origin of noncentrosymmetricity upon fluorination to exhibit multiferroicity.

3.2.2 Computational details

We have applied *ab-initio* method of calculations based on a single particle approximation to study the fluorinated counterparts of oxygen deficient $CaMnO_{2.5}$. Here we have used plane-wave basis set as implemented in Vienna Ab-initio simulation package (VASP) [12] for our *ab-initio* calculations with projector-augmented wave (PAW) potential [13]. The exchange correlation functional was chosen to be of generalized gradient approximation (GGA) implemented in Perdew-Burke-Ernzerhof (PBE) prescription [14]. Strong electron-electron correlation at Mn site beyond GGA, was checked through supplemented Hubbard U through GGA+U calculation [15]. We made the choice of $U = 4$ eV and Hund's coupling $J_H = 0.8$ eV to handle the multi orbital situation. Energy cut-off of 560 eV and Monkhorst-Pack k-points mesh of 6×4×6 for the unit cell of $CaMnO_{2.5}$ and its fluorinated counterparts were found to provide good convergence of the total energy in self-consistent field calculations. For calculating the magnetic exchanges, the orthorhombic unit cell of $CaMnO_{2.5}$ in *Pbam* symmetry was expanded to a 1×1×2 supercell in order to accommodate different magnetic exchange interactions in all directions.

3.2.3 Theoretical results

Results on un-fluorinated $CaMnO_{2.5}$

In order to find out the ground state magnetic arrangement, we made total energy calculation of different magnetic arrangements of Mn spins and results established the stabilization of unique up-up-down-down [cf. Fig. 3.6 (b)] magnetic configuration in the un-fluorinated compound $CaMnO_{2.5}$ with strong magneto-structural coupling.

Next we made analysis of the different magnetic exchange interactions present in the system as shown in right panel of Fig. 3.6.

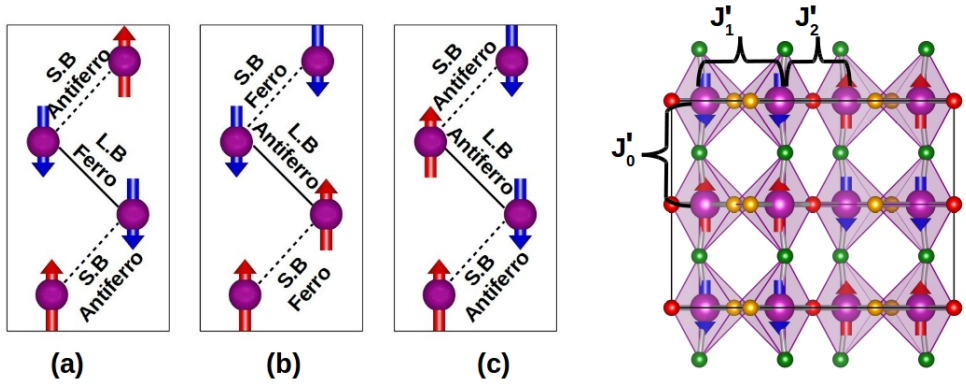

Figure 3.6: Left panel: different magnetic arrangements of the un-fluorinated unit cell of $CaMnO_{2.5}$. Magnetic arrangements are with, (a) antiferromagnet short bond and ferromagnetic long bond, (b) ferromagnetic short bond and antiferromagnetic long bond, and (c) antiferromagnetic both the short and long bond. S.B and L.B denote the short bond and long bond respectively. Right panel: different magnetic exchanges J'_0, J'_1 and J'_2 with the ground state magnetic arrangement of $CaMnO_{2.5}$. The colour codes of the balls are same as that in Fig. 3.5.

The calculated exchange interactions from the total energy calculation of different magnetic arrangements are tabulated in Table-3.6. Our theoretical cal-

Exchange interaction	GGA	GGA+U
J'_0 ∠Mn-O1-Mn = 170.7°	-1.308 ± 0.204	-0.536 ± 0.116
J'_1 ∠Mn-O2-Mn = 156.4°	0.307 ± 0.051	0.895 ± 0.084
J'_2 ∠Mn-O3-Mn = 180°	-3.010 ± 1.229	-1.395 ± 0.169

Table 3.6: Calculated different magnetic exchange interactions (meV) in GGA and GGA+U scheme from the total energy calculation of different magnetic arrangements of $CaMnO_{2.5}$.

culations show that each Mn with distorted square pyramidal coordination, is antiferromagnetically coupled through O1 (J_0') and O3 (J_2') atoms and ferromagnetically coupled through O2 atom (J_1') as shown in Fig. 3.6 right panel. It is evident from the calculation that J_1' is the weakest interactions and the magnetic ground state of $CaMnO_{2.5}$ is dominated by antiferromagnetic J_0' and J_2' interactions.

The calculated total strength of exchange interactions in GGA scheme is 31.86 meV which is equivalent to 369.58 K in temperature scale, close to the Néel temperature (335 K), experimentally found by our collaborators.

The magnetic structure with ferromagnetic short Mn-Mn bonds and antiferromagnetic long Mn-Mn bonds along the chain suggests the presence of strong spin-phonon coupling and exchange-striction which optimizes the spin-exchange

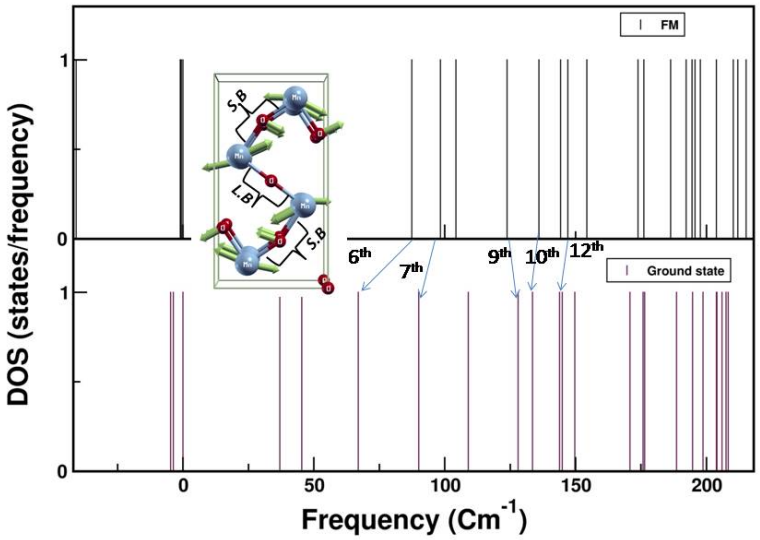

Figure 3.7: Matching of phonon frequencies (cm^{-1}) of $CaMnO_{2.5}$ taking the ferromagnetic and ground state magnetic arrangement. The first 24 phonon modes are shown. Crystal structure of $CaMnO_{2.5}$ with corresponding atomic shifts in the matched lowest mode is also shown. S.B and L.B denote short bond and long bond respectively. Blue and red balls represent Mn and oxygen atoms respectively in the structure. Ca balls are not shown.

energy by shifting the ions. Here in the short Mn-Mn bond, the $\angle Mn-O-Mn$ $< 180°$ plays a crucial role to shift the oxygen ions perpendicular to the Mn-Mn bond. Fig. 3.7 reveals the spin-phonon coupling considering the ground state magnetic arrangement and ferromagnetic arrangement showing the softening of phonon mode upon changed magnetic configuration driven by the change in $\angle Mn-O-Mn$ bond angle in short Mn-Mn bond.

Fluorination of $CaMnO_{2.5}$

Next in order to investigate the effect of fluorination on $CaMnO_{2.5}$, we took the indication of increased Mn valency upon fluorination from our collaborative experimental observation through XANES and the plan of fluorination is depicted in Fig. 3.8.

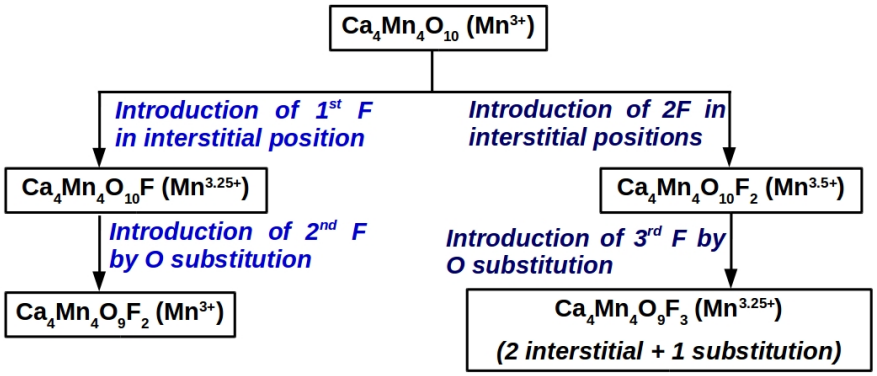

Figure 3.8: Flow chart of fluorination process of $CaMnO_{2.5}$.

Inserting F in the interstitial region and then by oxygen substitution for the case of $Ca_4Mn_4O_9F_2$ and $Ca_4Mn_4O_9F_3$, we have calculated the total energy required to substitute O from three inequivalent O sites and the results are tabulated in Table-3.7. Our calculation thus establishes the preference of oxygen

	F at O1 site	F at O2 site	F at O3 site
$\mathbf{Ca_4Mn_4O_9F_2}$	3.0396	2.7173	2.3893
$\mathbf{Ca_4Mn_4O_9F_3}$	2.2148	1.8964	1.7923

Table 3.7: Calculated total energy (eV) needed to substitute oxygen atoms from O sites for $Ca_4Mn_4O_9F_2$ and $Ca_4Mn_4O_9F_3$.

substitution from the O3 site when the interstitial site is preoccupied by the F atom.

In order to check the stability of different possible fluorinated counterparts of $CaMnO_{2.5}$, we calculated formation enthalpies of each compounds. We used Eq. (3.1) to calculate formation enthalpy,

$$\Delta H(A_{n1}B_{n2}...) = E_{total}(A_{n1}B_{n2}...) - \sum_i n_i \mu_i^0 \tag{3.1}$$

where, $E_{total}(A_{n1}B_{n2}...)$ is the total energy/f.u of a given compound $A_{n1}B_{n2}...$, and μ_i^0 are the chemical potentials of the constituting elements A, B,... in their elemental reference phases. Then we computed the obtained formation enthalpies

for per atom as the total number of different compounds are not the same. We used the following chemical potentials for our calculation, [44]

$$\mu_{Ca} = -1.93eV$$
$$\mu_{Mn} = -6.97eV$$
$$\mu_{O} = -4.99eV$$
$$\mu_{F} = -1.86eV$$

Our calculated formation enthalpies for different compounds are listed in Table-3.8. Enthalpy calculation shows that the formation enthalpy decreases whenever

Site occupancy of F	**Compound formula**	**Mn valency**	**Enthalpy eV**	**Shift from centroid Å**
Un-fluorinated	$Ca_4Mn_4O_{10}$	3	-2.514	
1 O/u.c. in interstitial	$Ca_4Mn_4O_{11}$	3.5	-2.505	0.0021
1 F/u.c. in interstitial	$Ca_4Mn_4O_{10}F$	3.25	-2.564	0.0010
1 F/u.c. in interstitial + 1 O/u.c. substitution	$Ca_4Mn_4O_9F_2$	3	-2.342	0.4463
2 F/u.c. in interstitial	$Ca_4Mn_4O_{10}F_2$	3.5	-2.607	0.0005 (C1F1), 0.0021(C2F2)
2 F/u.c. in interstitial + 1 O/u.c. substitution	$Ca_4Mn_4O_9\ F_3$	3.25	-2.675	0.5388 (C1F1), 0.4028 (C2F2)

Table 3.8: Comparison of calculated formation enthalpies (eV/atom) and shift from the centroid position for different fluorinated counterparts of $CaMnO_{2.5}$.

the number of fluorine sitting in the interstitial position (with or without substitution) increases. This is because the addition of fluorine in the interstitial position, makes the MnO_5F octahedra complete.

The formation enthalpy becomes the most stable for $Ca_4Mn_4O_9F_3$ suggesting that the fluorination is most favoured when the Mn atom restores its missing octahedral coordination by accommodating two F in interstitials and substituting O from O3 site without making huge change in its oxidation state from that of the un-fluorinated system. Thus the interplay between octahedral completion and making the Mn valence close to 3+ makes $Ca_4Mn_4O_9F_3$ the most favourable amongst all the possibilities.

Our calculation also confirms that fluorine is not off-centered when the system incorporates fluorine in the interstitial site(s) only but it becomes off-centered together with substitution and interstitial occupancies. This off-centric placement of fluorine can give rise to finite polarization in the system.

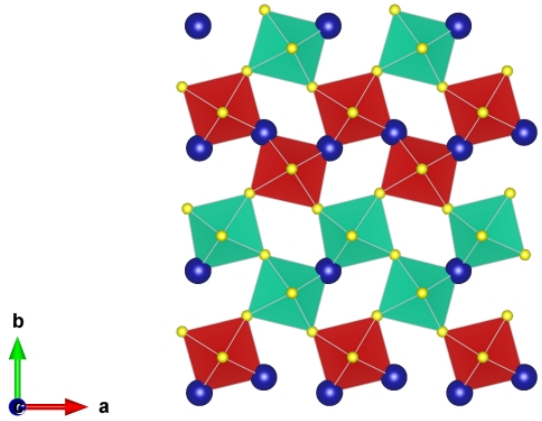

Figure 3.9: The most preferred fluorinated counterpart $Ca_4Mn_4O_9F_3$. The red and cyan coloured Mn octahedra contain double and single F respectively. The big blue and small yellow balls represent F and oxygen atoms respectively. Ca atoms are removed for clarity.

The most preferred fluorinated counterpart $Ca_4Mn_4O_9F_3$ shown in Fig. 3.9 which reveals that upon fluorination some of the Mn octahedra contain single F atom (MnO_5F) and some contain two F atoms (MnO_4F_2) which locally break the centrosymmetric nature of the structure leading to finite polarization suggesting a good agreement with our collaborative experimental findings and holds the promise to be a multiferroic.

3.2.4 Summary

Through compilation of experiment and theory, we have investigated the mixed anion chemistry through fluorination of $CaMnO_{2.5}$ manipulating the anionic sublattice. We made in depth investigation of the site occupancy of F atoms in the system through our DFT calculations. With the aim to achieve room temperature multiferroic we made attempt to explore new route to multiferroicity though controlling the dopant fluorine concentration. Our study establishes the stabilization of oxygen substitution along with interstitial F introducing the local noncentrosymmetricity to lead finite polarization. Thus our work proposes anion engineering as an effective tool to exhibit multiferroicity.

Bibliography

[1] A. Varela, S. de Dios, M. Parras, M. Hernando, M. T. Fernández-Díaz, Angel R. Landa-Cánovas, and J. M. González-Calbet, J. Am. Chem. Soc. **131**, 8660 (2009).

[2] K. Zhang, X. P. Han, Z. Hu, X. L. Zhang, Z. L. Tao and J. Chen, Chem. Soc. Rev. **44**, 699 (2015).

[3] J. Suntivich, H. A. Gasteiger, N. Yabuuchi, H. Nakanishi, J. B. Goodenough and S. H. Yang, Nat. Chem. **3**, 546 (2011).

[4] K. R. Poeppelmeier, M. E. Leonowicz, and J. M. Longo, J. Solid State Chem. **44**, 89 (1982).

[5] S. Picozzi, K. Yamauchi, B. Sanyal, I.A. Sergienko and E. Dagotto, Phys. Rev. Lett. **99**, 227201 (2007).

[6] C. Meneghini, S. Ray, F. Liscio, F. Bardelli, S. Mobilio, and D. D. Sarma, Phys. Rev. Lett. **103**, 046403 (2009).

[7] T. Chakraborty, C. Meneghini, A. Nag, and S. Ray S, J. Mater. Chem. C **3**, 8127 (2015).

[8] T. Chakraborty, C. Meneghini, G. Aquilanti, and S. Ray, J. Phys. Condens. Matter **25**, 236002 (2013).

[9] S. Middey, P. Aich, C. Meneghini, K. Mukherjee, E. V. Sampathkumaran, V. Siruguri, P. Mahadevan, and S. Ray, Phys. Rev. B **94**, 184424 (2016).

[10] A. Bandyopadhyay, S. K. Neogi, A. Paul, C. Meneghini, I. Dasgupta, S. Bandyopadhyay, and S. Ray, Phys. Rev. B **95**, 024432 (2017).

[11] W. Kohn, L. Sham, Phys. Rev. A **140**, 1133 (1965).

[12] G. Kresse, *et al.*, Phys. Rev. B **54**, 11169 (1996).

[13] P. E. Blöchl, Phys. Rev. B **50**, 17953 (1994).

[14] J. P. Perdew, K. Burke, M. Ernzerhof, Phys. Rev. Lett. **77**, 3865 (1996).

[15] S. L. Dudarev, G. A. Botton, S. Y. Savrasov, C. J. Humphreys, A. P. Sutton, Phys. Rev. B **57**, 1505 (1998).

[16] C. O. Arean, F. S. Stone, J. Chem. Faraday Trans. I **75**, 2285 (1979).

[17] R. D. Shannon, Acta Crystallogr. A **32**, 751 (1976).

[18] R. Dronskowski, P.E. Blöchl, J. Phys. Chem. **97**, 8617 (1993).

[19] V. L. Deringer, A. L. Tchougreeff, R. Dronskowski, J. Phys. Chem. A **115**, 5461 (2011).

[20] S. Maintz, V.L. Deringer, A.L. Tchougreeff, R. Dronskowski, J. Comput. Chem. **34**, 2557 (2013).

[21] S. Maintz, V.L. Deringer, A.L. Tchougreeff, R. Dronskowski, J. Comput. Chem. **37**, 1030 (2016).

[22] S. Maintz, M. Esser, R. Dronskowski, Acta Phys. Polon. B **47**, 1165 (2016).

[23] D. Khomskii, Physics **2**, 20 (2009).

[24] M. Fiebig, T. Lottermoser, D. Meier and M. Trassin, Nat. Rev. Mater. **1**, 16046 (2016).

[25] Y. Zhang, L. Lin and J.-J. Zhang *et al.*, Phys. Rev. Mater. **1**, 034406 (2017).

[26] C. De, N. V. Ter-Oganessian, and A. Sundaresan, Phys. Rev. B **98**, 174430 (2018).

[27] S. Dong, J. M. Liu, and E. Dagotto, Phys. Rev. Lett. **113**, 187204 (2014).

[28] H. C. Wu, K. D. Chandrasekhar, J. K. Yuan, J. R. Huang, J.-Y. Lin, H. Berger, and H. D. Yang, Phys. Rev. B **95**, 125121 (2017).

[29] A. Miyake, J. Shibuya, M. Akaki, H. Tanaka, and M. Tokunaga, Phys. Rev. B **92**, 100406(R) (2015).

[30] L. Zhao, T. L. Hung, and C. C. Li *et al.*, Adv. Mater. **24**, 2469 (2012).

[31] M. Al-Mamouri, P. P. Edwards, C. Greaves, and M. Slaski, Nature **369**, 382 (1994).

[32] Y. I. Kim, P. M. Woodward, K. Z. Baba-Kishi, and C. W. Tai, Chem. Mater. **16**, 1267 (2004).

[33] Y. Kobayashi, M. Tian, M. Eguchi, and T. E. Mallouk, J. Am. Chem. Soc. **131**, 9849 (2009).

[34] Y. Kobayashi, *et al.*, Nat. Mater. **11**, 507 (2012).

[35] M. Jansen, and H. P. Letschert, Nature **404**, 980 (2000).

[36] F. Sauvage, V. Bodenez, H. Vezin, T. A. Albrecht, J.-M. Tarascon, and K. R. Poeppelmeier, Inorg. Chem. **47**, 8464 (2008).

[37] S. Yamanaka, J. Mater. Chem. **20**, 2922 (2010).

[38] Y. Kamihara, T Watanabe, M. Hirano, and H. Hosono, J. Am. Chem. Soc. **130**, 3296 (2008).

[39] H. Kageyama, K. Hayashi, K. Maeda, J. P. Attfield, Z. Hiroi, J. M. Rondinelli, and K. R. Poeppelmeier, Nat. Commun. **9**, 772 (2018).

[40] Y. Kobayashi, Y. Tsujimoto, and H. Kageyama, Annu. Rev. Mater. Res. **48**, 303 (2018).

[41] C. N. R. Rao, and C. R. Serrao, J. Mater. Chem. **17**, 4931 (2007).

[42] Paul A. Maggard, Tiffany S. Nault, Charlotte L. Stern, Kenneth R. Poeppelmeier, J. Solid State Chem. **175**, 27 (2003).

[43] I. D. Brown, and D. Altermatt, Acta Crystallogr., Sect. B: Struct. Sci. **41**, 244 (1985).

[44] V. Stevanović and S. Lany, X. Zhang, A. Zunger, Phys. Rev. B **85**, 115104 (2012).

Chapter 4

Understanding the curious magnetic state of Sr_3OsO_6*

4.1 Motivation

B site ordered double perovskites derived from perovskites ABO_3, take the form as $A_2BB'O_6$, where A is alkaline earth/rare earth and B is transition metal (TM). In these B site ordered double perovskites half of the B sites are substituted by another TM B′. The rock-salt ordering of B-B′ in double perovskites extends the structural variation over simple perovskites showing intriguing electronic and magnetic properties [1–3].

Double perovskites consisting of two different TM atoms at B and B′ sites include compounds with high T_C magnetic behaviour like Sr_2FeMoO_6 (T_C = 420 K) [4–7], Sr_2CrMoO_6 (T_C = 420 K) [8, 9], Sr_2CrWO_6 (T_C = 458 K) [10, 11], Sr_2CrReO_6 (T_C = 620 K) [12], ferrimagnetic compound like Ca_2MnOsO_6 [13], Dirac-Mott insulator like Ba_2NiOsO_6 [14].

Double perovskites with single TM ion instead of two TM ions e.g. Ba_2CaOsO_6 [15], Sr_2MgOsO_6 [16], Ca_2MgOsO_6 [16,17], Sr_2YReO_6 have been also synthesized. They have been reported to exhibit either antiferromagnetism or spin-glass-like behaviour.

A recent study on Sr_3OsO_6 [18], a double perovskite with single TM Os in B-B′ sublattice showing a ferromagnetic (FM) insulating state at high temperature ($\approx$ 1060 K), is unconventional and counterintuitive. The surprising facts are as

*Based on publication: **Shreya Das**, Anita Halder, Atasi Chakraborty, Indra Dasgupta, and Tanusri Saha-Dasgupta; **Phys. Rev. B 101, 184422 (2020)**.

follows:

i) It is expected that the presence of nonmagnetic Sr at the B′ site in the B-O-B′-O-B superexchange path hinders the TM-TM (Os-Os) magnetic interaction, ii) high T_C value is a property of $3d$ TM containing compounds rather than $5d$ TM like Os containing compounds, iii) the conventional knowledge shows that ferromagnets are metals and antiferromagnetism is associated with insulators.

Few known ferromagnetic insulators like EuO (T_C = 77 K) [19], $CdCr_2S_4$ (T_C = 90 K) [20], $SeCuO_3$ (T_C = 25 K) [21] are reported to be low T_C compounds. La_2NiMnO_6 [22] is a double perovskite to stand out as an exception with T_C value 280 K which is still a factor of 3-4 smaller than reported T_C value of Sr_3OsO_6.

The situation becomes further intriguing by the fact that replacement of Sr by Ca (Ca_3OsO_6), makes the compound antiferromagnetic with low transition temperature ($\approx$ 50 K) in monoclinic symmetry [23] while the reported symmetry of ferromagnetic insulating high T_C Sr_3OsO_6 is cubic. This gives a hint that crystal symmetry plays an important role in determining the magnetism.

The presence of $5d$ transition metal, Os in the compound is expected to bring the interplay of spin-orbit coupling (λ) and on-site Coulomb repulsion U along with Hund's coupling parameter J_H within the Os t_{2g} multiorbital framework.

Being curious to reveal the interplay of crystal symmetry, Coulomb repulsion, Hund's coupling and spin-orbit coupling, we carried out first-principles density functional theory based calculations constructing a low-energy model Hamiltonian in Os t_{2g} Wannier basis. We also performed exact diagonalization technique on the two Os site full multiplet with realistic parameter in order to explore the parameter space.

Our study established the stabilization of ferromagnetism in cubic symmetry with high range of U and J_H, accompanied by the large Os-Os nearest neighbour hopping across the face of the cube while in the monoclinic symmetry, suppression of nearest neighbour hopping in distorted cube was found to stabilize antiferromagnetism instead of ferromagnetism. Our electronic stucture calculation revealed insulating behaviour in cubic symmetry by forming spin-orbit entangled Mott state in $j = 3/2$ sector of Os d^2, giving rise to high T_C value. Our study thus showed that for the reported stabilization of ferromagnetism in cubic symmetry of Sr_3OsO_6 is crucial as it is not a natural choice. This highlights the role of epitaxial growth on thin-film behind its unusual ferromagnetic state.

Our study also proposed Sr_2CaOsO_6 [24] as an alternative natural candidate to exhibit high T_C ferromagnetic insulating state in bulk form.

4.2 Computational details

We carried out first-principles density functional theory (DFT) based calculations to achieve a realistic description of the problem. We used two different basis

sets, namely (i) the plane-wave basis [25] and (ii) the muffin-tin orbital basis [26]. Through the calculated density of states and band structures the agreement between these two mentioned basis sets were checked. The structural optimization as well as the effect of spin-orbit coupling and on-site correlation U on the electronic structure were investigated using the plane-wave pseudopotential method as implemented within the Vienna Ab-initio simulation package (VASP) [27]. The wave functions in the plane-wave basis were expanded with a kinetic-energy cutoff of 650 eV. For self-consistent calculations with a plane-wave basis, we chose the k-point meshes as 6×6×6 for both the cubic and triclinic structure, and 6×6×4 for the monoclinic structure. The convergence of the results in terms of the choices of the k-mesh was also checked by repeating calculations with k-mesh of 12×12×12 for cubic and triclinic structure and 12×12×8 for the monoclinic structure. The calculations with larger k-points were found to effect to the results only marginally, with a maximum change in magnetic moment by 0.001 μ_B and energy difference by 0.75 meV. We chose the exchange-correlation functional of the generalized gradient approximation (GGA) [28] within Perdew-Burke-Ernzerhof (PBE) [29] framework. The effect of spin-orbit coupling (SOC) was taken into account within GGA+SOC implementation of VASP. The missing correlation effect beyond GGA at the Os site was considered within the GGA+SOC+U framework [30] by varying the screened Hubbard U value 2-4 eV and fixing Hund's coupling parameter J_H at 0.6 eV, with the choice of the fully localized limit (FLL) of double-counting, as implemented in VASP.

A literature search on the value of Hubbard U in Os oxides and compounds showed it to vary from about 2 eV [31, 32] to about 3.5 eV [33].

The optimization calculations were executed until all the forces on the atoms become smaller than 10^{-5} eV/Å.

For the construction of effective Os t_{2g} based Wannier functions, we used the N^{th}-order muffin-tin orbital (MTO) method [34], which relies on a self-consistent potential generated by the linear MTO (LMTO) [35] method. The low-energy few band Hamiltonian defined by Os t_{2g} Wannier functions provided the on-site energies i.e. the crystal field splitting of the Os sites as well as the effective hopping interactions between the Os sites. Plugging these information of hopping as input, exact diagonalization technique was executed with two-site Os problem.

The different muffin-tin radii for different atomic sites used in our LMTO calculations were as, 2.36 Å (2.05/1.90 Å) for Sr_A, 1.71 Å (1.99/1.80 Å) for Sr_B, 1.25 Å (1.44/1.39 Å) for Os, and 0.87 Å (0.81/0.93 Å, 0.90/0.93 Å, 0.84/0.93 Å) for O atoms in the cubic (monoclinic/triclinic) structure of Sr_3OsO_6.

4.3 Results

4.3.1 Crystal structure of Sr_3OsO_6

The crystal structure of ideal rock-salt ordered double perovskites is cubic with *Fm-3m* space group, which is the reported [18] crystal structure of Sr_3OsO_6 showing unusual ferromagnetic insulating state with high T_C.

Tilt and rotation of BO_6 and $B'O_6$ octahedra, governed by Goldschimidt's tolerance factor (t_R) leads to lower symmetry non-cubic structures. The tolerance factor is defined as $t_R = \frac{(r_A + r_O)}{\sqrt{2}(\frac{r_B + r'_B}{2} + r_O)}$, where r_A, r_B, r'_B, r_O denote the ionic radii of A, B, B′ and O respectively.

Double perovskites are reported with different non-cubic structures e.g. rhombohedral *R-3*, tetragonal *I4/m*, tetragonal *I4/mmm*, monoclinic *P2₁/n*, monoclinic *C2/m*. Along with these mentioned non-cubic space groups, rare examples of tetragonal *P4/mn* and triclinic *P-1* are also reported [2]. Depending upon the tolerance factor, the crystal structure of double perovskite is determined. Smaller t_R value ≈ 0.92 or less suggests to have monoclinic symmetry. In contrary, larger tolerance factors (> 0.92) suggest to have either cubic or tetragonal or rhombohedral symmetry.

Analysing the ionic radii of Sr^{2+}, Os^{6+} and O^{2-}, the t_R value for Sr_3OsO_6, turns out to be 0.89 which is similar to that of monoclinic Ca_3OsO_6. This indicates to the high possibility of forming a non-cubic structure of Sr_3OsO_6, grown through solid-state reaction contradicting the reported cubic symmetry of it.

To clarify the issue concerning the crystal structure of Sr_3OsO_6, we employed a genetic algorithm as implemented in Universal Structure Predictor: Evolutionary Xtallography (USPEX) [36] which has been proved successful in predicting the crystal structure of different multinary compounds, including double perovskites [37, 38] in accurate manner.

The computed energies through our DFT calculations served as a goodness parameter in the applied genetic algorithm and comparison of energies was made among a large number of competitive structures over a number of generations. Following different variational operations e.g. heredity, mutation, permutation, different structures in each generation are produced randomly. Application of this genetic algorithm on Sr_3OsO_6 resulted in monoclinic *P2₁/n* and triclinic *P-1* as its probable structures supporting a recent high-pressure synthesis [39] of Sr_3OsO_6 in powder form which also suggests monoclinic and triclinic structures as the probable structures for Sr_3OsO_6.

We thoroughly checked this structural issue by carrying out total energy vs. volume calculation in GGA+SOC+U scheme considering the reported [18] cubic structure of Sr_3OsO_6 thin film along with genetic algorithm screened structures,

monoclinic $P2_1/n$ and triclinic *P-1*.

Our study showed that the reported cubic symmetry has the highest energy and the energetics of triclinic and monoclinic are almost same as shown in Fig. 4.1. Although the monoclinic symmetry was found to have lower energy than

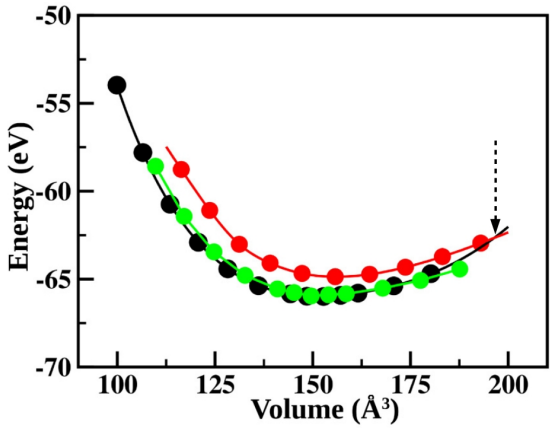

Figure 4.1: Comparison of total energy vs. volume calculated within GGA+SOC+U for Sr_3OsO_6 in cubic (red), monoclinic (black), and triclinic (green) symmetry. The point of crossover between cubic and monoclinic structures is indicated with the dashed arrow.

that of the triclinic one by ≈ 30 meV/f.u. at the equilibrium volume. Reported cubic structure had a large energy difference of 1.1 eV/f.u. from the lowest energy monoclinic structure at the equilibrium volume.

Our calculation showed that ≈ 6.5% tensile strain is required to make a crossover between lowest-energy monoclinic and highest-energy cubic symmetry which appears to be impractical to achieve. This contradicts the reported [18] stabilization of Sr_3OsO_6 in cubic symmetry.

Our study thus concluded that monoclinic symmetry is the most preferred symmetry for Sr_3OsO_6 however its reported stabilization in cubic symmetry only occurs due to its epitaxial growth on $SrTiO_3$ substrate.

In the following we carried out our calculations on the lowest energy monoclinic structure and the reported cubic structure of Sr_3OsO_6 to investigate the role of crystal symmetry on its magnetic properties.

4.3.2 NMTO downfolding and superexchange paths

In Sr_3OsO_6, Os is in nominal valence of 6+ i.e. it has d^2 occupancy. In the cubic symmetry the octahedral crystal field of Os atom splits the Os $5d^2$ levels into lower lying t_{2g} and upper lying e_g states. Due to d^2 occupancy, out of three degenerate t_{2g} levels, two are occupied and one remains empty. The upper lying

empty e_g levels are separated from the t_{2g} levels by a large energy difference $\approx$ 3-4 eV suppressing any hopping interaction involving e_g levels. The degenerate t_{2g} levels are further split into non-degenerate energy levels in non-cubic monoclinic structure.

Thus spitting of the d levels gives rise to virtual hopping procedures. Virtual hopping between half-filled t_{2g} orbitals of neighbouring Os sites drives antiferromagnetic coupling while ferromagnetic coupling is associated with the virtual hopping between half-filled and empty t_{2g} orbitals of two Os sites. Thus the resultant exchange interaction is determined by the competition between the antiferromagnetic and ferromagnetic exchange interactions.

Estimation of strengths of these two competitive interactions quantitatively, necessitates the construction of a low-energy Os t_{2g} Hamiltonian. We applied NMTO downfolding method to obtain this low-energy few band model Hamiltonian, defined by the effective Os t_{2g} Wannier functions by integrating out all the degrees of freedom of Sr, Os e_g and O p. The result showed that while the head part of Os t_{2g} effective Wannier function is shaped following the t_{2g} symmetry, their tail part is shaped according to the integrated out orbitals.

To uncover the role of crystal symmetry of Sr_3OsO_6 on magnetism, we constructed low-energy Os t_{2g} based Hamiltonian for both the reported cubic and theoretically predicted most stable monoclinic structure. In Figs. 4.2 (a), 4.2 (b) the crystal structures of Sr_3OsO_6 in cubic and monoclinic symmetry are shown with corner linked network of OsO_6 and Sr_BO_6 octahedra where the Sr_A atoms occupy the void created by neighbouring OsO_6 and SrO_6 octahedra. In the non-cubic monoclinic structure the OsO_6 and Sr_BO_6 octahedra experience in-plane rotation and out-plane tilt for which the face-centered-cubic (fcc) lattice formed by Os only sublattice in cubic structure becomes distorted in the monoclinic structure. Thus due to structural distortion in monoclinic symmetry, the Os-O-Os angle across the face of the cube deviates from ideal 90° and the Os-O-Sr angle along the edge of the cube deviates from ideal 180°. The deviation range of these two angles in monoclinic symmetry are about 2°-5° and 30°-40° respectively.

The two possible Os-Os hopping paths, nearest-neighbour (t) along the face of the cube and next-nearest neighbour (t') along the edge of the cube, are shown in Figs. 4.2 (c) and 4.2 (d) for cubic and monoclinic symmetry respectively. According to conventional wisdom it is expected that hopping procedure t involving 90° or near 90° in Os-O-Os path is either zero or very weak. Hopping procedure t' through a linear path or nearly linear path Os-O-Sr_B-O-Os involving non-magnetic Sr is also expected to be weak. This conventional knowledge thus makes the high T_C ferromagnetic insulator Sr_3OsO_6 more puzzling.

The overlap plots of Os t_{2g} derived Wannier functions for nearest neighbour and next-nearest neighbour in cubic and monoclinic stucture show a remarkable trend. For the ideal cubic structure in Fig. 4.2 (e), the O p like tails of the Os t_{2g} Wannier functions bend strongly toward the A site Sr atom making a well-defined

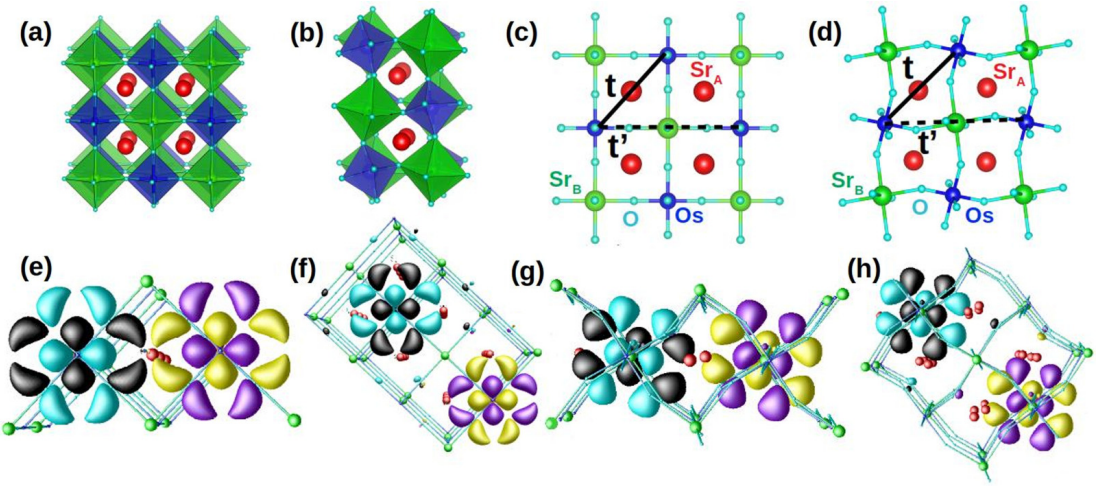

Figure 4.2: (a) The cubic and (b) distorted monoclinic structures of Sr_3OsO_6. The A site Sr atoms (Sr_A) are marked as red balls. The Sr_BO_6 and OsO_6 octahedra are marked in blue and green respectively. (c), (d) The nearest neighbour (t) and next-nearest neighbour (t') Os-Os hopping paths across the face and edge of the cube and the distorted cube in cubic and monoclinic symmetry respectively. (e), (f) Os effective t_{2g} Wannier function overlaps for nearest neighbour and next-nearest neighbour Os sites for the cubic symmetry. Oppositely signed lobes of the Wannier functions are coloured differently (cyan/black for site 1 and magenta/yellow for site 2). (g), (h) show the same as in (e), (f) but for the monoclinic symmetry.

connected path between two Os sites across the face of the cube which is mediated through the t hopping. In Fig. 4.2 (g) for the monoclinic structure, the Wannier functions get misaligned due to the structural deviation from ideal 90° weakening the connected path between Os sites across the face. Due to the bending of O p like tail, we have hardly any overlap for the next-nearest neighbours mediated by t' hopping path as shown in Figs. 4.2 (f) and 4.2 (h) for cubic and monoclinic structures respectively.

The observed trend in Wannier overlap plots is also reflected in the 3×3 tight-binding Hamiltonian defined by Os t_{2g} effective Wannier basis through NMTO downfolding method. The non-cubic crystal-field splitting of the range of 0.07-0.10 eV in monoclinic symmetry lifts the degeneracy of t_{2g} levels. The nearest-neighbour hopping interaction t in the cubic symmetry has the maximum strength of 0.17 eV while that in the monoclinic symmetry takes the value of 0.05 eV being largely suppressed. Thus the hopping strengths derived from the low-energy tight-binding Hamiltonian agrees well with the Wannier function overlap plots. The next-nearest neighbour hopping integral t' is found to be significantly smaller than t comparing their maximum strength values both for cubic and monoclinic structures. The largest strength of t' is $\approx$ 0.01 eV for the cubic symmetry, and

that becomes negligibly small in the monoclinic symmetry.

Next in the exact-diagonalization technique we used these hopping informations considering only the effect of t and discarding the effect of small hopping t'.

4.3.3 Two-site model and magnetic phase diagram

Here we used the knowledge of Wannier function overlaps and the low-energy tight-binding Hamiltonian, derived through DFT calculations to explore the interplay of hopping interaction (t), crystal-field splitting (Δ), Coulomb interaction (U), Hund's exchange (J_H), and spin-orbit coupling (λ) for both cubic and monoclinic structures by employing many-body multiplet calculations within a two-site Os problem.

The two-site Os t_{2g} only model Hamiltonian considering the effect of nearest neighbour hopping, Coulomb interaction, and spin-orbit coupling takes the form as follows [40–42],

$$H = H_{on-site} + H_{int} + H_{SO} + H_t \tag{4.1}$$

The explicit expression of each of the terms are given below,

$$\begin{aligned}
H_{on-site} &= \sum_i \sum_{l,m} \Delta^i_{l,m} d^\dagger_{i,l\sigma} d_{i,m\sigma} \\
H_{int} &= U \sum_i \sum_l n_{i,l\uparrow} n_{i,l\downarrow} + \frac{(U' - J_H)}{2} \sum_i \sum_{\substack{l,m \\ l\neq m}} n_{i,l\sigma} n_{i,m\sigma} \\
&+ \frac{U'}{2} \sum_i \sum_{\substack{l,m \\ l\neq m \\ \sigma\neq\sigma'}} n_{i,l\sigma} n_{i,m\sigma'} \\
&- \frac{J_H}{2} \sum_i \sum_{\substack{l,m \\ l\neq m}} (d^\dagger_{i,m\uparrow} d_{i,m\downarrow} d^\dagger_{i,l\downarrow} d_{i,l\uparrow} + d^\dagger_{i,m\uparrow} d^\dagger_{i,m\downarrow} d_{i,l\uparrow} d_{i,l\downarrow} + H.c.) \\
H_{SO} &= \frac{i\lambda}{2} \sum_i \sum_{\substack{l,m,n \\ \sigma,\sigma'}} \epsilon_{lmn} d^\dagger_{i,l\sigma} d_{i,m\sigma'} \sigma^n_{\sigma,\sigma'} \\
H_t &= \sum_{\substack{l,m,\sigma \\ \langle i,j\rangle}} t^{ij}_{lm} (d^\dagger_{i,l\sigma} d_{j,m\sigma} + H.c.)
\end{aligned} \tag{4.2}$$

where, $d^\dagger_{i,l\sigma}(d_{i,l\sigma})$ is the creation (annihilation) operator of the l^{th} orbital at site i with spin σ. $n_{i,l\sigma}$ is defined as, $n_{i,l\sigma} = d^\dagger_{i,l\sigma} d_{i,l\sigma}$. $H_{on-site}$ represents the on-site crystal field splitting with on-site matrix element $\Delta_{l,m}$ between l and m orbital

at the same site i. H_{int} contains intra-orbital Coulomb correlation (U), Hund's coupling (J_H) and inter-orbital Coulomb correlation (U'). Inter-orbital Coulomb interaction satisfies the Kanamori relation, $U' = U - 2J_H$. In H_{SO}, λ is the spin-orbit coupling strength and ϵ_{lmn} is the three dimensional leve-civita symbol. H_t contains t_{lm}^{ij}, the nearest neighbour hopping parameter between l^{th} orbital of site i and m^{th} orbital of site j.

We took the realistic values of the non-cubic crystal field and the intersite hopping parameters as obtained through NMTO downfolding calculations by varying the U and J_H parameters over a physically meaningful range, $U' > J_H$ keeping the λ values fixed at 0.1, 0.2, and 0.4 eV.

Using the exact-diagonalization technique on this two-site Os problem [43], the energy differences between parallel (ferromagnetic) and antiparallel (antiferromagnetic) spin arrangement of Os spins were studied. In Figs. 4.3 (a) and 4.3 (b) the energy differences with the choice of $U = 2$ eV and $\lambda = 0.1$ eV varying J_H are plotted for cubic and monoclinic structures respectively. Thus analysing Fig. 4.3, it is evident that in the cubic symmetry the parallel alignment of Os spin i.e. ferromagnetic (FM) interaction becomes favoured over antiferromagnetic (AFM) interaction for $J_H > 0.27$ eV or so while that for the monoclinic structure the ferromagnetic interaction becomes stabilized over antiferromagnetic interaction only when $J_H > 0.6$ eV. Thus we can argue that for $5d$ transition metal Os, with a reasonable choice of $J_H = 0.6$ eV, FM interaction is stabilized for cubic symmetry, and AFM interaction is stabilized for monoclinic symmetry.

Looking at the energy gain values at $J_H = 0.6$ eV, it is clear that the energy gain is larger in cubic (≈ 30 meV) than that for the monoclinic (≈ 1.5 meV) structure. Now putting these energy gain values in the mean-field temperature scale, $\frac{zJS^2}{3}$ (z = number of nearest neighbours, here it is 12), we obtained the T_C value above 1300 K for cubic stucture and that for the monoclinic structure became ~ 70 K.

Thus our calculation showed that FM state supports a large T_C and AFM state supports a low transition temperature, which is in good agreement with the reported cubic structured Sr_3OsO_6 [18] and monoclinic structured Ca_3OsO_6 [23].

We repeated the same calculation by varying the U and J_H parameters with higher λ values 0.2 eV and 0.4 eV to obtain the U-J_H phase space and the results are shown in Figs. 4.3 (c), 4.3 (d) for cubic and monoclinic structure respectively. Though the two phase diagrams look qualitatively the same, increase of the λ value shifts AFM to FM transition to a larger value of J_H as spin-orbit coupling favours antiferromagnetism. Our calculations showed that both for the λ values, the FM interaction is stabilized only in a shrunk part of the U-J_H phase space in monoclinic structure while an appreciable part of U-J_H phase space supports FM interaction in cubic structure.

Thus in summary our study showed that the ferromagnetic phase is stabilized

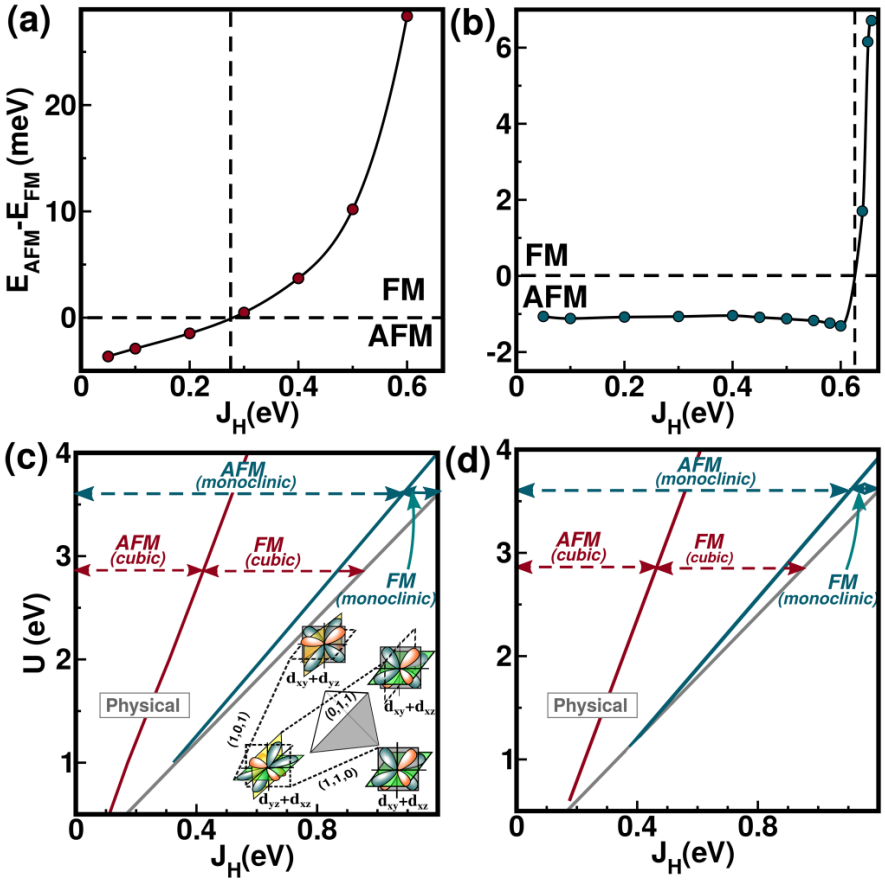

Figure 4.3: Energy difference between parallel and antiparallel alignment of Os spins as a function of varying Hund's coupling parameter J_H keeping $U = 2$ eV and $\lambda = 0.1$ eV and considering the DFT derived hopping interaction in (a) cubic symmetry and (b) monoclinic symmetry of Sr_3OsO_6. (c) U-J_H phase diagram in cubic and monoclinic symmetry showing the stabilization of ferro and antiferro Os spin alignment for $\lambda = 0.2$ eV. The inset shows the ordering of Os t_{2g} orbitals with d^2 occupancy reversing between d_{xy}/d_{xz}, d_{yz}/d_{xz}, d_{xy}/d_{yz}, and d_{xy}/d_{xz} along the connecting vectors of Os fcc tetrahedra. (d) U-J_H phase diagram for $\lambda = 0.4$ eV. The gray solid line in (c) and (d) separates the physically relevant space, $U' = U - 2J_H > J_H$.

in the cubic structure of Sr_3OsO_6 with a rather high temperature scale, while the monoclinic structure favours the antiferromagnetic interaction with a low transition temperature.

The fcc lattice made up of Os only sublattice can give rise to spin-glass-like behaviour in compound specific cases as the antiferromagnetic arrangement of Os spins becomes frustrated in the fcc motif.

We repeated our calculation to obtain the U-J_H phase space for the triclinic symmetry which is one of the suggested structures of bulk Sr_3OsO_6 in Ref. [39]

and the next favoured structure predicted from our theoretical calculations. For all choices of λ, the phase diagram of triclinic symmetry is found to favour antiferromagnetic interaction solely, disfavouring the ferromagnetic interaction even more than that of the monoclinic symmetry. This agrees completely with the stabilization of antiferromagnetism over ferromagnetism in the reported study of Ref. [39] for bulk Sr_3OsO_6.

The inset of Fig. 4.3 (c) shows the orbital ordering of two occupied orbitals between the four sites of Os fcc tetrahedra in the stabilized ferromagnetic phase involving the hopping between occupied and empty t_{2g} orbitals. Two Os sites connected through (1,1,0) vector have electron occupancy mostly at d_{xz}/d_{yz} and d_{xz}/d_{xy} orbitals. Thus this encourages the hopping between filled and empty d_{xy} orbitals. Similarly, for the sites connected through (1,0,1) and (0,1,1) vectors, the ferromagnetic hopping is favoured between filled to empty d_{xz} and d_{yz} orbitals respectively.

4.3.4 Insulating electronic structure

Here aiming to explore the origin of the insulating behaviour of ferromagnetic cubic Sr_3OsO_6, we performed stepwise calculations within the framework of GGA, GGA+SOC, and GGA+SOC+U considering various influencing factors which drive the insulating state.

For Os^{6+} ions in ideal cubic environment with d^2 occupancy, GGA calculation gave a metallic solution [cf. top panel of Fig. 4.4 (a)] with a magnetic moment of 1.10 μ_B at the Os site, and 0.05 μ_B at the O site due to finite Os-O covalency. A significant orbital moment of 0.17 μ_B at the Os site, oppositely aligned to the spin moment of 0.62 μ_B at the Os site was developed turning on the spin-orbit coupling within GGA+SOC framework. This antiparallel alignment of orbital and spin moment confirms the less than half-filled nature of Os^{6+}.

The calculated band structures are also presented in Fig. 4.4 (b) in the framework of GGA, GGA+SOC and GGA+SOC+U. Being consistent with the density of states structure, the band structure also showed that inclusion of SOC keeps the solution metallic with Os states crossing the Fermi level as SOC mixes the up and down spin channels of t_{2g}'s which act like effective $l = 1$ quantum number states. These states are described by fourfold-degenerate $j = 3/2$ and twofold-degenerate $j = 1/2$ states in presence of SOC. Due to d^2 occupancy of Os, the $j = 3/2$ states become half-filled which becomes similar to a d^5 iridate e.g. Sr_2IrO_4 [44].

Inclusion of correlation U in GGA+SOC+U framework opened up a gap within $j = 3/2$ manifold for the choice of U value ≥ 2 eV. The 4 f.u. cubic cell gives 24 t_{2g} bands of Os. Within the GGA+SOC+U framework, out of these 24 bands, 8 lie below the Fermi level, forming $j = 3/2$ lower Hubbard bands (LHB) and the remaining 16 lie above the Fermi level being separated by a gap from $j = 3/2$ LHB states as shown in Fig. 4.4 (b). The 8 empty $j = 3/2$ upper

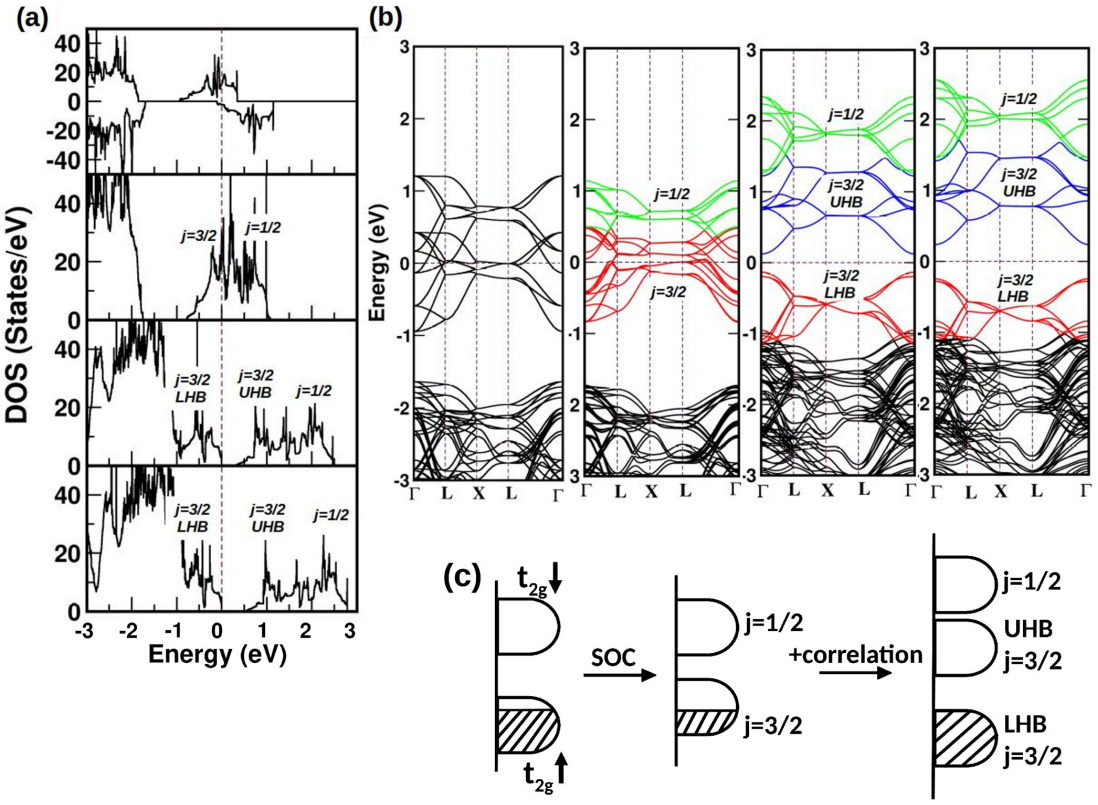

Figure 4.4: Electronic structure calculation of cubic Sr_3OsO_6. (a) Density of states computed within spin-polarized GGA, GGA+SOC, GGA+SOC+U (U = 2 eV) and GGA+SOC+U (U = 3 eV) (top to bottom) framework. The spin-orbit coupled $j = 3/2$ and 1/2 manifolds are marked. In the presence of U correlation effect, $j = 3/2$ manifold develops into $j = 3/2$ LHB and $j = 3/2$ UHB. (b) The band structures are plotted along high symmetry points of the fcc BZ, within GGA, GGA+SOC, GGA+SOC+U for U = 2 eV and 3 eV (left to right). Only the bands of the majority spin channel for spin-polarized GGA band structure are shown. Bands corresponding to $j = 3/2$ (LHB, UHB) and $j = 1/2$ are coloured differently and marked. The zero of the energy in both the density of states and band structure plots represents the respective Fermi energy. (c) Schematic representation of the systematic effect of turning on SOC and U correlation on Os t_{2g}'s with d^2 occupancy. Filled states are represented as hatched.

Hubbard bands (UHB) overlap with 8 empty $j = 1/2$ bands due to finite bandwidths of $j = 3/2$ and 1/2. The inclusion of the Hubbard U correction increased both the spin and orbital moment of Os and for the choice of U = 2 eV and they took the values as 1.48 μ_B and 0.65 μ_B respectively leading to effective magnetic moment of 0.83 μ_B which is in good agreement with the experimentally measured [18] moment of 0.77 μ_B. The gap value was found to get increased with increasing the U value. The calculated band gap value was found to be 0.33 eV

for $U = 2$ eV, and 0.55 eV for $U = 3$ eV.

Thus our study showed that Sr_3OsO_6 is an example of a spin-orbit entangled Mott state in $j = 3/2$ sector akin to Sr_2IrO_4 in $j = 1/2$ sector.

4.4 Summary

Here our study has been carried out on Os containing double perovskite compound Sr_3OsO_6. We studied the microscopic origin of its reported high-T_C ferromagnetic insulating behaviour in cubic symmetry [18]. Situation became curious as the Ref. [18] reported the crystal structure of Sr_3OsO_6, grown on thin-film to be cubic whereas a recent report [39] of bulk Sr_3OsO_6, synthesized in solid-state route suggests for its non-cubic monoclinic or triclinic symmetry.

We performed our calculations to explore the crystal symmetry of Sr_3OsO_6 in conjunction with the application of a genetic algorithm and first-principles total energy calculations. Our study showed monoclinic symmetry as the most preferred symmetry followed by triclinic symmetry and the cubic symmetry with much higher energy.

Next we explored the role of crystal symmetry on magnetism taking into account the predicted lowest energy monoclinic structure and the reported [18] cubic structure of Sr_3OsO_6. Our Wannier function overlaps defined by Os t_{2g} basis showed large Os-Os hopping across the face of the cubic structure dominating over the conventionally expected Os-O-Sr_B-O-Os superexchange path along the edge of the cubic structure. This well-connected Os-Os path became misaligned in the monoclinic structure due to structural distortion weakening the hopping process.

Using the DFT derived Os t_{2g} low-energy Hamiltonian, defined in the Wannier basis as input, we next solved the two-site Os t_{2g} full multiplet problem with exact diagonalization method to understand the t-U-J_H-λ phase space more accurately. With the reasonable choice of λ value for Os, the U-J_H phase space showed the stabilization of ferro alignment of Os spins in cubic symmetry. On the other hand, the ferro alignment was found to be largely suppressed in monoclinic symmetry. The stabilization energy of ferro alignment over antiferro alignment in the cubic symmetry was found to be more than an order of magnitude larger compared to the stabilization energy of antiferro alignment of Os spins over ferro in the distorted monoclinic symmetry for the same parameter values of U, J_H, and λ, supporting the observed high T_C in the reported cubic, ferromagnetic phase of Sr_3OsO_6 [18] and the low Neél temperature in the reported monoclinic, AFM phase of Ca_3OsO_6 [23].

Following this understanding, we next investigated the driving force behind the insulating nature of ferromagnetic Sr_3OsO_6 through systematic analysis in GGA, GGA+SOC and GGA+SOC+U framework of electronic structure calcu-

lations. Our electronic structure calculation gave metallic solution for GGA and GGA+SOC scheme whereas an insulating ground state was achieved only within the framework of GGA+SOC+U with reasonable choices of U values. Thus inclusion of correlation U was found to give insulating state in cubic Sr_3OsO_6 in $j = 3/2$ Mott state induced by large spin-orbit coupling at the Os site.

Bibliography

[1] D. D. Sarma, Curr. Opin. Solid State Mater. Sci. **5**, 261 (2001).

[2] S. Vasala and M. Karppinen, Prog. Solid State Chem. **43**, 1 (2015).

[3] T. Saha-Dasgupta, J. Supercond. Nov. Magn. **26**, 1991 (2013).

[4] T. Saitoh, M. Nakatake, A. Kakizaki, H. Nakajima, O. Morimoto, Sh. Xu, Y. Moritomo, N. Hamada, and Y. Aiura, Phys. Rev. B **66**, 035112 (2002).

[5] A. A. Aczel, Z. Zhao, S. Calder, D. T. Adroja, P. J. Baker, and J.-Q. Yan, Phys. Rev. B **93**, 214407 (2016).

[6] Y. Tomioka, T. Okuda, Y. Okimoto, R. Kumai, K.-I. Kobayashi, and Y. Tokura, Phys. Rev. B **61**, 422 (2000).

[7] P. Sanyal, H. Das, and T. Saha-Dasgupta, Phys. Rev. B **80**, 224412 (2009).

[8] T. K. Mandal, C. Felser, M. Greenblatt, and J. Kubler, Phys. Rev. B **78**, 134431 (2008).

[9] P. Sanyal, A. Halder, L. Si, M. Wallerberger, K. Held, and T. Saha-Dasgupta, Phys. Rev. B **94**, 035132 (2016).

[10] J. B. Philipp, P. Majewski, L. Alff, A. Erb, R. Gross, T. Graf, M. S. Brandt, J. Simon, T. Walther, W. Mader, D. Topwal, and D. D. Sarma, Phys. Rev. B **68**, 144431 (2003).

[11] H. Das, P. Sanyal, T. Saha-Dasgupta, and D. D. Sarma, Phys. Rev. B **83**, 104418 (2011).

[12] J. M. De Teresa, D. Serrate, C. Ritter, J. Blasco, M. R. Ibarra, L. Morellon, and W. Tokarz, Phys. Rev. B **71**, 092408 (2005).

[13] H. L. Feng, M. P. Ghimire, Z. Hu, S.-C. Liao, S. Agrestini, J. Chen, Y. Yuan, Y. Matsushita, Y. Tsujimoto, Y. Katsuya, M. Tanaka, H.-J. Lin, C.-T. Chen, S.-C. Weng, M. Valvidares, K. Chen, F. Baudelet, A. Tanaka, M. Greenblatt, L. H. Tjeng, and K. Yamaura, Phys. Rev. Mater. **3**, 124404 (2019).

[14] H. L. Feng, S. Calder, M. P. Ghimire, Y.-H. Yuan, Y. Shirako, Y. Tsujimoto, Y. Matsushita, Z. Hu, C.-Y. Kuo, L. H. Tjeng, T.-W. Pi, Y.-L. Soo, J. He, M. Tanaka, Y. Katsuya, M. Richter, and K. Yamaura, Phys. Rev. B **94**, 235158 (2016).

[15] C. M. Thompson, J. P. Carlo, R. Flacau, T. Aharen, I. A. Leahy, J. R. Pollichemi, T. J. S. Munsie, T. Medina, G. M. Luke, J. Munevar, S. Cheung, T. Goko, Y. J. Uemura, and J. E. Greedan, J. Phys. Condens. Matter **26**, 306003 (2014).

[16] Y. Yuan, H. L. Feng, M. P. Ghimire, Y. Matsushita, Y. Tsujimoto, J. He, M. Tanaka, Y. Katsuya, and K. Yamaura, Inorg. Chem. **54**, 3422 (2015).

[17] R. Morrow, A. E. Taylor, D. J. Singh, J. Xiong, S. Rodan, A. U. B. Wolter, S. Wurmehl, B. Bchner, M. B. Stone, A. I. Kolesnikov, A. A. Aczel, A. D. Christianson, and P. M. Woodward, Sci. Rep. **6**, 32462 (2016).

[18] Y. K. Wakabayashi, Y. Krockenberger, N. Tsujimoto, T. Boykin, S. Tsuneyuki, Y. Taniyasu, and H. Yamamoto, Nat. Commun. **10**, 535 (2019).

[19] B. T. Matthias, R. M. Bozorth, and J. H. Van Vleck, Phys. Rev. Lett. **7**, 160 (1961).

[20] P. K. Baltzer, H. W. Lehmann, and M. Robbins, Phys. Rev. Lett. **15**, 493 (1965).

[21] M. A. Subramanian, A. P. Ramirez, and W. J. Marshall, Phys. Rev. Lett. **82**, 1558 (1999).

[22] H. Das, U. V. Waghmare, T. Saha-Dasgupta, and D. D. Sarma, Phys. Rev. Lett. **100**, 186402 (2008).

[23] H. L. Feng, Y. Shi, Y. Guo, J. Li, A. Sato, Y. Sun, X. Wang, S. Yu, C. I. Sathish, and K. Yamaura, J. Solid State Chem. **201**, 186 (2013).

[24] J. H. Choy, D. K. Kim, and J. Y. Kim, Solid State Ion. **108**, 159 (1998).

[25] V. Heine, Solid State Phys. **24**, 1 (1970).

[26] O. K. Andersen, Phys. Rev. B **12**, 3060 (1975).

[27] G. Kresse and J. Hafner, Phys. Rev. B **47**, 558(R) (1993); G. Kresse and J. Furthmüller, ibid. **54**, 11169 (1996).

[28] J. P. Perdew, J. A. Chevary, S. H. Vosko, K. A. Jackson, M. R. Pederson, D. J. Singh, and C. Fiolhais, Phys. Rev. B **48**, 4978(E) (1993).

[29] J. P. Perdew, K. Burke, and M. Ernzerhof, Phys. Rev. Lett. **77**, 3865 (1996).

[30] A. I. Liechtenstein, V. I. Anisimov, and J. Zaanen, Phys. Rev. B **52**, R5467 (1995).

[31] G. Lana, J. Song, and Z. Yang, J. Alloy Compd. **749**, 909 (2018).

[32] A. Neroni, E. Sasloglu, H. Hadipour, C. Friedrich, S. Blügel, I. Mertig, and M. Lezaic, Phys. Rev. B **100**, 115113 (2019).

[33] E. Şaşoğlu, C. Friedrich, and S. Blügel, Phys. Rev. B **83**, 121101(R) (2011).

[34] O. K. Andersen and T. Saha-Dasgupta, Phys. Rev. B **62**, R16219 (2000).

[35] O. K. Andersen and O. Jepsen, Phys. Rev. Lett. **53**, 2571 (1984).

[36] A. R. Oganov and C. W. Glass, J. Chem. Phys. **124**, 244704 (2006); A. O. Lyakhov, A. R. Oganov, and M. Valle, in Modern Methods of Crystal Structure Prediction, edited by A. R. Oganov (Wiley-VCH, Weinheim, Germany, 2012), pp. 147-180; A. R. Oganov and C. W. Glass, J. Phys. Condens. Matter **20**, 064210 (2008).

[37] A. Halder, D. Nafday, P. Sanyal, and T. Saha-Dasgupta, npj Quantum Mater. **3**, 17 (2018).

[38] A. Halder, A. Ghosh, and T. S. Dasgupta, Phys. Rev. Mater. **3**, 084418 (2019).

[39] J. Chen, H. L. Feng, Y. Matsushita, A. A. Belik, Y. Tsujimoto, M. Tanaka, D. Y. Chung, and K. Yamaura, Inorg. Chem. **59**, 4049 (2020).

[40] H. Matsuura and K. Miyake, J. Phys. Soc. Jpn. **82**, 073703 (2013).

[41] A. Chakraborty and I. Dasgupta, J. Magn. Magn. Mater. **492**, 165708 (2019).

[42] A. Nag, S. Bhowal, A. Chakraborty, M. M. Sala, A. Efimenko, F. Bert, P. K. Biswas, A. D. Hillier, M. Itoh, S. D. Kaushik, V. Siruguri, C. Meneghini, I. Dasgupta, and S. Ray, Phys. Rev. B **98**, 014431 (2018).

[43] H. Meskine, H. Konig, and S. Satpathy, Phys. Rev. B **64**, 094433 (2001).

[44] B. J. Kim, H. Jin, S. J. Moon, J.-Y. Kim, B.-G. Park, C. S. Leem, J. Yu, T. W. Noh, C. Kim, S.-J. Oh, J.-H. Park, V. Durairaj, G. Cao, and E. Rotenberg, Phys. Rev. Lett. **101**, 076402 (2008).

Chapter 5

Understanding Magnetism in Double Double Perovskites: A Complex Multiple Magnetic Sublattice System*

5.1 Motivation

Transition metal oxides crystallizing in perovskite structure with the chemical formula ABO_3 is a holy grail of condensed matter physics due to their numerous interesting properties like high temperature superconductivity, colossal magnetoresistance, half-metallicity etc. [1, 2].

The structural and compositional flexibility of the structure allow perovskites to accommodate almost all of the elements of periodic table, and also support various possible coordination. One of the common routes to tailor the perovskite properties is cation substitution. Substitution and 1:1 cation ordering at B site give rise to rock-salt ordered double perovskites $A_2BB'O_6$ [3–6], where B and B′ are two transition metal (TM) ions, as discussed in Chapter 4 in context of Sr_3OsO_6.

The magnetism of transition metal oxides crystallizing in double perovskite framework has grabbed significant attention [7–22].

In this scenario it is worthwhile to explore the situation when compounds

*Based on publication: Anita Halder†, **Shreya Das**†, Prabuddha Sanyal, and Tanusri Saha-Dasgupta; †authors have equal contribution to this work; **arXiv:2101.10822**.

involve even larger number of magnetic ions, i.e. more than two TM ions, as in double double perovskites. There are limited reports on cation ordering at A and B sublattices simultaneously. However this cation ordering extends the structural flexibility of perovskites further.

Recently double double perovskites with formula $AA'_{0.5}A''_{0.5}BB'O_6$ have been synthesized using high pressure and temperature condition [23–25] with columnar motif of A sublattice and rock-salt motif of B sublattice. This structure consists of five independent cation sites A, A′, A″, B and B′ where the A site hosts rare-earth or alkaline-earth ion, A′, A″ and B sites host $3d$ transition metal ions and B′ hosts $5d$ transition metal ion. Use of high pressure stabilizes small magnetic TM ions like Mn^{2+} at A sites with reduced coordination of tetrahedral (4) and square planar (4) instead of the usual choice of large nonmagnetic cations like Ca^{2+}, Sr^{2+} with dodecahedral (12) coordination of A site [26]. Stabilization of magnetic TM ion at A site introduces A site magnetism which eventually drives the interplay of magnetism among the multiple sublattices giving rise to highly enriched magnetic properties.

Presence of multiple magnetic ions with multiple magnetic exchanges can lead to a naive expectation of spin-glass like ground state with frustration but in contrary, recently synthesized double double perovskites $CaMnMReO_6$ (M = Ni, Co) are reported to be magnetically ordered [27], exhibiting ferromagnetic ordering in $CaMnNiReO_6$ with parallel spin alignment and ferrimagnetic ordering in $CaMnCoReO_6$, on replacement of Ni by Co.

Reported net moment of such multi sublattice ferromagnetic system is very high which paves the way to design large moment magnetic oxides. The situation becomes curious on the following counts,

(i) what is the underlying reason that makes three or more magnetic sublattice system $CaMnNiReO_6$ ferromagnetic, (ii) why $CaMnCoReO_6$ becomes ferrimagnetic on replacement of Ni by Co, the neighbouring element in periodic table, (iii) what is the driving mechanism of magnetism in such multi sublattice system.

Theoretical understanding of the interplay of magnetism of these multi magnetic sublattices is challenging as well as exciting as it is expected to unravel the rich physics which can be helpful in designing such oxides in future.

Aiming to explore the multi magnetic sublattice systems, we carried out first principles density functional theory (DFT) based calculations taking into account all the chemical and structural aspects accurately. Next we employed DFT derived spin Hamiltonians which were solved with Monte Carlo (MC) simulation.

Our study uncovered the presence of a novel exchange mechanism which is a combination of multi sublattice hybridization i.e. the kinetic energy driven double-exchange mechanism, along with the superexchange mechanism, in these systems. Our study showed that the ground state of these multi sublattice systems is determined by the competition between these two above mentioned exchange

mechanisms. It was revealed through our calculation that in $CaMnNiReO_6$, the multi sublattice hybridization-driven double-exchange mechanism dominates the superexchange mechanism giving rise to long range ferromagnetic state. Replacement of Ni by Co, enhances the core spin value at B sublattice (from S = 1 to S = 3/2) which toggles between the two exchange mechanisms supporting long range ferrimagnetism. The MC simulation on solving the DFT derived spin Hamiltonians, provided good agreement with the reported magnetic properties [27] of both the Ni and Co compounds. The description of the ground states of the respective structures was found to be intact even after the introduction of off-stoichiometry. These high moment multi sublattice systems turned out to exhibit half-metallic character which is important for spintronics applications.

5.2 Methods

We carried out first principles density functional theory based calculations using the plane-wave pseudopotential method as implemented in Vienna Ab-initio Simulation Package (VASP) [28]. We used exchange-correlation functional within the generalized gradient approximation (GGA) [29]. The projector-augmented wave (PAW) potentials [30] were used with the expansion of the wave functions in the plane-wave basis. Kinetic energy cut-off of 600 eV and reciprocal space integration with a k-space mesh of 6×6×6 were found to provide a good convergence. The exchange-correlation beyond GGA was treated in GGA+U approach with Hubbard U and Hund's coupling J_H within the multi-band framework [31]. The double-counting correction was incorporated by using fully localized limit (FLL) of double-counting [32]. The choice of U and J_H values were made to be 5 eV, 0.9 eV for Ni/Co as appropriate for $3d$ TM atoms, and 2 eV, 0.4 eV for Re as appropriate for $5d$ TM atoms respectively [33]. Results found to be unaltered qualitatively by varying the U values over 1-2 eV.

For the construction of a few-band tight-binding (TB) Hamiltonian out of the full DFT calculation, N^{th}-order muffin tin orbital (NMTO) calculations were executed [34]. Starting from a full DFT all band calculation, energy selected few-orbital Hamiltonian, defined by effective Wannier function basis was constructed by integrating out all the degrees of freedom that are not of interest. The NMTO method relies on the self-consistent potential parameters obtained through the linear muffin-tin orbital (LMTO) [35] method calculations.

We employed Monte Carlo simulation on the spin Hamiltonian with a N×N×N finite sized unit cell of Mn and Ni/Co atoms to obtain the magnetization data. Here we used 3×3×3 lattice simulations applying the periodic boundary conditions. The magnetic transition temperatures were estimated from these calculations.

5.3 Results

5.3.1 Crystal structure

Stoichiometric $CaMnNiReO_6$ (CMNRO) has tertragonal unit cell consisting of four formula units and belongs to *P42/n* space group symmetry as shown in Fig. 5.1. Another compound $CaMnCoReO_6$ (CMCRO) is isostructural to $CaMnNiReO_6$.

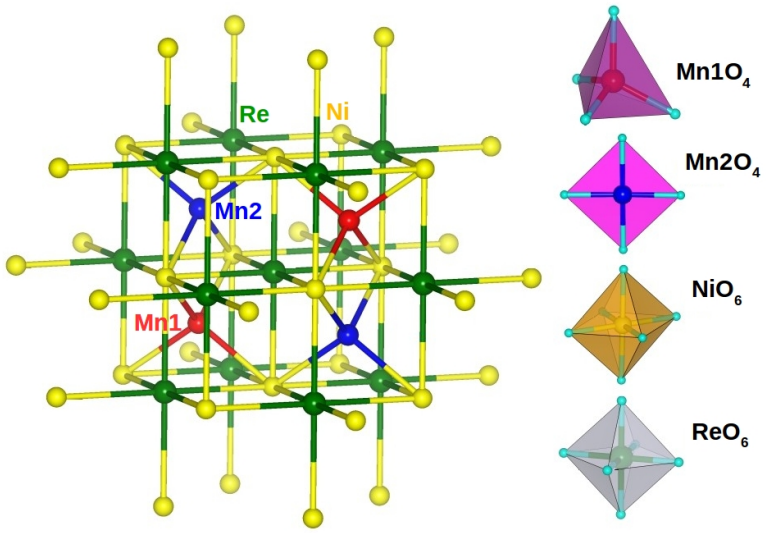

Figure 5.1: Crystal structure of stoichiometric CMNRO compound. CMCRO is isostructural to CMNRO. Left panel shows the three dimensional 3*d*-5*d* network of four magnetic sublattices with Mn at tetrahedral site (Mn1) and at square planar site (Mn2). Red, blue, yellow and green coloured balls represent Mn1, Mn2, Ni and Re atoms respectively. Right panel shows the oxygen coordination of the four magnetic ions: tetrahedral for Mn1, square planar for Mn2, and octahedral for Ni and Re.

The structure makes a 3*d*-5*d* TM magnetic system containing the following four magnetic sublattices,

(i) 3*d* transition metal Mn(Mn1) at A′ site in tetrahedral coordination, (ii) square planar coordinated 3*d* transition metal Mn(Mn2) at A″ site, (iii) 3*d* transition metal Ni/Co at B site in octahedral coordination, and (iv) 5*d* transition metal Re at B′ site in octahedral coordination. Mn1 connects itself to two nearest neighbour (NN) Mn2 sites mediated by Mn1-O-O-Mn2 superexchange paths, while Mn1/Mn2 is connected to 4 NN Ni(Co)/Re via Mn1/Mn2-O-Ni(Co)/Re superexchange paths. Ni(Co) and Re are connected to each other through Ni(Co)-O-Re corner shared path, with a range of bond angles of 141-152°.

5.3.2 Electronic structure

Our electronic structure calculations of these two stoichiometric compounds in terms of spin-polarized density of states (DOS), and its projection to the orbital characters provided the information on charge and spin states of the transition metal ions.

The GGA+U DOS, with $U = 5$ (2) eV and $J_H = 0.9$ (0.4) eV at $3d$ TM (Re) sites, for CMNRO and CMCRO are shown in Fig. 5.2.

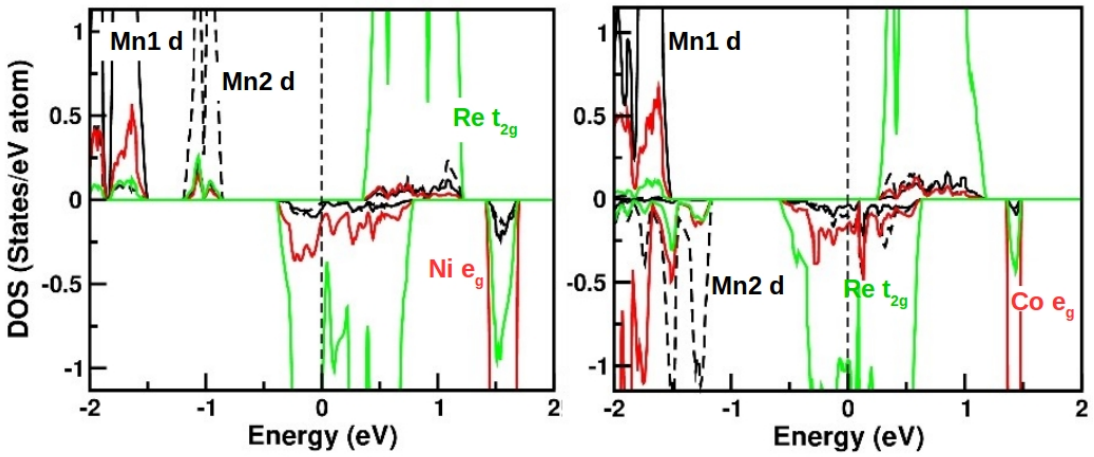

Figure 5.2: The GGA+U density of states of CMNRO (left) and CMCRO (right) projected to Mn1 d (black solid), Mn2 d (black dashed), Ni e_g/Co d (red solid) and Re t_{2g} (green solid) states. Fermi energy is fixed at zero of the energy.

Our calculation showed that the ground state of CMNRO is ferromagnetic, with moments at three $3d$ TM sublattices Mn1, Mn2 and Ni sites aligned in parallel direction, while the moment at Re site is aligned opposite to the moments of Mn1, Mn2 and Ni sites. This result is consistent with the reported experimental findings. The calculated magnetic moments at both the Mn sites (Mn1 and Mn2), Ni and Re were found to be 4.5 μ_B, 1.6 μ_B and 0.5 μ_B respectively, with a large total moment of 24 μ_B in the unit cell with 4 formula units.

For CMCRO our calculation showed that the ground state is ferrimagnetic which is also in good agreement with the observed experimental report. The calculated magnetic moments of Mn1, and Mn2 were found to be aligned in antiparallel direction, and Co moment pointing in the direction of Mn1. The Re moment was found to be antiparallel to Mn1 and Co. The calculated moment values were found to be 4.5 μ_B (Mn1 and Mn2), 2.6 μ_B (Co) and 0.5 μ_B (Re) and total moment of 8 μ_B in the unit cell.

These calculated moments supports the nominal 2+ valence of Mn1 and Mn2 with high spin (HS) d^5 occupancy, 2+ valence of Ni/Co with high spin d^8/d^7

occupancy and 6+ valence of Re with d^1 occupancy.

Analysing the DOS of CMNRO, it was found that Mn1 and Mn2 states are filled in the majority spin channel and empty in the minority spin channel. Ni e_g states in CMNRO are filled in majority spin channel and empty in minority spin channel, while the Ni t_{2g} states are filled in both the spin channels. The Re t_{2g} states in CMNRO are partially filled with one electron in the minority spin channel and strongly hybridized with Mn1/Mn2 d and Ni e_g states. In minority spin channel the density of states crosses the Fermi level making the solution metallic while in the majority spin channel it is gapped.

This half-metallic solution remained intact in CMCRO too. Although in CMCRO the Mn1 and Mn2 d states become filled and empty, respectively in two opposite spin channels. Co t_{2g} states become partly empty indicating the possibility to achieve spin-dependent nature of the carrier scattering in these compounds with a large spin value.

We also checked the effect of spin-orbit coupling (SOC), which was expected to be appreciable for $5d$ TM element, Re. Our calculation showed that the qualitative results are unchanged upon inclusion of SOC, apart from a developed orbital moment of $\sim 0.15\ \mu_B$ at Re site, antiparallel to its spin moment.

5.3.3 Mechanism of magnetism

To explore the driving mechanism of magnetism in these multi magnetic sublattice compounds, we constructed a low-energy spin Hamiltonian using the DFT results as inputs.

In order to do so we performed the muffin-tin orbital based downfolding calculations [34] by integrating out the degrees of freedom which are of no interest, in an energy selective manner.

The downfolded Hamiltonian, defined by Wannier basis, provided us the estimates of the onsite energies and the hopping interactions between the orbitals retained in the basis during the process of downfolding.

The two-step downfolding calculations were executed by following the steps:

(i) In the first step of downfolding calculations, the Mn1, Mn2 d states, Ni e_g/Co d states and Re t_{2g} states were retained in the basis and other degrees of freedom were integrated out.

(ii) In the second step, Mn1, Mn2 and Ni/Co degrees of freedom were downfolded keeping only the Re t_{2g} degrees of freedom in the basis.

The second step of massive downfolding gave the estimates of the Re t_{2g} onsite energies renormalized by the hybridization from Mn1, Mn2 and Ni/Co states.

Thus the onsite matrix elements of the real space Hamiltonian defined in the first and second step of downfolding calculations, provided the energy level positions before and after switching on the hybridization between Mn1/Mn2/Ni(Co)

and Re states, respectively.

The results of two step downfolding calculations for CMNRO and CMCRO are shown in Fig. 5.3. These energy level diagrams show both the crystal field split and exchange split for the Mn1-d, Mn2-d, Ni e_g (Co-d) and Re t_{2g} states.

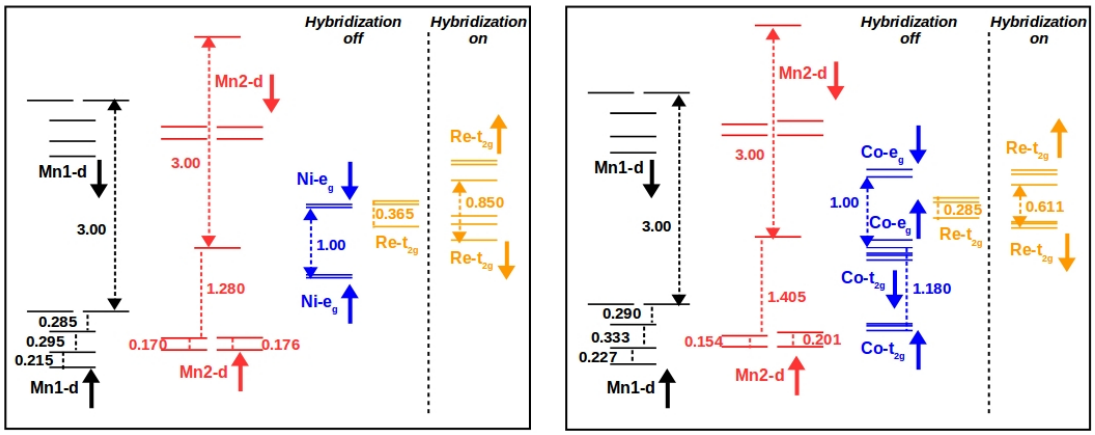

Figure 5.3: The energy level diagram for CMNRO (left) and CMCRO (right) considering Mn1-d/Mn2-d/Ni e_g(Co d)/Re t_{2g} in basis (Hybridization-off) and in the massively downfolded Re t_{2g} only basis (Hybridization-on).

Analysing energy diagram it was found that in distorted tetrahedral coordination, Mn1 d states split into 1-1-1-2 fold degeneracies, while Mn2 d states in square planar coordination split into 2-2-1 fold degeneracies. Re t_{2g} states split into 1-2 fold degeneracies due to its trigonal distortion in ReO_6 octahedra.

Examination of Fig. 5.3 uncovers the way to construct the low-energy spin Hamiltonian. Analysis of the energy diagram showed that,

(i) in Mn1-Mn2-Ni(Co)-Re basis, the Re t_{2g} states are non-magnetic with negligible exchange splitting, (ii) the Re t_{2g} states lie within the exchange split states of Mn1 d, Mn2 d and Ni e_g/Co d, and most importantly (iii) switching on the hybridization between Mn1 d/Mn2 d/Ni e_g(Co d) and Re t_{2g} develops an induced exchange splitting of 0.6-0.8 eV among the Re t_{2g} states, with the direction of spin splitting opposite to that of Mn1 or Mn2 or Ni/Co.

The above observation establishes the hybridization-driven multi sublattice double-exchange process to be operative, in which a negative spin splitting in the non-magnetic site is induced through hybridization between the localized spin and itinerant electrons [7, 8]. This can be achieved in terms of a 3+1 sublattice Kondo Lattice model, consisting of (i) a large core spin at the Mn1, Mn2 and Ni(Co) sites, (ii) strong coupling on the Mn1/Mn2/Ni(Co) site between the core spin and the itinerant electron, strongly preferring one spin polarization of the itinerant electron, and (iii) delocalization of the itinerant electron on the Mn1-

Mn2-Ni(Co)-Re network. Following Ref. [14], the corresponding spin Hamiltonian can be written as,

$$\begin{aligned} H_{DE} &= \epsilon_B \sum_{i\sigma} b^\dagger_{i\sigma} b_{i\sigma} + \epsilon_{Mn1} \sum_i m^{1\dagger}_{i\sigma} m^1_{i\sigma} \\ &+ \epsilon_{Mn2} \sum_i m^{2\dagger}_{i\sigma} m^2_{i\sigma} + \epsilon_{Re} \sum_i r^\dagger_{i\sigma} r_{i\sigma} \\ &+ t_{B-Re} \sum_{\langle ij \rangle} (b^\dagger_{i\sigma} r_{j\sigma} + h.c.) \\ &+ t_{Mn1-Re} \sum_{\langle ij \rangle} (m^{1\dagger}_{i\sigma} r_{j\sigma} + h.c.) \\ &+ t_{Mn2-Re} \sum_{\langle ij \rangle} (m^{2\dagger}_{i\sigma} r_{j\sigma} + h.c.) \\ &+ J_B \sum_{i \in B} \vec{S}^B_i \cdot b^\dagger_{i\alpha} \vec{\sigma}_{\alpha\beta} b_{i\beta} \\ &+ J_{Mn1} \sum_{i \in A'} \vec{S}^{Mn1}_i \cdot m^{1\dagger}_{i\alpha} \vec{\sigma}_{\alpha\beta} m^1_{i\beta} \\ &+ J_{Mn2} \sum_{i \in A''} \vec{S}^{Mn2}_i \cdot m^{2\dagger}_{i\alpha} \vec{\sigma}_{\alpha\beta} m^2_{i\beta} \end{aligned} \tag{5.1}$$

where the m's and b's represent the Mn and the B (Ni/Co) sites respectively. t_{B-Re}, t_{Mn1-Re}, t_{Mn2-Re} denote the nearest neighbour B-Re, Mn1-Re, Mn2-Re hoppings respectively with onsite elements ϵ_B, ϵ_{Mn1}, ϵ_{Mn2} and ϵ_{Re}. The 'classical' core spins at the Mn1/Mn2/B sites are denoted by S_i, coupled to the itinerant Re electrons through a coupling J, when the Re electron hops onto the respective sublattice.

The Kondo coupling parameter J in H_{DE} is present only at the magnetic Mn1, Mn2 and B sites possessing a large core spin of $S = 5/2$ at Mn1 and Mn2, $S = 1$ for Ni and $S = 3/2$ for Co, with which the itinerant Re electron interacts with these magnetic sites through hopping. The ratio J/W of Kondo coupling (J) and bandwidth (W) is thus relevant only on the magnetic Mn1, Mn2 and B (Ni/Co) sites.

Using the DFT inputs, the calculated J/W ratios for the Mn1, Mn2 and Ni sites in CMNRO were found to be 3.77, 2.06 and 2.7 respectively. The ratios for the Mn1, Mn2 and Co sites in CMCRO were found to be 3.529, 1.87 and 3.5 respectively. Thus the exchange coupling J is appreciably larger than the bandwidth W for all the magnetic sites in these two compounds. Along with this as the bandwidth, $W \approx zt$ where t's are the hopping parameters and z is the number of neighbours, the J/t ratios were found to be even larger, of the order of 8 or 10, justifying the use of $J \to \infty$ model. The $J \to \infty$ limit of double-exchange models was used by Anderson and Hasegawa [36] and further studied in the context of

perovskites by P. De Gennes [37].

Applying the $J \to \infty$ approximation, we derived the effective spin Hamiltonian for CMNRO in terms of the core spins at Mn1 ($S = 5/2$), Mn2 ($S = 5/2$) and Ni ($S = 1$) site as given in the following.

$$\begin{aligned} H'_{DE} &= 4D_{Mn1-Mn2} \sum_{<ij>i\in A',j\in A''} \sqrt{\frac{1+\mathbf{S}_i^{Mn1}\cdot\mathbf{S}_j^{Mn2}}{2}} \\ &+ 8D_{Mn1-Ni} \sum_{<ij>i\in A',j\in B} \sqrt{\frac{1+\mathbf{S}_i^{Mn1}\cdot\mathbf{S}_j^{Ni}}{2}} \\ &+ 8D_{Mn2-Ni} \sum_{<ij>i\in A'',j\in B} \sqrt{\frac{1+\mathbf{S}_i^{Mn2}\cdot\mathbf{S}_j^{Ni}}{2}} \end{aligned} \tag{5.2}$$

A similar Hamiltonian for the Co compound CMCRO, with $\mathbf{S}^{Ni}$ ($S = 1$) replaced by $\mathbf{S}^{Co}$ ($S = 3/2$), and coupling constants $D_{Mn1-Mn2}$, D_{Mn1-Co} and D_{Mn2-Co} was also constructed.

The above multi sublattice double-exchange Hamiltonian described the ferromagnetic state of CMNRO, but it failed to explain the change from ferromagnetic to ferrimagnetic state on replacement of Ni by Co in CMCRO, suggesting the presence of another source of magnetism together with hybridization-driven double-exchange mechanism.

Indeed, the superexchange between the half-filled Mn1-d, Mn2-d, Ni e_g, and high spin Co (t_{2g} + e_g) states played an important role as the another source of magnetism. According to the Goodenough-Kanamori rule [38] superexchange interactions are antiferromagnetic for the virtual electron hopping between half-filled orbitals, and that becomes ferromagnetic for the virtual electron hopping from a half-filled to an empty orbital or from a filled to a half-filled orbital. Thus following the rule, all the superexchange contributions in the present context were found to be antiferromagnetic in nature as shown in Fig. 5.4.

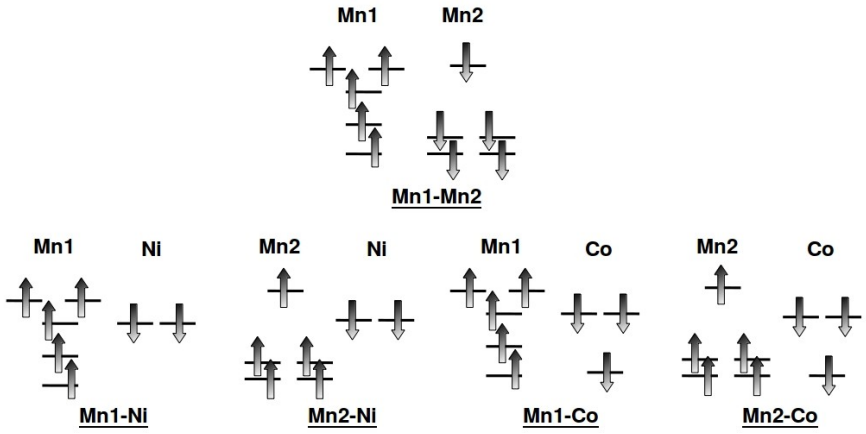

Figure 5.4: Superexchange interactions in CMNRO and CMCRO between half-filled d states of Mn1, Mn2, half-filled e_g states of Ni and half-filled e_g and one of the t_{2g} states of Co. The fully filled states with no contribution in superexchange are not shown.

The strength of these antiferromagnetic superexchange interactions were defined as,

$$J \propto \sum_{m,m'} t^2_{m,m'}/(U + \Delta_{m,m'}) \tag{5.3}$$

where, t are the hopping integrals, $\Delta_{m,m'}$ is the onsite energy differences of m and m' orbitals at site i (Mn1/Mn2/Ni(Co)) and j (Mn1/Mn2/Ni(Co)).

The net Hamiltonian for CMNRO incorporating the contributions of double-exchange as well as superexchange is thus given by,

$$\begin{aligned}
H &= 4D_{Mn1-Mn2} \sum_{<ij>i\in A',j\in A''} \sqrt{\frac{1+\mathbf{S}_i^{Mn1}\cdot\mathbf{S}_j^{Mn2}}{2}} \\
&+ 8D_{Mn1-Ni} \sum_{<ij>i\in A',j\in B} \sqrt{\frac{1+\mathbf{S}_i^{Mn1}\cdot\mathbf{S}_j^{Ni}}{2}} \\
&+ 8D_{Mn2-Ni} \sum_{<ij>i\in A'',j\in B} \sqrt{\frac{1+\mathbf{S}_i^{Mn2}\cdot\mathbf{S}_j^{Ni}}{2}} \\
&+ 4J_{Mn1-Mn2} \sum_{<ij>i\in A',j\in A''} \mathbf{S}_i^{Mn1}\cdot\mathbf{S}_j^{Mn2} \\
&+ 8J_{Mn1-Ni} \sum_{<ij>i\in A',j\in B} \mathbf{S}_i^{Mn1}\cdot\mathbf{S}_j^{Ni} \\
&+ 8J_{Mn2-Ni} \sum_{<ij>i\in A'',j\in B} \mathbf{S}_i^{Mn2}\cdot\mathbf{S}_j^{Ni}
\end{aligned} \tag{5.4}$$

The net Hamiltonian was also obtained for CMCRO in similar fashion.

In order to estimate the various coupling constants of Eq. (5.4) we applied a two step process. In the first step, we constructed a spin unpolarized Mn1-Mn2-Ni(Co) Hamiltonian defined in effective Mn1-d, Mn2-d, Ni e_g (Co d) basis by applying the downfolding technique [34]. The real space representation of this Hamiltonian provided the estimate of onsite matrix elements of Mn1-d, Mn2-d, Ni e_g (Co d) and the hopping interactions between them. The antiferromagnetic superexchange coupling J's were computed using $J = \sum_{m,m'} 2 \times t^2_{m,m'}/(U + \Delta_{m,m'})$. In the second step, the total energies for different possible spin configurations at Mn1, Mn2 and Ni(Co) sites were calculated, and mapped on to the spin Hamiltonian given in Eq. (5.2). Putting the values of J's obtained from superexchange formula, the estimates of double-exchange couplings were obtained. The estimated values of D's, and J's for the two compounds are presented in Table-5.1.

CMNRO	D **(meV)**	JS^2 **(meV)**	**Effective (meV)**
Mn1-Mn2	-91.7 (-94.7)	47.5 (48.8)	-44.2 (-45.9)
Mn1-Ni	-123.5 (-117.3)	54.8 (56.1)	-68.7 (-61.2)
Mn2-Ni	-28.6 (-29.6)	10.8 (9.7)	-17.8 (-19.9)
Mn@Ni-Mn1	-100.9	37.9	-63.0
Mn@Ni-Mn2	-50.3	30.1	-20.2
CMCRO	D **(meV)**	JS^2 **(meV)**	**Effective (meV)**
Mn1-Mn2	1.9 (2.1)	48.5 (44.6)	50.4 (46.7)
Mn1-Co	-143.9 (-147.4)	87.9 (86.1)	-56.0 (-61.3)
Mn2-Co	-18.7 (-19.8)	41.0 (43.1)	22.3 (23.3)
Co@Mn2-Mn1	2.4	47.7	50.1
Co@Mn2-Co	-150.3	88.1	-62.2

Table 5.1: Estimates of the coupling constants connecting the core spins for the hybridization-driven double-exchange and superexchange mechanisms operative in CMNRO and CMCRO, as estimated employing the superexchange formula and total energy calculations of different spin configurations. Negative and positive signs indicate ferro and antiferro magnetic interactions respectively.

Analysis of Table-5.1 it was found that while the strength of Mn1-Mn2 superexchange ($J_{Mn1-Mn2}$) remains similar between the two compounds, the strength of Mn1/Mn2-B superexchange is enhanced greatly in CMCRO compared to CMNRO. Superexchange coupling $J_{Mn1-Ni/Co}$ got enhanced by a factor of 1.6 and $J_{Mn2-Ni/Co}$ got enhanced by a factor of 3.2. This was expected due to the fact that while for Ni, two unpaired e_g electrons participate in the superexchange process while for Co, three unpaired electrons, two belonging to the e_g manifold and one belonging to t_{2g} manifold contribute. In the contrast a significant weakening of the hybridization-driven exchange between Mn1-Mn2, reduced by two orders of magnitude compared to Ni compound, was also found. These important changes turned the net interaction to be antiferromagnetic between Mn1 and Mn2, and

that between Mn2 and Co, while all the effective interactions were ferromagnetic in the Ni compound.

5.3.4 Monte Carlo study of the spin Hamiltonian

To evaluate the finite temperature properties of the defined spin Hamiltonian, described by Eq. (5.4), we performed Monte Carlo simulations.

We obtained the total energy of a particular spin configuration from the spin Hamiltonian by plugging in the input parameters D's and J's, as listed in Table-5.1. The spin configurations at Mn1, Mn2 and Ni/Co sites were generated through Metropolis algorithm in a 3×3×3 unit cell simulation box considering the periodic boundary condition.

Starting from an initial temperature of 400 K (1000 K) for CMNRO (CMCRO) the simulation temperature was stepped down to $T = 1$ K with an interval of 2 K. Hundred thousand Monte Carlo steps were employed to ensure a large sample space. The physical quantity e.g. magnetization was calculated by averaging over the last 10,000 Monte Carlo steps. The magnetizations plotted as a function of temperature for CMNRO and CMCRO are shown in Fig. 5.5. Analysis of Monte Carlo results revealed that for CMNRO compound, the metropolis simulation reproduced the ground state correctly with parallel spin alignment of Mn1, Mn2 and Ni (cf. top, left panel, Fig. 5.5). The total moment at low-temperature was found to be 28 μ_B/unit cell which came from the sum of the nominal moment of 5 μ_B for 2 Mn1 and 2 Mn2 with the nominal moment of 2 μ_B for 4 Ni sites.

We calculated the transition temperature (T_C) from the inflection point of the derivative of magnetization vs. temperature curve, as shown in the top panel, Fig. 5.5. The obtained T_C value for CMNRO from our calculation was found to be 142 K which is in good agreement with experimentally reported value of 158 K [27].

For CMCRO compound, the ferrimagnetic ground state was also correctly captured with antiparallel spin alignment of Mn2 to that of Mn1 and Co. The total calculated moment was found to be 12 μ_B/unit cell, arising from magnetic moment of 3 μ_B in 4 Co sites and cancellation of moments at Mn1 and Mn2 sites.

The transition in the case of CMNRO is prominently sharper compared to CMCRO, as reflected in the narrower width of the inverse peak in dM/dT curve. More interestingly in CMCRO, a shoulder was observed in the left of the inverse peak which was completely absent in CMNRO.

Repeating the calculation with larger simulation cell also established that the peak and shoulder structure in CMCRO is robust arising from the competition between effective ferromagnetic Mn1-Co interaction and the two effective antiferromagnetic Mn1-Mn2 and Mn1-Co interactions.

We checked the effect of competing nature of magnetic interactions in dM/dT curve of CMCRO compound and showed the dM/dT curve for varying D_{Mn1-Co}

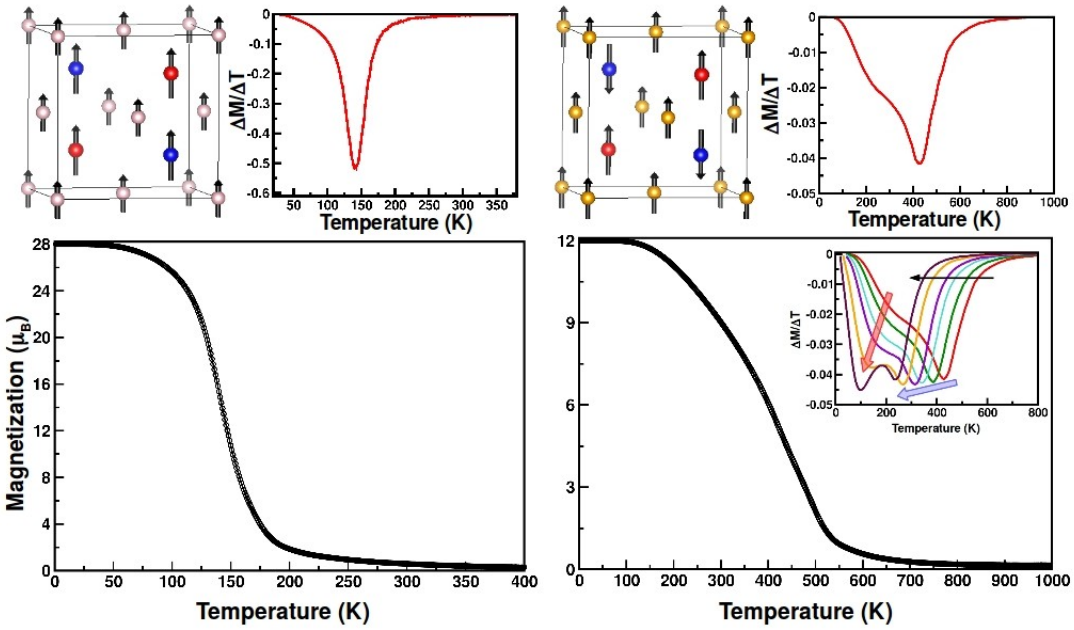

Figure 5.5: Magnetic properties of CMNRO (left) and CMCRO (right) obtained through Monte Carlo simulation. Top-left panels show the ground state magnetic structures, while the top-right panels show the derivative of magnetization as a function of temperature of the corresponding compounds. The minimum of the derivative of magnetization vs. temperature curve corresponds to the transition temperature of respective compound. Mn1, Mn2, Ni(Co) atoms are marked by red, blue and light pink (yellow) balls respectively. The lower panels show the magnetization, plotted as a function of temperature for CMNRO (left) and CMCRO (right). The inset in lower, right panel shows the shift of transition temperature (the minima of the curves) for monotonic decrease of double-exchange coupling D_{Mn1-Co}.

value in the inset of bottom right panel of Fig. 5.5. The results showed that on reducing D_{Mn1-Co} from DFT estimated value of -143.9 meV to -135.9 meV, i.e. weakening ferro interaction, the high-temperature peak got shifted to lower temperature, redistributing the height between the peak and the shoulder, converting the shoulder to the peak. Thus the shoulder feature resembles second peak which becomes unresolved on comparable strength of ferro and antiferro interactions. This suggests that the high-temperature peak appeared due to the ferro interaction while the lower temperature feature came from the antiferro interaction.

The experimental study [27] on CMCRO reported only magnetic susceptibility without any information regarding dM/dT. However reported experimental dM/dT data for Nd_2NiMnO_6, double perovskite with multiple magnetic sublattices exhibits such two feature structure [39]. Such peak-shoulder feature in dM/dT curve is also observed for ferrimagnetic compound $NiCr_2O_4$ [40].

From our calculation it is noticed that with the choice of DFT estimated value of D_{Mn1-Co}, the second feature appears around 200 K which is very close to the experimentally reported T_C, 188 K [27].

5.3.5 Effect of off-stoichiometry

The experimental samples of CMNRO and CMCRO were reported to be off-stoichiometric [27] showing a high degree of B site cation ordering with nominal antisite disorder of 3.4 and 2.5% for the Co and Ni compounds respectively. For CMCRO, while there is 96% Co at the octahedral B site, 30-40% of Co was reported to substitute Mn at the A sites giving rise to an overall Co-rich composition with formula $CaMn_{0.7}Co_{1.3}ReO_6$ opposing to the stoichiometric formula of $CaMnCoReO_6$.

Similarly, for CMNRO, an overall Ni-poor composition $CaMn_{1.2}Ni_{0.8}ReO_6$ was reported with some of the Mn atoms occupying Ni sites in B sublattice.

Thus to check the validity of the theoretical understanding as used for the stoichiometric compounds, we also carried out our calculations for the experimentally reported off-stoichiometric compounds. To mimic the experimental situation of off-stoichiometry, we replaced one out of the four Ni atoms in the unit cell by Mn, giving rise to Ni poor composition of formula $CaMn_{1.25}Ni_{0.75}ReO_6$. Since all four Ni sites are equivalent in the unit cell, any one chosen out of four possible sites, gave rise to same results.

Similarly, for CMCRO, an extra Co atom replacing one of the four Mn atoms in the unit cell was introduced, giving rise to composition $CaMn_{0.75}Co_{1.25}ReO_6$.

Our total energy calculations showed that Co prefers to occupy the square planar Mn site (Mn2) instead of tetrahedrally coordinated Mn site (Mn1). For CMNRO it was found that even in presence of off-stoichiometry the ground state remains ferromagnetic with Mn1, Mn2, Mn@Ni and Ni spins aligned in parallel direction, suggesting the dominant role of hybridization-driven magnetism, as opposed to superexchange driven mechanism which depends on the position of the energy levels instead of the exchange pathways.

Similarly, for off-stoichiometric CMCRO, the spin alignment of Mn1 and Mn2 remained unaltered as that in the stoichiometric Co compound while the Co spins (both at A″ site and B site) were found to be oppositely aligned to Mn2.

Thus the magnetic ground states were found to be robust, i.e they remained unaltered even in presence of off-stoichiometry, as also found experimentally.

The computed Mn1-Mn2, Mn1-Ni(Co), Mn2-Ni(Co) exchanges for the off-stoichiometric Ni and Co compounds were found not to change significantly compared to their stoichiometric counterparts ($\sim$ 3-10%) as shown in Table-5.1. Although off-stoichiometry introduced few additional interactions like Mn@Ni-Mn1, Mn@Ni-Mn2 replacing some of Ni-Mn1, Ni-Mn2 interactions respectively in CMNRO. In CMCRO, Co@Mn2-Mn1, Co@Mn2-Co interactions were introduced by

replacing some of Mn2-Mn1, Mn2-Co interaction respectively.

Computation of these additional interactions showed that the signs of effective interactions corresponding to these additional interactions were the same as those of the replacing interactions, with values raging between 5-7%. This suggests that the magnetic transition temperature should not be altered drastically in presence of off-stoichiometry. We carried out Monte Carlo study for the Ni-poor and Co-rich compounds with a 3×3×3 unit cell simulation box size to check the issue explicitly.

The total energy calculations showed that extra Mn(Co) atoms at Ni(Mn2) sites prefer to be uniformly distributed rather than being clustered. Considering the uniform distribution of extra Mn(Co) atoms in 3×3×3 unit simulation cell led to 152 different configurations. Considering this the Monte Carlo results were averaged over atomic configurations.

The ground state was found to be ferromagnetic for CMNRO and ferrimagnetic for CMCRO making a good agreement with the DFT results.

The variation of moment with temperature for the respective off-stoichiometric compounds are shown Fig. 5.6.

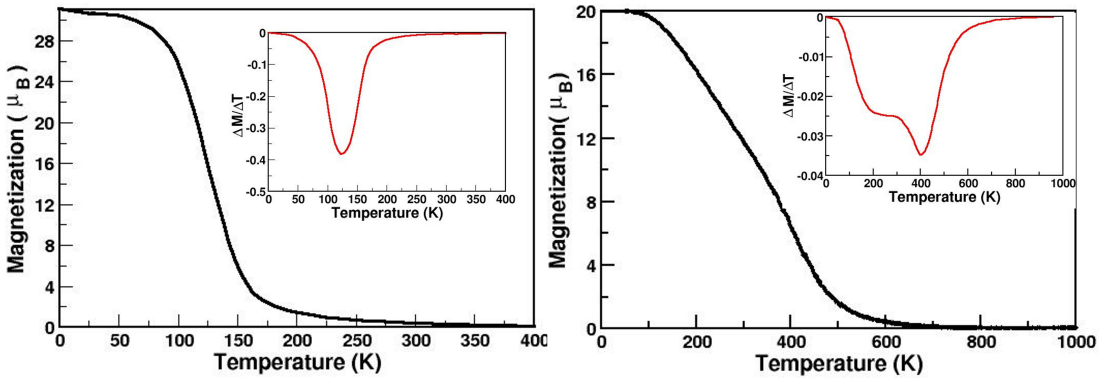

Figure 5.6: Magnetic properties of $CaMn_{1.25}Ni_{0.75}ReO_6$ (left) and $CaMn_{0.75}Co_{1.25}ReO_6$ (right) obtained from Monte Carlo simulation. The derivative of magnetization vs. temperature is shown in the insets.

Our study showed that in presence of off-stoichiometry, the saturation moment for CMNRO and CMCRO became 31 μ_B/unit cell and 20 μ_B/unit cell respectively. The dM/dT curves in the insets of Fig. 5.6 shows similarity with that found for stoichiometric compounds, confirming that the presence of off-stoichiometry not having significant influence on the transition temperature.

5.4 Summary

Here we studied the magnetism for the multi magnetic sublattice systems being motivated by the synthesis of double double perovskite compounds of general formula $AA'_{0.5}A''_{0.5}BB'O_6$ with transition metal magnetic ions in both A and B sites. The results of our study are summarized as follows:

- Theoretical analysis considering first-principles and model Hamiltonian approaches, uncovered the microscopic origin of the long range ordered magnetism in double double perovskite compounds containing $3d$ magnetic ions at A and B sites, and $5d$ magnetic ions at B′ sites bringing out the interplay of hybridization driven multi-sublattice double-exchange and superexchange mechanism of magnetism.

- This interplay was found to be dependent on the position of the d energy levels as well as its filling. This supported the ferromagnetic long range order in CMNRO compound with two different Mn ions at A sites, and Ni and Re ions at B and B′ sites. The replacement of Ni by Co at B site decreased the filling by one in CMCRO stabilizing ferrimagnetism making good agreement with experimental observations [27].

- The spin Hamiltonian taking into account the interplay of hybridization driven multi sublattice double exchange and superexchange mechanism of magnetism was parameterized in terms of three hybridization driven exchange constants e.g. $D_{Mn1-Mn2}$, $D_{Mn1-Ni/Co}$, $D_{Mn2Ni/Co}$ and another three superexchange constants $J_{Mn1-Mn2}$, $J_{Mn1-Ni/Co}$, $J_{Mn2-Ni/Co}$. These exchange coupling constants were obtained from first-principles estimated hopping interactions, onsite energies and total energies of different spin configurations.

- The computed temperature dependent magnetization by Monte Carlo simulation reproduced the experimentally observed magnetic transition temperature of CMNRO with reasonable accuracy. For CMCRO, it was found that the competition between ferro and antiferro nature of the effective interactions, gave rise to two hump structures of dM/dT curve.

- Our calculations for off-stoichiometric composition of Ni-poor and Co-rich compounds, reproduced the experimental situation. The magnetic properties were found to be unaltered even in presence of off-stoichiometry, as the hybridization driven multi sublattice double-exchange, a dominant contributor in exchange mechanism of CMNRO and CMCRO, depends on the energy level position instead of the exchange pathways.

Bibliography

[1] C. N. R. Rao, Annu. Rev. Phys. Chem. **40**, 291 (1998).

[2] A. S. Bhall, R. Guo, R. Roy, Mater Res Innov. **4**, 3 (2000).

[3] G. King, P. M. Woodward, J. Mater. Chem. **20**, 5785 (2010).

[4] T. Saha-Dasgupta, J. Superconductivity and Novel Mag. **26**, 1991 (2013).

[5] S. Vasala, M. Karppinen, Prog. Solid State Chem. **43**, 1 (2015).

[6] T. Saha-Dasgupta, Mater. Res. Express **7**, 1 (2020).

[7] D. D. Sarma, P. Mahadevan, T. Saha Dasgupta, S. Ray, A. Kumar, Phys. Rev. Lett. **85**, 2549 (2000).

[8] K.-I. Kobayashi, T. Kimura, H. Sawada, K. Terakura, Y. Tokura, Nature (London) **395**, 677 (1998).

[9] H. Das, U. V. Waghmare, T. Saha-Dasgupta, D. D. Sarma, Phys. Rev. Lett. **100**, 186402 (2008).

[10] A. Chattopadhyay and A. J. Millis, Phys. Rev. B **64**, 024424 (2001).

[11] L. Brey, M. J. Calderon, S. Das Sarma and F. Guinea, Phys. Rev. B **74**, 094429 (2006).

[12] J. L. Alonso, L. A. Fernandez, F. Guinea, F. Lesmes, and V Martin-Mayor, Phys. Rev. B **67**, 214423 (2003).

[13] J. B. Phillip, P. Majewski, L. Alff, A. Erb, R. Gross, T. Graf, M. S. Brandt, J. Simon, T. Walther, W. Mader, D. Topwal, and D. D. Sarma, Phys. Rev. B **68**, 144431 (2003).

[14] P. Sanyal, P. Majumdar, Phys. Rev. B **80**, 054411 (2009).

[15] H. Kato, T. Okuda, Y. Okimoto, and Y. Tomioka, App. Phys. Lett. **81**, 328 (2002).

[16] Y. Krockenberger *et al.*, Phys. Rev. B **75**, 020404(R) (2007).

[17] J. Li, A. W. Sleight, M. A. Subramanian, Adv. Mater. **17**, 2225 (2005).

[18] H. Das, U. V. Waghmare, T. Saha-Dasgupta, D. D. Sarma, Phys. Rev. B **79**, 144403 (2009).

[19] P. Sanyal, Phys. Rev. B **96**, 214407 (2017).

[20] H. Das, P. Sanyal, T. Saha-Dasgupta, D. D. Sarma, Phys. Rev. B **83**, 104418 (2011).

[21] A. Halder, P. Sanyal, T. Saha-Dasgupta, Phys. Rev. B **99**, 020402 (R) (2019).

[22] K Samanta, P Sanyal, T. Saha-Dasgupta, Sci. Rep. **5**, 15010 (2015).

[23] E. Solana-Madruga, A. M. Arévalo-Lópẹz, A. J. Dos santos-Garcá, E. Urones-Garrote, D. Avila-Brande, R. Sáéz-Puche, J. P. Attfield, Angew. Chem., Int. Ed. **55**, 9340 (2016).

[24] G. M. McNally, A. M. Arévalo-López, P. Kearins, F. Orlandi, P. Manuel, J. P. Attfield, Chem. Mater. **29**, 8870 (2017).

[25] E. Solana-Madruga, A. M. Arévalo-López, A. J. Dos santos-Garcá, C. Ritter, C. Cascales, R. Sáez-Puche, J. P. Attfield, Phys. Rev. B **97**, 134408 (2018).

[26] E. Solana-Madruga, A. J. Dos santos-Garca, A. M. Arvalo Lýpez, D. Avila-Brande, C. Ritter, J. P. Attfield, J. Saez-Puche, R. Dalton Trans **44**, 20441 (2015).

[27] E. Solana-Madruga, Y. Sun, A. M. Arévalo-López, J. P. Attfield, Chem. Commun. **55**, 2605 (2019).

[28] G. Kresse, J. Furthmüller, Comput. Mater. Sci **6**, 15 (1996).

[29] J. P. Perdew, K. Burke, M. Ernzerhof, Phys. Rev. Lett. **77**, 3865 (1996); ibid **78**, 1396(E) (1991).

[30] P. E. Blöchl, Phys. Rev. B **50**, 17953 (1994).

[31] S. L. Dudarev, G. A. Botton, S. Y. Savrasov, C. J. Humphreys, A. P. Sutton, Phys. Rev. B **57(3)**, 1505 (1998).

[32] E. R. Ylvisaker, W. E. Pickett, and K. Koepernik, Phys. Rev. B **79**, 035103 (2009).

[33] I. V. Solovyev, P. H. Dederichs, V. I. Anisimov, Phys. Rev. B **50**, 16861 (1994).

[34] O. K. Andersen, T. Saha-Dasgupta, Phys. Rev. B **62**, R16219 (2000).

[35] O. K. Andersen, O. Jepsen, Phys. Rev. Lett. **53**, 2571 (1994).

[36] P.W. Anderson and H. Hasegawa, Phys. Rev. **100**, 675 (1955).

[37] P.-G de Gennes, Phys. Rev. **118**, 141 (1960).

[38] P. W. Anderson, Phys. Rev. **79** 350 (1950); J. B. Goodenough, Phys. Rev. **100** 564 (1955); J. Kanamori, J. Phys. Chem. Solids. **10** 87 (1959).

[39] R. Das, P. Yanda, A.Sundaresan and D.D. Sarma, Mater. Res. Express **6** 116122 (2019).

[40] A. Ali, G. Sharma, Y. Singh, arXiv:1811.07836.

Chapter 6

$NiRh_2O_4$: A spin-orbit entangled diamond-lattice paramagnet*

6.1 Introduction

Topology in electronic system includes two-dimensional (2D), three-dimensional (3D) topological insulators [1, 2], Weyl semimetals [3], and topological superconductors [2] showing the nature of symmetry protected topological (SPT) phases.

This paved the path for the proposal of interacting spins and bosons supporting SPT phases with conventional bulk excitations but unconventional gapless or gapped edge states [4–8].

Following the prescription of spin-1 system, recently an exciting suggestion has been reported that, certain spin-1 model on diamond lattice may represent a time-reversal symmetry protected topological quantum paramagnet [9] being a 3D analog of Haldane chain [10, 11], with gapless 2D surface states. This suggestion has showered interest on the spinel materials of general chemical formula AB_2O_4 with A site spins on the diamond lattice.

Spinels like $MnSc_2S_4$ with S = 5/2, $CoAl_2O_4$ and $CoRh_2O_4$ with S = 3/2, and $CuRh_2O_4$ with S = 1/2, exhibit spin spiral or helix or Néel ordering [12–18]. In contrast to these, spinel $FeSc_2S_4$ shows very weak Néel ordering at the vicinity of a nonmagnetic ground state being induced by spin-orbit coupling (SOC) [19–21]. Although it is reported that excess Fe plays a significant role in pronounced magnetic irreversibility, hence the Néel ordering [22].

*Based on publication: **Shreya Das**, Dhani Nafday, Tanusri Saha-Dasgupta, and Arun Paramekanti; **Phys. Rev. B 100, 140408(R) (2019)**.

The need for spin-1 topological paramagnets recently put emphasis on the investigation of $NiRh_2O_4$ [23]. Magnetic ion with S = 1 on the A site like Ni^{2+} with d^8 occupancy can be realized as a S = 1 diamond lattice. However according to crystal field splitting, stabilization of Ni^{2+} at A site with tetrahedral coordination is exceptionally tough, and it favours to put Ni^{2+} on the B site which is octahedrally coordinated [23]. In this regard, $NiRh_2O_4$ is an unconventional example of spin-1 system consisting of $3d$ ions on the tetrahedrally coordinated A site, structurally stabilized by the placement of $4d$ Rh^{3+} ion at the octahedral B site.

$NiRh_2O_4$ is reported to be cubic at high-temperature [23, 24], which undergoes structural transformation from cubic to tetragonal phase below $T \sim 440$ K. The tetragonal phase is found to be with $c/a \approx 1.05$ (tetragonal elongation), S-1 ground state with orbital degeneracy. This tetragonal distortion associated with $c/a > 1$ makes the t_2 states of Ni partially filled and thus the active orbital degrees of freedom allow spin-obit coupling (SOC) to play an important role.

$NiRh_2O_4$ exhibits a Schottky anomaly in the specific heat at $T \sim$ 30-40 K, and spin gapped excitations in inelastic neutron scattering (INS) upon cooling. Previous studies on $NiRh_2O_4$ argued [23] to exhibit the characteristics of valence bond solids or topological paramagnets. On the other hand an alternate crystal field level scheme was also proposed with a nonmagnetic ground state [25]. In a theoretical study [26], $NiRh_2O_4$ was also considered to be a frustrated Heisenberg model with antiferromagnetic (AFM) first and second neighbour exchanges, J_1 and J_2 respectively, proposing a nonmagnetic ground state driven by large single-ion anisotropy DS_z^2, with $D > 0$ favouring local $S_z = 0$.

Another study of the J_1-J_2 model [27] revealed that while the S = 1 case favours a quantum spiral spin liquid, tetragonal distortion or large $D/J_1 \gtrsim 8$ favour Néel order or $S_z = 0$ ground state respectively. These previous studies ignored orbital degrees of freedom.

In recent time, spin-orbit coupling in a tetrahedral coordination is argued to support a $J_{eff} = 0$ state with d^8 occupancy [28]. This situation becomes similar to $J_{eff} = 0$ insulators with d^4 occupancy in an octahedral coordination [29–31]. The INS results [23] on $NiRh_2O_4$ also remained inconclusive because this work used spin-wave theory with assumption of AFM order but this assumption was not appropriate in absence of long range order.

Given that there are many contradicting suggestions about $NiRh_2O_4$, a proper and consistent theory of it is needed. Here, we combined first-principles density functional theory (DFT) based calculations armed with a model Hamiltonian approach to unravel the curious case of $NiRh_2O_4$ as well as to explain the existing data and make concrete predictions.

6.2 Crystal structure

The crystal structures of $NiRh_2O_4$ in high-temperature cubic phase with $Fd\bar{3}m$ symmetry [23] and low-temperature tetragonal phase with $I4_1/amd$ symmetry [32] are shown in left and right panels of Fig. 6.1 respectively.

The conventional unit cell of cubic and tetragonal $NiRh_2O_4$ consists of eight

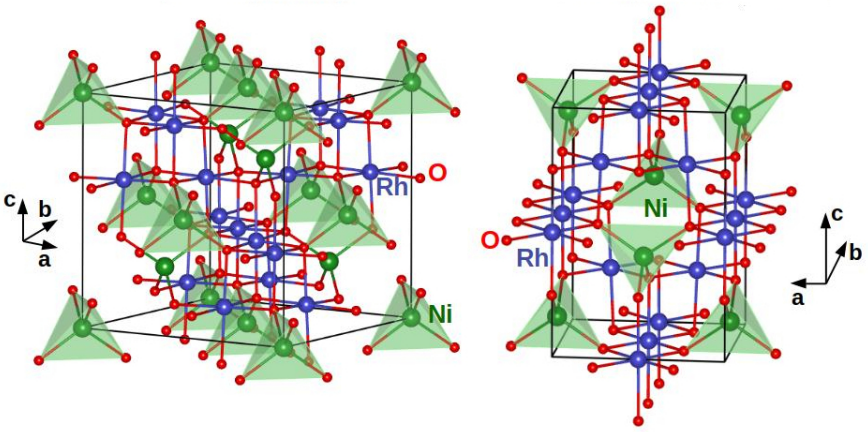

Figure 6.1: Crystal structure of $NiRh_2O_4$ in high-temperature cubic (left panel) phase and low-temperature tetragonal (right panel) phase. Green, blue and red balls represent Ni, Rh and O sites, respectively.

formula units with 56 atoms, and four formula units with 28 atoms respectively. The lattice parameter of the cubic phase is found to be $a = 8.477$ Å with Ni, Rh and O Wyckoff positions of $8a$, $16d$ and $32e$ respectively. The lattice parameters for tetragonal phase are $a = 5.912$ Å and $c = 8.670$ Å with Ni, Rh and O occupying Wyckoff positions of $4a$, $8d$ and $16e$, respectively.

In cubic phase there are four Ni-Ni nearest neighbours (NN) with distance 3.670 Å and twelve Ni-Ni next nearest neighbours (NNN) with distance of 5.990 Å.

Structural transition from cubic to tetragonal at low-temperature lowers the crystal symmetry leading slight decrease of the four NN Ni-Ni distance. Lowered structural symmetry of tetragonal phase also makes the twelve NNN Ni-Ni bonds to group into four in-plane bonds with length 5.912 Å and eight out-of-plane bonds with length 6.022 Å.

6.3 Density functional theory calculation details

Here we carried out density functional theory based calculations using the following three different basis sets as,

(a) plane-wave basis set as implemented in the Vienna *ab-initio* Simulation Package (VASP) [33], (b) muffin-tin orbital (MTO) based linear muffin-tin orbital (LMTO) method [34] along with the N^{th} order MTO method (NMTO) [35] as implemented in the STUTTGART code, and (c) the full-potential linearized augmented plane wave (FLAPW) basis set as implemented in the Wien2k package [36].

The consistency of the calculations executed in above mentioned different basis sets was cross checked in terms of density of states, and band structure calculations.

The self-consistent-field total energy calculations and the density of states calculations were carried out with the plane-wave basis and projector-augmented wave (PAW) potentials [37].

We chose the potentials of Ni, Rh and O as the electronic configurations, $[Ar]3d^84s^2$, $[Kr]4d^85s^1$, and $[He]2s^22p^4$ respectively. We used exchange-correlation functional as the generalized gradient approximation (GGA) implemented as in the Perdew-Burke-Ernzerhof (PBE) prescription [38]. The effect of missing correlation beyond GGA was taken into account through supplemented Hubbard U in GGA+U calculation [39]. We made the choice of typical U value of 5 eV for $3d$ transition metal Ni accompanied by Hund's coupling, $J_H = 1$ eV. Validity of the results were also checked by varying the U value by 1-2 eV at Ni site and it was found that the qualitative trend remained unchanged.

Spin-orbit coupling was included as a perturbation on a fully self-consistent basis. The effect of SOC was cross checked within the all-electron method of full-potential linearized augmented plane-wave (FLAPW) as implemented in WIEN2K code.

The convergence of APW + lo basis set was given by the common criteria of $R_{MT} \times K_{max} = 7.0$, where R_{MT} represents the smallest atomic sphere radius and K_{max} represents the plane-wave cutoff.

The Brillouin Zone sampling was done over an 6×6×6 k-mesh and self consistency was assumed to be achieved when the total energies were converged to within 0.001 eV.

In order to construct low energy Hamiltonian in the Ni-Rh and Ni only Wannier function basis, we applied NMTO-downfolding technique starting from a full DFT band structure and integrated out the O degrees of the freedom for the Ni-Rh basis, and integrated out O as well as Rh degrees of freedom for the Ni only basis. Thus in the first case, renormalization effect from oxygens were taken into consideration while for the second case, renormalization effect from both oxygen and Rh were incorporated. The carried out NMTO calculations relied on the potential used in self-consistent LMTO calculations.

The real space representation of the NMTO-downfolded Hamiltonian in the Wannier function basis provided the information of the onsite energies as well as other hopping integrals in the effective Wannier function basis.

The muffin tin radii of Ni, Rh and O were chosen to be 1.23 Å, 1.37 Å, and 1.00 Å respectively for LMTO calculations.

6.4 Results

6.4.1 Density functional theory

Electronic structure

The electronic structure calculation of $NiRh_2O_4$ within GGA+U scheme with $U_{Ni} = 5$ eV and $J_H = 1$ eV, gave half-metallic solution for both the high-temperature cubic and the low-temperature tetragonal phases as shown in the upper left and right panels of Fig. 6.2 respectively.

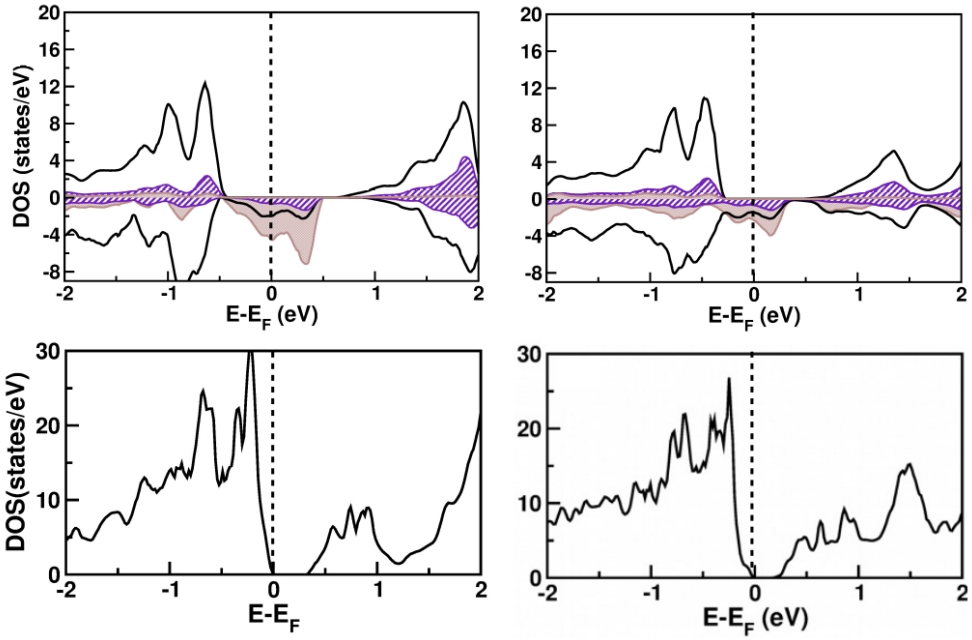

Figure 6.2: The GGA+U electronic structure of $NiRh_2O_4$ in high-temperature cubic (upper left) and low-temperature tetragonal phase (upper right) with states projected onto Ni d, Rh d, and O p as shown in gray-shaded, black-solid line, and hatched areas, respectively. The GGA+U+SOC electronic structure of $NiRh_2O_4$ in cubic and tetragonal phases are shown in lower left and lower right panels respectively.

In the cubic phase the octahedral coordination of Rh splits the $4d$ states into t_{2g} and e_g states with a large splitting ~ 3 eV, while the tetrahedral coordination

of Ni splits the $3d$ states into e and t_2 states with a relatively smaller splitting $\sim$ 0.6 eV as shown in the left panel of Fig. 6.3.

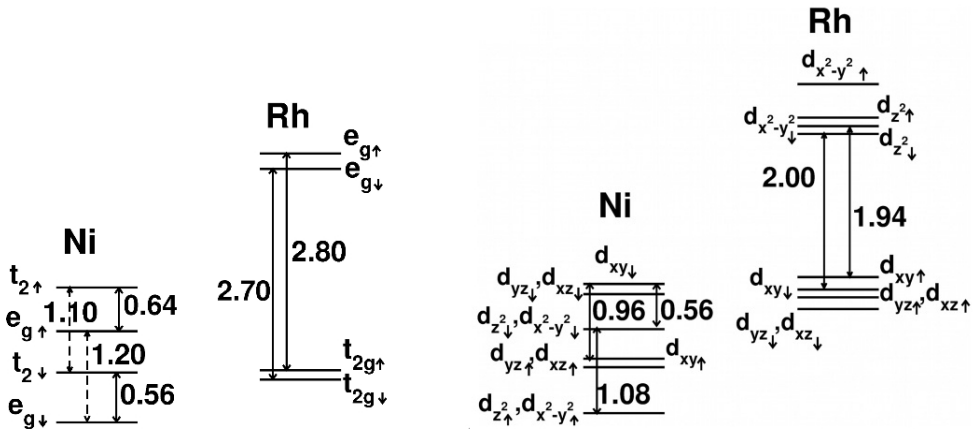

Figure 6.3: The energy level positions for the spin-split and the crystal-field-split of d states of Ni and Rh in case of cubic (left) and tetragonal (right) phases of $NiRh_2O_4$. For clarity, small splittings $\approx$ 0.1 eV are not shown.

Analysis of the energy level diagram and DOS structure for cubic phase showed that in the down-spin channel, the Ni t_2 states are admixed with Rh t_{2g} and O p states and cross the Fermi level (E_F) making the solution half-metallic. The Rh t_{2g} states are mostly occupied, while Rh e_g states are empty. This occupancy of d electrons of both Ni and Rh are in accordance with the nominal valence of Ni^{2+} (d^8) with two holes in t_2 manifold and low-spin d^6 occupancy of Rh^{3+}.

This general description remained valid in the tetragonal phase as seen in the right panel of Fig. 6.3. In the tetragonal phase, the calculated spin splitting at the Ni site was observed to be large ($\approx$ 1 eV) while that at the Rh site was an order of magnitude smaller being $\approx$ 0.1 eV supporting the nominal magnetic and nonmagnetic character of Ni^{2+} and Rh^{3+} respectively.

The tetragonal distortion introduces additional splitting among the cubic symmetry split states so that the Ni t_2 states further split with Ni d_{xy} level positioned above Ni d_{xz}/d_{yz} with splitting of $\approx$ 0.1 eV. The nature of splitting of the Ni t_2 states allows one of the two holes of Ni to occupy the down-spin d_{xy} level, while the other hole occupies the down-spin doubly degenerate d_{xz}/d_{yz} levels giving rise to a half-metallic solution in GGA+U scheme for tetragonal phase [cf. upper right panel Fig. 6.2].

Analysis of the the crystal and spin splittings in the tetragonal phase as shown in right panel of Fig. 6.3 also show the energetic proximity of Ni t_2 and Rh t_{2g} states in the down-spin channel, leading to a high degree of mixing between the two. This mixing resulted in a small magnetic moment $\approx$ 0.06-0.07 μ_B at the

nonmagnetic, low-spin, Rh site with d^6 occupancy, while the Ni moment was found to be $\approx$ 1.5-1.6 μ_B. Rest of the magnetic moment lied on the O sites, making the total moment of 2 μ_B/f.u. in both cubic and tetragonal phases.

Next we investigated the role of SOC due to the active Ni orbital degrees of freedom.

Our calculations within the GGA+U+SOC approach showed that Ni supports partially occupied $d_{xz} \pm id_{yz}$ orbitals, with a large orbital moment of $\sim$ 1.0 μ_B. This led to an S = 1, $L_{eff} = 1$ state, with parallel alignment of spin and orbital magnetization, confirming more than half-filling of d states of Ni.

Effect of U in GGA+U+SOC scheme, enhanced the orbital momentum of Ni significantly which GGA could not do due to its inability to capture the orbital polarization effect [40].

GGA+SOC was found unable to open up an insulating gap in-spite of splitting the partially occupied orbitally degenerate states in the down-spin channel making the situation similar to that of $FeCr_2S_4$ [41]. Application of Coulomb correlation in GGA+U+SOC scheme was found to open up an insulating charge gap for both cubic and tetragonal phases of $NiRh_2O_4$ as shown in the lower panels of Fig. 6.2 and the calculated insulating charge gap was found to be $\approx$ 0.25 eV [cf. lower right panel Fig. 6.2] for the low-temperature tetragonal phase.

Magnetic exchanges

In order to understand the magnetism, next we made estimate of dominant Ni-Ni magnetic exchanges from the knowledge of the effective hopping strengths and on-site energies in the Wannier basis of Ni t_2 only low-energy Hamiltonian derived through NMTO calculations.

Analysis of the dominant antiferromagnetic (AFM) interactions in cubic phase turned out to be between four nearest-neighbour (NN) Ni sites (J_1) belonging to two different face-centered cubic (fcc) sublattices of the diamond lattice, and 12 next-nearest neighbour (NNN) Ni sites (J_2) belonging to the same fcc sublattice as shown in left panel of Fig. 6.4. Due to the tetragonal distortion, the 12 NNN Ni-Ni interactions are grouped into four in-plane (J_2') and 8 out-of-plane (J_2'') interactions as shown in right panel of Fig. 6.4.

The significant mixing between Ni and Rh states, makes the Ni-O-Rh-O-Ni superexchange paths strong, as shown in the encircled part of the overlap of Wannier functions in right panel Fig. 6.4.

The calculated exchange interactions for low-temperature tetragonal phase turned out to be $J_1 \approx 1.2$ meV, J_2' and $J_2'' \approx 0.4 J_1$. The dominant interaction J_1 was found to vary between 1.2 and 0.8 meV, with little changes in the ratios of magnetic exchanges on variation of the U_{Ni} value ranging between 5 and 7 eV. Thus the calculated strengths of the exchange interactions led to strong magnetic frustration. The scale of J_1 derived from our calculations was found to be in good

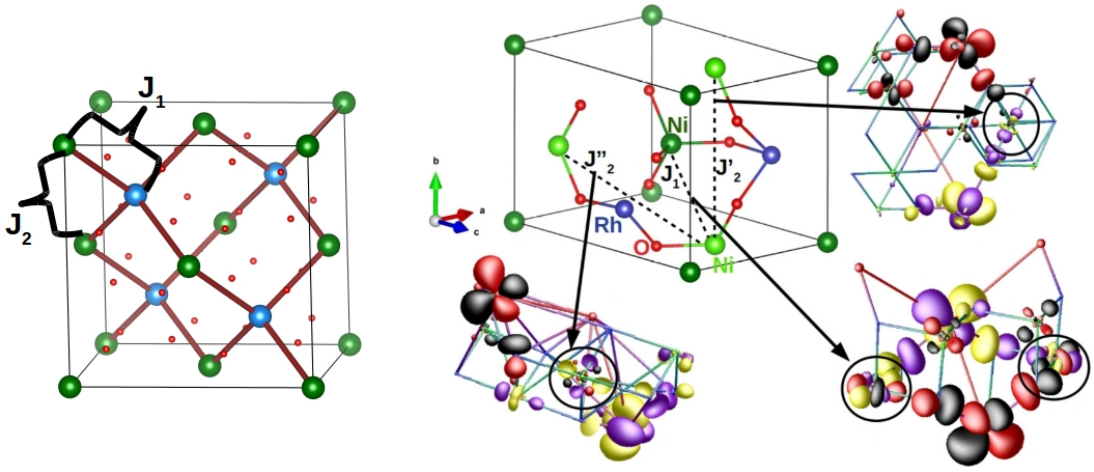

Figure 6.4: Nearest neighbour (NN) and next nearest neighbour (NNN) Ni-Ni interactions J_1 and J_2 belonging to two different fcc lattices and the same fcc lattice for the cubic phase of $NiRh_2O_4$ are shown in the left. The Ni atoms belonging two different fcc lattices are marked differently with green and blue balls. The exchange pathways for nearest neighbour (J_1) and inequivalent second neighbours (J_2', J_2'') in the low-temperature tetragonal phase of $NiRh_2O_4$ are shown in the right panel. The effective Ni Wannier function overlap placed at NN, in-plane NNN, and out-of-plane NNN Ni sites are also shown in the right panel. Circles indicate the nonzero overlap at Rh sites in the pathway. Differently coloured lobes denote opposite sign parts of each Wannier function.

agreement with previous rough estimates [23].

6.4.2 Single-site model

Together with the DFT results, next we constructed an effective single-site model Hamiltonian for Ni^{2+} in the tetrahedral crystal field.

The presence of the two holes in the high-energy t_2 orbital, encourages strong Hund's interaction to favour total $L_{eff} = 1$ and total S = 1 situation. Our Hamiltonian, considering tetragonal distortion (δ) and spin-orbit coupling (λ) took the form as,

$$H = -\delta L_z^2 + \lambda \vec{L} \cdot \vec{S} \tag{6.1}$$

where the sign of SOC depends on the two holes in t_2 manifold. The t_2 manifold flips the sign of the orbital angular momentum, so $L_{eff} = 1$ carries an orbital magnetic moment $-\vec{L}$. Thus in the state $|L_z, S_z\rangle = |+, -\rangle$, the orbital and spin magnetic moment direction becomes parallel, as in the full DFT.

The limit of $\lambda \gg \delta$ led to the $J_{eff} = 0$ singlet ground state [28].

Based on the DFT inputs ($\delta \approx 100$ meV) we considered $\delta \gg \lambda$, and in

this regime we constructed orbital eigenstates with well-defined L_z, which led to a ground doublet with $L_z = \pm 1$ and an excited orbital singlet with $L_z = 0$, separated by a large energy δ.

Next we allowed SOC to play and couple through λ with dominant SOC coupling $\lambda L_z S_z$. A sequence of states in increasing energy was made as follows being led by $\lambda L_z S_z$,

$$\begin{aligned} E_0^0[2] &= -\delta - \lambda : |\pm, \mp\rangle \\ E_1^0[2] &= -\delta : |\pm, 0\rangle \\ E_2^0[2] &= -\delta + \lambda : |\pm, \pm\rangle \\ E_3^0[3] &= 0 : |0, 0\rangle, |0, \pm\rangle \end{aligned} \tag{6.2}$$

The degeneracies of having the same energy are shown in square brackets of Eq. (6.2).

We treated $\lambda(L^+S^- + L^-S^+)/2$ perturbatively as it couples the lower energy states $E_{0,1,2}^0$ to the higher energy states E_3^0. Now doing so and defining the symmetric state $|e\rangle = (|+,-\rangle + |-,+\rangle)/\sqrt{2}$, we got a sequence of states with energy differences from the ground state as follows,

$$\begin{aligned} |\psi_0\rangle &\approx |e\rangle - \sqrt{2}\frac{\lambda}{\delta}|0,0\rangle; & \Delta_0 &= 0 \\ |\psi_1\rangle &= \frac{|+,-\rangle - |-,+\rangle}{\sqrt{2}}; & \Delta_1 &\approx 2\frac{\lambda^2}{\delta} \\ |\psi_{2,\pm}\rangle &\approx |\pm,0\rangle - \frac{\lambda}{\delta}|0,\pm\rangle; & \Delta_2 &\approx \lambda + \frac{\lambda^2}{\delta} \\ |\psi_{3,\pm}\rangle &= |\pm,\pm\rangle; & \Delta_3 &\approx 2\lambda + 2\frac{\lambda^2}{\delta} \\ |\psi_{4,\pm}\rangle &\approx |0,\pm\rangle + \frac{\lambda}{\delta}|\pm,0\rangle; & \Delta_4 &\approx \delta + \lambda + 3\frac{\lambda^2}{\delta} \\ |\psi_5\rangle &\approx |0,0\rangle + \frac{\sqrt{2}\lambda}{\delta}|e\rangle; & \Delta_5 &\approx \delta + \lambda + 4\frac{\lambda^2}{\delta} \end{aligned} \tag{6.3}$$

Ground state

Analysis of the energy states we found that the ground state is a nonmagnetic singlet being consistent with the absence of any magnetic order down to the lowest temperature in this material [42].

Our proposed nonmagnetic ground state was a spin-orbit entangled type singlet state originated from the weak splitting of a doublet due to off-diagonal SOC.

Thermodynamics

The gap of the states $|\psi_{4,\pm}\rangle$ and $|\psi_5\rangle$ was found to be large and we recovered an entropy $S_{low} = R\ln 6$ for $T < 300$ K [cf. left panel Fig. 6.5] which was found to be consistent with earlier work in Ref. [23]. At low-temperature Δ_1,

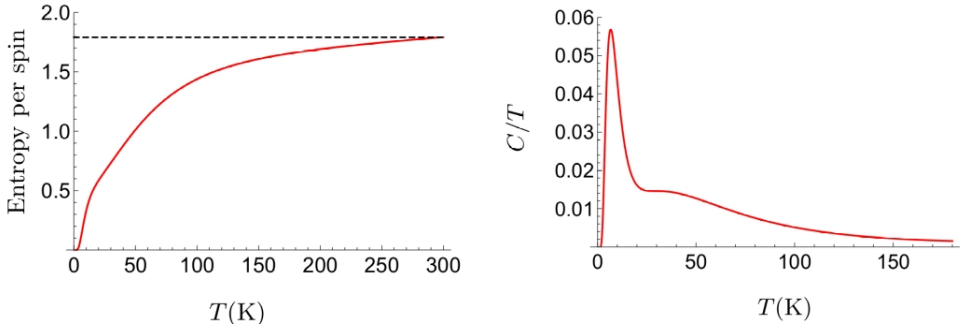

Figure 6.5: Entropy per spin (k_B) as a function of temperature is shown in left panel. Dashed line indicates ln 6 corresponding to the lowest 6 states which are accessible up to room temperature. Scaled specific heat per spin vs. temperature T is plotted as C/T (k_B/K) for the single site model in right panel showing first Schottky peak at $T \sim$ 10 K and second smeared Schottky bump near $T \sim 40$ K.

corresponding to $|\psi_1\rangle$ state, showed a Schottky peak in C/T at $T \sim 10$ K as shown in right panel of Fig. 6.5. The higher levels $|\psi_{2,\pm}\rangle$ showed broad Schottky peak at $T \sim 40$ K.

Neutron scattering

The calculated local dynamical spin correlation function $S_{loc}(\omega)$ is presented in the left panel of Fig. 6.6. Analysing this it was found that the first excited state is nondegenerate, being separated by an energy $\Delta_1 \approx 2$ meV.

It was expected to observe $|\psi_1\rangle$ in non-spin-flip scattering as $|\psi_0\rangle$ and $|\psi_1\rangle$ were connected by S^z, but it appeared difficult to get visible due to the resolution and the background.

The second excited state, a doublet $|\psi_{2,\pm}\rangle$ was observed with an energy gap $\Delta_2 \approx 11$ meV. The states $|\psi_{3,\pm}\rangle$ at an energy gap $\Delta_3 \approx 22$ meV and singlet state $|\psi_5\rangle$ at energy gap $\Delta_4 \approx 108$ meV were marked as 'dark states' as they were invisible to neutrons due to vanishing matrix elements. States $|\psi_{4,\pm}\rangle$ with energy gap $\Delta_5 \approx 107$ meV again appeared with much smaller spectral weight than that of $|\psi_{2,\pm}\rangle$.

These invisible, 'dark-states' pave the path for future inelastic neutron scattering experiments.

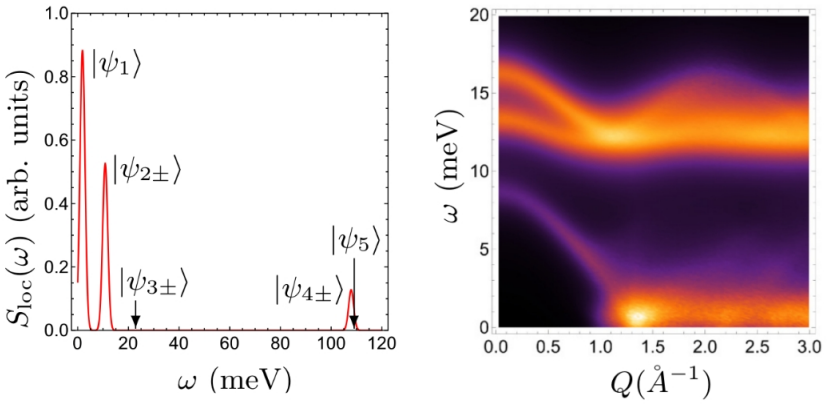

Figure 6.6: Local dynamical spin correlation function $S_{loc}(\omega)$ within single-site model is shown in left panel. Relevant excited states are represented by the peaks. The arrows indicate the invisible states to neutrons. The intensity plot in arbitrary units of powder-averaged inelastic neutron scattering spin structure factor, $S(Q,\omega)$, as a function of wave vector Q and energy ω is shown in right panel with 1 meV broadening to mimic the experimental situation.

Magnetic susceptibility

The computed single-site magnetic susceptibility χ and the inverse susceptibility χ^{-1} are shown in the left and right panels of Fig. 6.7 respectively.

χ^{-1} was fitted to the Curie-Weiss form $\chi(T) = \chi_0 + \alpha/(T - T_0)$ apparently [cf. right panel Fig. 6.7] with a negligible background χ_0 ($\approx 10^{-5}$). The Curie-Weiss scale was found to be $T_0 \approx 16$ K.

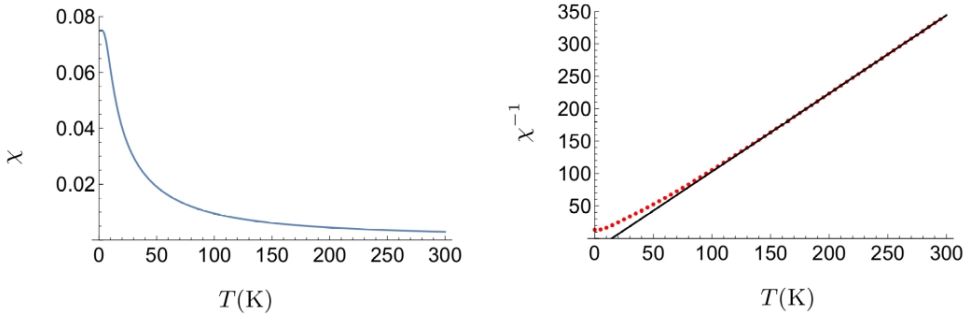

Figure 6.7: Plot of susceptibility χ (K^{-1}) in left. Plot of inverse susceptibility χ^{-1} (K) of the single-site model is shown in right panel. Points denote computed values and solid line denotes a fit to the Curie-Weiss form.

Thus the computed estimate for T_0 from our calculation appeared to be small and ferromagnetic in sign in contrast to the experimentally observed $T_0 \approx$ -11

K [23]. We attributed weak residual intersite antiferromagnetic exchanges as the origin of this experimental antiferromagnetic T_0.

Setting the fitted $\alpha \equiv S_{eff}(S_{eff}+1)/3$ gave rise to effective spin $S_{eff} = 1.4$ which is larger than spin-only value S = 1 [23].

Intersite exchange

Next intersite exchanges were incorporated using a simple J_1-J_2 Heisenberg exchange model of the form $H_{ex} = \frac{1}{2}\sum_{i,j} J_{ij} S_i \cdot S_j$.

Slave-boson theory [28,43,44] with four local boson operators, $c_0^\dagger$, $c_1^\dagger$, $d_\pm^\dagger$, was applied to compute the spin dynamics in low-energy Hilbert space. The local boson operators create $|\psi_0\rangle$, $|\psi_1\rangle$ and $|\psi_{2\pm}\rangle$ states .

Projecting the Heisenberg model to the Hilbert subspace, with local completeness constraint $(c_0^\dagger c_0 + c_1^\dagger c_1 + d_\alpha^\dagger d_\alpha) = 1$ we arrived to the Hamiltonian as, $H_{tot} = H_{loc} + H_{ex} + H_{con}$, where H_{loc}, H_{ex} and H_{con} denote local single-site Hamiltonian, intersite exchange Hamiltonian, and the constraint imposed Hamiltonian via the Lagrange multiplier μ respectively with the explicit form as,

$$H_{loc} = \sum_i (\Delta_1 c_{i1}^\dagger c_{i1} + \Delta_2 d_{i\alpha}^\dagger d_{i\alpha}) \tag{6.4}$$

$$H_{ex} = \frac{1}{4}\langle c_0\rangle^2 \sum_{i,j} J_{ij}[(d_{i\alpha}^\dagger d_{j\alpha} + d_{i\alpha}^\dagger d_{j\bar{\alpha}}^\dagger + H.c.) + 2(c_{i1}^\dagger + c_{i1})(c_{j1}^\dagger + c_{j1})] \tag{6.5}$$

$$H_{con} = -\mu \sum_i (c_{i1}^\dagger c_{i1} + d_{i\alpha}^\dagger d_{i\alpha} + \langle c_0\rangle^2 - 1) \tag{6.6}$$

Considering $\Delta_1 = 1.8$ meV, $\Delta_2 = 11$ meV from the single-site model, and $J_1 = 1.2$ meV and $J_2/J_1 = 0.4$ from DFT results we minimised the ground state energy with respect to $\langle c_0\rangle^2$, taking μ to satisfy the constraint. We obtained the optimal $\langle c_0\rangle^2 \approx 0.7$ and $\mu \approx$ -2.1 meV.

The resulting weighted and powder-averaged dynamic spin factor relevant to INS experiments, $S(Q,\omega)$ is shown in right panel Fig. 6.6 including 1 meV broadening to realize the experimental resolution. Our study explained that the upper gapped mode appeared from the $|\psi_{2,\pm}\rangle$ states making a good agreement with INS observations of a gapped dispersive mode [23].

We argued that the $S(Q,\omega)$ plot contained two peaks due to two sublattices on the diamond lattice. The lower gapped mode arising from $|\psi_1\rangle$ state formed the optical branch which collapsed in energy, with increasing Q from $\sim$ 8 meV down to $\sim$ 0.5 meV. This optical branch remained intact as an intense small-gap band being robust against magnetic condensate formation due to frustrating J_2 exchange interaction.

The acoustic branch of $|\psi_1\rangle$ state with low energy was also found to be gapped, but became invisible due to negligible intensity.

6.5 Summary

In conjunction with density functional theory based calculations and model calculations, here we addressed the mystery of $NiRh_2O_4$ by capturing the existing thermodynamic and INS observations.

Our study showed that the low-temperature tetragonal phse of $NiRh_2O_4$, associated with $c/a > 1$, allows spin-orbit coupling to play significantly due to the active degrees of freedom of partially filled Ni t_2 states. The Wannier function overlap for the dominant exchange paths in tetragonal phase showed non-zero overlap on the non-magnetic Rh site indicating strong Ni-O-Rh-O-Ni superexchange pathways. Solution of the model Hamiltonian revealed the presence of non-magnetic singlet state driven by spin-orbit coupling.

Finally, our study revealed that $NiRh_2O_4$ could not be realized as a candidate of topological quantum paramagnet.

Bibliography

[1] M. Z. Hasan and C. L. Kane, Rev. Mod. Phys. **82**, 3045 (2010).

[2] X.-L. Qi and S.-C. Zhang, Rev. Mod. Phys. **83**, 1057 (2011).

[3] B. Yan and C. Felser, Annu. Rev. Condens. Matter Phys. **8**, 337 (2017).

[4] A. Vishwanath and T. Senthil, Phys. Rev. X **3**, 011016 (2013).

[5] M. Levin and Z.-C. Gu, Phys. Rev. B **86**, 115109 (2012).

[6] F. Pollmann, E. Berg, A. M. Turner, and M. Oshikawa, Phys. Rev. B **85**, 075125 (2012).

[7] T. Senthil and M. Levin, Phys. Rev. Lett. **110**, 046801 (2013).

[8] T. Senthil, Annu. Rev. Condens. Matter Phys. **6**, 299 (2015).

[9] C. Wang, A. Nahum, and T. Senthil, Phys. Rev. B **91**, 195131 (2015).

[10] F. D. M. Haldane, Phys. Rev. Lett. **50**, 1153 (1983).

[11] I. Affleck, T. Kennedy, E. H. Lieb, and H. Tasaki, Phys. Rev. Lett. **59**, 799 (1987).

[12] V. Fritsch, J. Hemberger, N. Büttgen, E.-W. Scheidt, H.-A. Krug von Nidda, A. Loidl, and V. Tsurkan, Phys. Rev. Lett. **92**, 116401 (2004).

[13] N. Tristan, J. Hemberger, A. Krimmel, H.-A. Krug von Nidda, V. Tsurkan, and A. Loidl, Phys. Rev. B **72**, 174404 (2005).

[14] D. Bergman, J. Alicea, E. Gull, S. Trebst, and L. Balents, Nat. Phys. **3**, 487 (2007).

[15] J.-S. Bernier, M. J. Lawler, and Y. B. Kim, Phys. Rev. Lett. **101**, 047201 (2008).

[16] S. Gao, O. Zaharko, V. Tsurkan, Y. Su, J. S. White, G. S. Tucker, B. Roessli, F. Bourdarot, R. Sibille, D. Chernyshov *et al.*, Nat. Phys. **13**, 157 (2016).

[17] L. Ge, J. Flynn, J. A. M. Paddison, M. B. Stone, S. Calder, M. A. Subramanian, A. P. Ramirez, and M. Mourigal, Phys. Rev. B **96**, 064413 (2017).

[18] J. Oitmaa, Phys. Rev. B **99**, 134407 (2019).

[19] G. Chen, L. Balents, and A. P. Schnyder, Phys. Rev. Lett. **102**, 096406 (2009).

[20] G. Chen, A. P. Schnyder, and L. Balents, Phys. Rev. B **80**, 224409 (2009).

[21] K. W. Plumb, J. R. Morey, J. A. Rodriguez-Rivera, H. Wu, A. A. Podlesnyak, T. M. McQueen, and C. L. Broholm, Phys. Rev. X **6**, 041055 (2016).

[22] V. Tsurkan, L. Prodan, V. Felea, I. Filippova, V. Kravtsov, A. Gnther, S. Widmann, H.-A. Krug von Nidda, J. Deisenhofer, and A. Loidl, Phys. Rev. B **96**, 054417 (2017).

[23] J. R. Chamorro, L. Ge, J. Flynn, M. A. Subramanian, M. Mourigal, and T. M. McQueen, Phys. Rev. Mater. **2**, 034404 (2018).

[24] G. Blasse and D. Schipper, Phys. Lett. **5**, 300 (1963).

[25] The calculations in our Rapid Communication showed that the correct crystal field level scheme is different. In the large distortion limit in [23] the ground state is Γ_1 singlet with a triplet excited Γ_5 state, while we predicted the ground state associated with weakly split doublet and a further excited doublet at the SOC scale $\sim \lambda$.

[26] G. Chen, Phys. Rev. B **96**, 020412(R) (2017).

[27] F. L. Buessen, M. Hering, J. Reuther, and S. Trebst, Phys. Rev. Lett. **120**, 057201 (2018).

[28] F.-Y. Li and G. Chen, Phys. Rev. B **100**, 045103 (2019).

[29] G. Khaliullin, Phys. Rev. Lett. **111**, 197201 (2013).

[30] A. Akbari and G. Khaliullin, Phys. Rev. B **90**, 035137 (2014).

[31] C. Svoboda, M. Randeria, and N. Trivedi, Phys. Rev. B **95**, 014409 (2017).

[32] J. F. Dulac, Bulletin de la Societe Francaise de Mineralogie et de Cristallographie **92**, 25 (1969).

[33] G. Kresse *et. al.*, Phys. Rev. B **54**, 11169 (1996).

[34] O. K. Andersen and O. Jepsen, Phys. Rev. Lett. **53**, 2571 (1984).

[35] O. K. Andersen and T. Saha-Dasgupta, Phys. Rev. B **62**, R16219 (2000).

[36] P. Blaha, K. Schwartz, G. K. H. Madsen, D. Kvasnicka and J. Luitz, Wien2k, An Augumented Plane Wave + Local Orbitals Program for Calculating Crystal Properties, Technische Universitiät Wien, Vienna **28**, (2001).

[37] P. E. Blöchl, Phys. Rev. B **50**, 17953 (1994).

[38] J. P. Perdew, K. Burke, and M. Ernzerhof. Phys. Rev. Lett. **77**, 3865 (1996).

[39] V. I. Anisimov, I. V. Solovyev, and M. A. Korotin, Phys. Rev. B **48**, 16929 (1993).

[40] Calculated orbital moment at the Rh site was found to be smaller than that of Ni ($\approx 0.05\ \mu_B$). Both calculations within GGA+SOC and GGA+U+SOC suggested for orbital moment quenching at the Rh site.

[41] S. Sarkar, M. De Raychaudhury, I. Dasgupta, and T. Saha-Dasgupta, Phys. Rev. B **80**, 201101(R) (2009).

[42] This was clearly appreciated in Ref. [23].

[43] S. Sachdev and R. N. Bhatt, Phys. Rev. B **41**, 9323 (1990).

[44] F.-Y. Li and G. Chen, Phys. Rev. B **98**, 045109 (2018).

Chapter 7

Conclusion and outlook

7.1 Conclusion

In the thesis we have studied and investigated the structural as well as the microscopic origin of different novel properties of functional materials namely, transition metal oxides. As presented in chapters 3-6, we have studied different intriguing properties including multiferroicity, high T_C ferromagnetic insulating properties, multicomponent high moment magnetism and symmetry protected quantum spin liquid behaviour.

We have carried out density functional theory (DFT) based calculations armed with first-principles derived model Hamiltonian approach in order to explore different interesting properties of the systems we studied. In addition to these we have also employed exact diagonalization (ED) technique and quantum Monte Carlo simulation to solve the model Hamiltonian for obtaining the physical properties. To predict the crystal structure of a compound only knowing the chemical composition we have further applied genetic algorithm.

In this chapter we summarize all the results obtained through our calculations in a concise manner as well as discuss the future scopes which can be taken up.

7.1.1 Chapter 3: Examining the microscopic chemical structure and mixed anion chemistry through fluorination for oxygen deficient compounds of $CaMnO_{3-x}$ (x = 1, 0.5)

In this joint theoretical-experimental study, we have studied two oxygen deficient compounds of a well known perovskite $CaMnO_3$, namely $CaMnO_2$ and $CaMnO_{2.5}$. Employing the density functional theory based calculations we per-

formed the local structure analysis of $CaMnO_2$. For $CaMnO_{2.5}$ we have studied the mixed anion chemistry incorporating F as a foreign anion into the system. The key findings are presented below.

Re-examining the nature of ordering in $CaMnO_2$: The role of Mn-O covalency in the local structure

- Collaborative experimental study employing local probes reveals a very different chemical structure of $CaMnO_2$ at microscopic level in contrast to the random Ca/Mn distribution as concluded from the diffraction like bulk probe. It claims the presence of a novel structural pattern with locally ordered regions where Ca and Mn atoms are arranged in alternate layers, separated by antiphase boundaries instead of 6 Ca/6 Mn arrangement.
- DFT total energy calculation shows that the structure with antiphase boundary is the most stable structure agreeing with the experimental finding.
- The local distribution of cations around oxygen plays an important role in determining Mn-O covalency. Our study shows that presence of antiphase boundary is supported by enhanced Mn-O covalency.
- The calculated values of magnetic exchange interaction terms show that the in-plane missing interactions are compensated by the gained out-plane interaction terms in the structure with antiphase boundary, hence giving rise to its magnetic energy gain and supporting it to be the most stable structure of $CaMnO_2$.

Mixed Anion Physics in Flourinated vacancy ordered Brownmillerite: A possible route to Multiferrocity

- Oxygen deficient compound $CaMnO_{2.5}$ shows stabilization of unique up-up-down-down spin arrangement with strong magneto-structural coupling, akin to that found in $HoMnO_3$ [1].
- Incorporation of fluorine increases the valence of Mn indicating that F sits in some interstitial position instead of substituting oxygen atoms only.
- Enthalpy calculation shows that enthalpy decreases whenever number of fluorine sitting in the interstitial position (with or without substitution) increases because addition of fluorine in the interstitial position makes the MnO_5F octahedra complete.
- The interplay between octahedral completion and making the Mn valence close to 3+ makes $Ca_4Mn_4O_9F_3$ the most favourable amongst all the possibilities on fluorination of $CaMnO_{2.5}$.

- Fluorine is not off-centered when system incorporates F in the interstitial site(s) only while fluorine becomes off-centered together with substitution and interstitial occupancies giving rise to finite polarization in the system.

- The off-centric movement of F in $Ca_4Mn_4O_9F_3$ breaks the centrosymmetricity and develops finite polarisation in the system which holds the promise to be a multiferroic.

7.1.2 Chapter 4: Understanding the curious magnetic state of Sr_3OsO_6

In this chapter we have carried out density functional theory based calculation together with model Hamiltonian approach on single transition metal Os containing B site ordered double perovskite Sr_3OsO_6. The few band Wannier function based model Hamiltonian is then solved by exact diagonalization technique to understand the parameter space. We have also employed genetic algorithm to predict the crystal symmetry of Sr_3OsO_6 theoretically. Here we have explored the microscopic origin of its reported high-T_C ferromagnetic insulating behaviour in cubic symmetry [2]. The main findings are:

- Monoclinic symmetry is found to be the most preferred symmetry followed by triclinic symmetry on investigation of total energy vs. volume calculation. The reported cubic symmetry is found to be energetically much higher.

- Reported stabilization of Sr_3OsO_6 in cubic symmetry is due to its epitaxial growth on $SrTiO_3$ substrate.

- To explore the role of crystal symmetry on magnetism, the Os t_{2g} based Wannier function overlap are made for lowest energy monoclinic structure and reported cubic structure. The Wannier overlaps show large Os-Os hopping across the face of the cubic structure dominating over the conventionally expected Os-O-Sr_B-O-Os superexchange path along the edge of the cubic structure while that well connected Os-Os path becomes misaligned in the monoclinic structure due to structural distortion weakening the hopping process.

- Solving the two-site Os t_{2g} full multiplet problem with exact diagonalization method we obtained the U-J_H phase space for monoclinic and cubic structure of Sr_3OsO_6. A significant part of U-J_H phase space supports ferromagnetic interaction in cubic symmetry favouring reported high T_C [2] whereas antiferromagnetic interaction is supported in monoclinic structure with low T_N as observed in the antiferromagnetic phase of Ca_3OsO_6 [3].

- Electronic structure calculation shows that an insulating ground state is achieved in GGA+SOC+U scheme opening up a gap in spin-orbit entangled $j = 3/2$ Mott state.

7.1.3 Chapter 5: Understanding Magnetism in Double Double Perovskites: A Complex Multiple Magnetic Sublattice System

In this chapter, carrying out DFT calculations together with model Hamiltonian, we have studied the magnetism of multi magnetic sublattice system, A and B site ordered double double perovskite of general formula $AA'_{0.5}A''_{0.5}BB'O_6$. Our findings are:

- We have uncovered the microscopic origin of long range ordered magnetism in double double perovskite compounds with $3d$ transition metal ion at A and B sites, and $5d$ magnetic ions at B′ sites.

- Our calculation brought out the interplay between hybridization driven multi-sublattice double exchange and superexchange mechanism of magnetism depending on the position of the d energy levels as well as its filling.

- Total energy calculation of different spin arrangement shows the stabilization of ferromagnetic long range order in $CaMnNiReO_6$ with Mn ions of two different coordination at A sites, and Ni and Re ions at B and B′ sites. The replacement of Ni by Co at B site decreases the filling by one in $CaMnCoReO_6$ stabilizing ferrimagnetism which is in good agreement with experimental observations [4].

- The temperature dependency of magnetism is obtained by employing Monte Carlo simulation on the spin Hamiltonian. The quantum simulation reproduces the experimentally observed magnetic ground state spin arrangement of both $CaMnNiReO_6$ and $CaMnCoReO_6$. The calculated transition temperatures of both the compounds are found to be close to the experimentally observed values with reasonable accuracy. For $CaMnCoReO_6$, the competition between ferro and antiferro nature of the effective interactions, gives rise to two hump structure of dM/dT curve.

- To mimic the experimental situation off-stoichiometry has been introduced and Ni-poor and Co-rich compounds are made. The magnetic properties are found to be intact even in presence of off-stoichiometry.

7.1.4 Chapter 6: $NiRh_2O_4$: A spin-orbit entangled diamond-lattice paramagnet

Here we have applied density functional theory based calculations in conjunction with model Hamiltonian approach to address the curious state of $NiRh_2O_4$ by capturing the existing thermodynamic and inelastic neutron scattering (INS) observations. Our results are listed below:

- Tetragonal distortion, with $c/a > 1$ makes the t_2 states of Ni partially filled and the active orbital degrees of freedom allows spin-orbit coupling to play an important role.
- Electronic structure calculation shows half-metallic solution which becomes insulating on application of spin-orbit coupling for both the high-temperature cubic phase as well as the low-temperature tetragonal phase of $NiRh_2O_4$.
- Analysis of energy level diagram of d orbitals shows that tetrahedrally coordinated Ni has larger spin splitting than octahedrally coordinated Rh satisfying the high-spin state of Ni and low-spin state of Rh. The crystal field splitting of Rh is found to be larger than that of Ni.
- In tetragonal phase, analysis of the dominant exchange interaction paths, effective hopping strengths and on-site energies in the Wannier basis of Ni t_2 only low-energy Hamiltonian, show significant mixing between Ni and Rh states which makes Ni-O-Rh-O-Ni superexchange path strong.
- Single site model Hamiltonian shows that the ground state is nonmagnetic, spin-orbit coupling entangled singlet.

7.2 Outlook

In the present thesis we have studied transition metal oxides as functional materials to explore their various intriguing properties. There are few scopes in connection to the present study which may be worthwhile to explore in future. Here we list such few possibilities.

- Our investigation on $CaMnO_{2.5}$ suggests that manipulating the anionic sublattice and incorporating dissimilar anions in a system can emerge interesting properties and this can be an effective tool to tailor the functional properties of transition metal oxides apart from cationic substitution.
- Study on single transition metal containing B site ordered double perovskite Sr_3OsO_6 shows the stabilization of ferromagnetic insulating state associated with high T_C value in its cubic symmetry. In search for related double

perovskite candidates with such high T_C ferromagnetic insulating state, our study recommends Sr_2CaOsO_6 as a promising candidate. The reported powder x-ray diffraction analysis [5] of synthesized Sr_2CaOsO_6 together with the calculated tolerance value which turns out to be 0.93, suggests an ordered cubic structure of Sr_2CaOsO_6. Calculated Os-Os hopping strengths in Sr_2CaOsO_6 are also found to be similar to that of cubic Sr_3OsO_6, the largest Os-Os hopping strength is 0.16 eV compared to 0.17 eV in Sr_3OsO_6. All these raise the expectation that Sr_2CaOsO_6 in bulk form can support high T_C ferromagnetism which will be purposeful to explore.

- Our study on the multi magnetic sublattice system consisting of $3d$ and $5d$ transition metal ions in double-double perovskite structural framework, reveals rich physics of its magnetism. Our proposed theory of magnetism taking into account hybridization-driven double-exchange and superexchange mechanism, remains general to be applicable for multi sublattice mixed $3d$-$4d/5d$ transition metal systems. Our study opens up possibility of stabilization of a large moment ferromagnetic state depending on the proper choice of $3d$ and $4d/5d$ elements. Our studied systems show half metallic solution with high moment which can be applied for spintronics applications.

- Our investigation on $NiRh_2O_4$ suggests to revisit the specific heat at low-temperature and low-energy inelastic neutron scattering on higher purity samples. It also proposes that Terahertz spectroscopy [6, 7] on $NiRh_2O_4$ could check our prediction of the optical $|\psi_1\rangle$ mode at $Q = 0$.
  Our study also suggested Raman or resonant inelastic x-ray scattering at Ni edge [8] to look for the predicted invisible 'dark states', $|\psi_{3\pm}\rangle$ and $|\psi_5\rangle$.
  Our study also directs to future study suggesting tetragonal compression to provide quenched orbital momentum and suppressed spin-orbit coupling effect.

Bibliography

[1] S. Picozzi, K. Yamauchi, B. Sanyal, I. A. Sergienko and E. Dagotto, Phys. Rev. Lett. **99**, 227201 (2007).

[2] Y. K. Wakabayashi, Y. Krockenberger, N. Tsujimoto, T. Boykin, S. Tsuneyuki, Y. Taniyasu, and H. Yamamoto, Nat. Commun. **10**, 535 (2019).

[3] H. L. Feng, Y. Shi, Y. Guo, J. Li, A. Sato, Y. Sun, X. Wang, S. Yu, C. I. Sathish, and K. Yamaura, J. Solid State Chem. **201**, 186 (2013).

[4] E. Solana-Madruga, A. M. Arévalo-López, A. J. Dos santos García, C. Ritter, C. Cascales, R. Sáez-Puche, J. P. Attfield, Phys. Rev. B **97**, 134408 (2018).

[5] J.-H. Choy, D.-K. Kim, J.-Y. Kim, Solid State Ionics **108**, 159 (1998).

[6] N. J. Laurita, J. Deisenhofer, L. D. Pan, C. M. Morris, M. Schmidt, M. Johnsson, V. Tsurkan, A. Loidl, and N. P. Armitage, Phys. Rev. Lett. **114**, 207201 (2015).

[7] X. Zhang, F. Mahmood, M. Daum, Z. Dun, J. A. M. Paddison, N. J. Laurita, T. Hong, H. Zhou, N. P. Armitage, and M. Mourigal, Phys. Rev. X **8**, 031001 (2018).

[8] Y. Lu, D. Betto, K. Fürsich, H. Suzuki, H.-H. Kim, G. Cristiani, G. Logvenov, N. B. Brookes, E. Benckiser, M. W. Haverkort *et al.*, Phys. Rev. X **8**, 031014 (2018).